Downloaded from UvA-DARE, the institutional repository of the University of Amsterdam (UvA)
http://dare.uva.nl/document/81092

File ID	81092
Filename	Thesis

SOURCE (OR PART OF THE FOLLOWING SOURCE):

Type	Dissertation
Title	Charged current deep inelastic scattering at HERA
Author	A.I. van Sighem
Faculty	Faculty of Science
Year	2000
Pages	123

FULL BIBLIOGRAPHIC DETAILS:
http://dare.uva.nl/record/89312

Copyright

It is not permitted to download or to forward/distribute the text or part of it without the consent of the author(s) and/or copyright holder(s), other than for strictly personal, individual use.

UvA-DARE is a service provided by the library of the University of Amsterdam (http://dare.uva.nl)

Charged Current Deep Inelastic Scattering at HERA

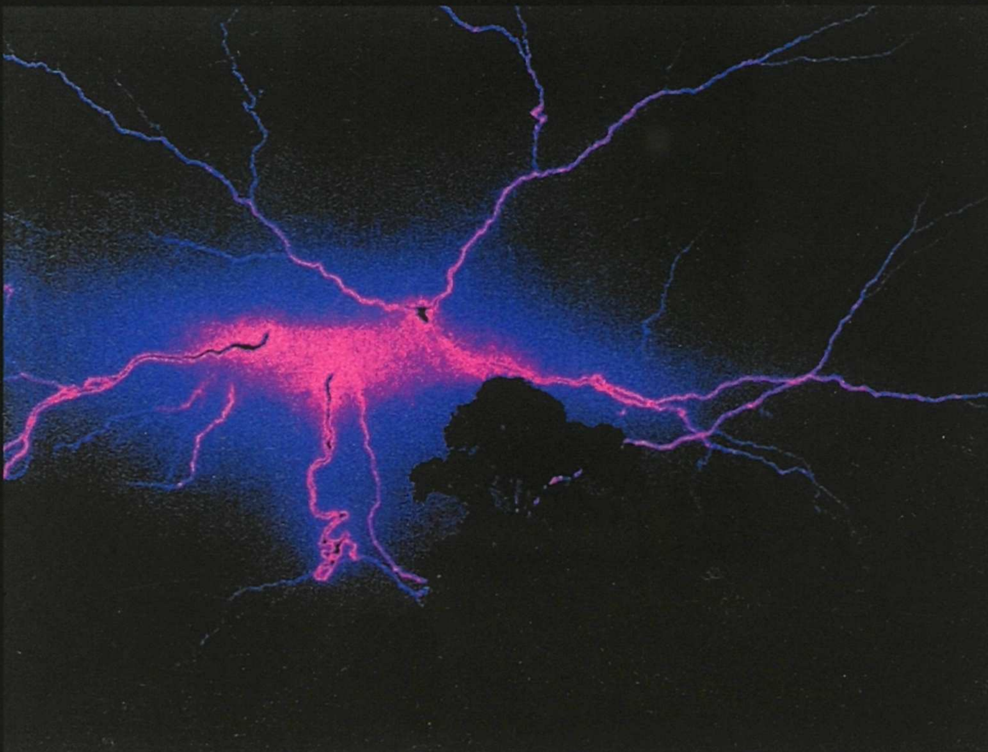

Ard van Sighem

Charged Current Deep Inelastic Scattering at HERA

Charged Current Deep Inelastic Scattering at HERA

Academisch Proefschrift

ter verkrijging van de graad van doctor
aan de Universiteit van Amsterdam
op gezag van de Rector Magnificus
Prof. Dr. J.J.M. Franse
ten overstaan van een door het college voor promoties
ingestelde commissie, in het openbaar te verdedigen
in de Aula der Universiteit
op dinsdag 29 februari 2000 te 13.00 uur

door

Adrianus Izaäk van Sighem
geboren te Vlissingen

Promotor: Prof. Dr. J.J. Engelen
Co-Promotor: Dr. P.M. Kooijman

Faculteit der Natuurwetenschappen, Wiskunde en Informatica

The work described in this thesis is part of the research programme of 'het Nationaal Instituut voor Kernfysica en Hoge-Energie Fysica (NIKHEF)' in Amsterdam, the Netherlands. The author was financially supported by 'de Stichting voor Fundamenteel Onderzoek der Materie (FOM)', which is funded by 'de Nederlandse Organisatie voor Wetenschappelijk Onderzoek (NWO)'.

IJdelheid der ijdelheden, zegt Prediker, ijdelheid der ijdelheden! Alles is ijdelheid.

Prediker 1:2

Contents

Introduction

Why are we here? Why does the world exist? Who created it and when? When the progenitors of the human race learnt to think they probably also wondered about these questions. During the evolution of civilisation quite a number of answers has been proposed. The ancient Greeks, for example, regarded the earth as a goddess called Gaia who sprang from the primordial void Chaos. An Egyptian creation myth says that there existed only the ocean at first. On its surface appeared an egg that brought forth Ra, the sun, who got four children. One of these children was Geb, who became the earth.

Another approach consists of evading these questions by taking resort to humour instead of mythology or religion. For example, one author[1] claims the answer to the question of everything is 42 and the sole purpose of the earth is to find this question. In this thesis we will, however, follow the scientific approach.

Scientists can give a partial answer to the questions above within a well defined framework, in which the quest for the creator plays no explicit part. The modern scientific view is that the world is the result of a big explosion twelve billion years ago and that we are some sort of eructation of the vacuum. Scientists endeavour to deduce the origin of the world from measurements instead of mythology. Accordingly, this thesis will contain a measurement of one aspect of the scientific view on this world.

The physical world as it is known today is built up of tiny particles which are called atoms. Their diameter is about 10^{-10} m. These atoms are made of smaller particles and consist of a positively charged nucleus that is surrounded by a cloud of negatively charged electrons. Electrons are fundamental particles: they do not have a structure and thus they are not built up of smaller particles, at least not as far as it is known today. On the other hand, the nucleus of an atom is composed of particles called protons, which have a positive charge, and neutrons, which are electrically neutral. The typical size of protons and neutrons is 100000 times smaller than the size of an atom.

Protons and neutrons are fundamental particles neither as they consist of still smaller entities, so-called quarks. Quarks are fundamental particles. They have a non-integer charge. Two types of quarks exist, the up and the down quark, and three of these can build up a proton or a neutron. Such combinations of three quarks are called baryons.

Every charged particle has a corresponding antiparticle with opposite charge[2]. An antiquark can form a bound state with a quark. These combinations are called mesons. Together with the baryons they form a group of composite particles that are known as hadrons.

---

[1] D. Adams, *The hitchhiker's guide to the galaxy.*

[2] "Charge" is to be understood in a generic sense. It refers not only to electrical charge.

There is one more particle that belongs to "daily life". This particle is called neutrino and plays a role in the radioactive decay of nuclei where a neutron decays into a proton, an electron and an antineutrino. Neutrinos and electrons belong to the class of particles known as leptons.

Apart from the four fundamental particles (two quarks, the electron and the neutrino) and their antiparticles there exist two heavier versions of each of these four particles. Thus there exist four more quarks with a mass larger than the up and the down quark. Also two heavy electrons exist, the muon and the tau particle, with corresponding neutrinos[3]. An overview of all these particles, their charge and their mass is given in the table below.

	particle	charge (e)	mass (MeV)
leptons	electron	-1	0.511
	neutrino ν_e	0	~ 0
	muon	-1	106
	neutrino ν_μ	0	< 0.17
	tau	-1	1777
	neutrino ν_τ	0	< 18.2
quarks	up	$+2/3$	1.5–5
	down	$-1/3$	3–9
	charm	$+2/3$	~ 1200
	strange	$-1/3$	60–170
	top	$+2/3$	174000
	bottom	$-1/3$	~ 4200
gauge bosons	photon γ	0	0
	Z	0	91187
	$W^\pm$	± 1	80410
	8 gluons g	0	0

The interactions between the fundamental particles are described by the Standard Model (SM). This model provides a unified description of the electromagnetic force as described by the theory of Quantum-Electrodynamics (QED) and the weak force that is responsible for radioactive decay. Leptons and quarks interact via the exchange of so-called gauge bosons which can be a photon γ, a neutral Z particle, or a charged $W^\pm$ particle. Quarks are held together in hadrons by a third force, the strong or colour force, that is described in the Standard Model by the theory of Quantum-Chromodynamics (QCD). This force is mediated by gluons which couple to the "colour charge" of the quarks. This "colour" can assume three values and plays a similar role as the electrical charge in QED. Coloured particles, however, cannot exist freely in nature in contrast to electrically charged particles.

[3]We leave the issue of neutrino mass aside.

To study the properties of fundamental particles large accelerators are required. They accelerate particles to very high energies before these are brought into collision. The particles emanating from the collisions are measured by large detectors. From many of such collisions properties about the structure and the fundamental interactions of the particles can be deduced.

This thesis focuses on the structure of the proton as it can be measured from positron-proton collisions registered by the ZEUS detector at the HERA collider in Hamburg. In the picture sketched above the proton consisted of only three quarks. Due to QCD, however, the proton is a dynamical system that contains a large number of mutually interacting quarks, antiquarks and gluons which are collectively known as partons. This system can be probed by a virtual gauge boson that is mediated between a positron and a proton in a process called deep inelastic scattering (DIS). In this way it is possible to measure the momentum distribution of the particles in the proton. When the gauge boson is a photon or a Z particle the process is called neutral current DIS and all quarks and antiquarks in the proton can take part in the interaction. In charged current DIS which will be the main subject of this thesis the gauge boson is a $W^{\pm}$ particle and only certain combinations of quarks and antiquarks can contribute to the cross section.

Chapter 1 will present the theoretical framework of deep inelastic positron-proton scattering and the structure of the proton. In chapter 2 the ZEUS detector is described followed by a brief exposé on event simulations in chapter 3. Chapters 4 and 5 concentrate on the selection of charged current events and the removal of backgrounds in the event sample. Since charged current events produced by a charged lepton beam have been observed for the first time at HERA this selection requires new techniques. The reconstruction of the kinematic variables of a charged current DIS event is the main subject of chapter 6. In chapter 7 the cross sections as a function of various kinematic variables are extracted from the data and compared to the Standard Model predictions. Finally, a few related topics like the extraction of the W mass are discussed in chapter 8.

Chapter 1

Deep inelastic scattering

1.1 Introduction

The internal structure of the proton can be investigated by exposing protons to a bombardment with pointlike particles. This bombardment can lead to a process called deep inelastic scattering (DIS). At the HERA collider in Hamburg DIS is realised by colliding highly energetic protons and positrons. In these collisions the positron and the proton interact via the exchange of a gauge boson. As a result the proton breaks up into a large number of particles and this debris can, in principle, be measured, together with the scattered positron. Two main types of interactions can be distinguished:

$$e^+ p \rightarrow e^+ X \quad \text{and} \quad e^+ p \rightarrow \bar{\nu}_e X \tag{1.1}$$

where X denotes the hadronic particles that result from the break-up of the proton. The first process is referred to as neutral current (NC) DIS as the exchanged gauge boson has no charge, being either a photon or a Z particle. In the second process a W boson is exchanged and the initial state positron yields a final state antineutrino. This process is called charged current (CC) deep inelastic scattering.

In figure 1.1 a schematic diagram is shown of the deep inelastic scattering process. The incoming positron e^+ with four-momentum k and the incoming proton p with four-momentum P interact via the exchange of a gauge boson (γ, Z, $W^\pm$). In the interaction the gauge boson does not couple to the proton as a whole but to one of its constituents. The other constituents in the proton do not participate in this part of the collision process. Therefore, the interaction can be regarded as elastic scattering between a positron and a parton in the proton. After the pointlike interaction the final state will contain a positron or an antineutrino, depending on the charge of the mediating gauge boson. The parton that was hit by the boson will be knocked out of the proton and hadronise into the so-called current jet. The other constituents of the proton that did not take part in the interaction will also hadronise and form the proton remnant.

The scale of the interaction, Q^2, is given by the square of the four-momentum q of the gauge boson:

$$Q^2 = -q^2 = -(k - k')^2 = -(P' - P)^2 > 0 \tag{1.2}$$

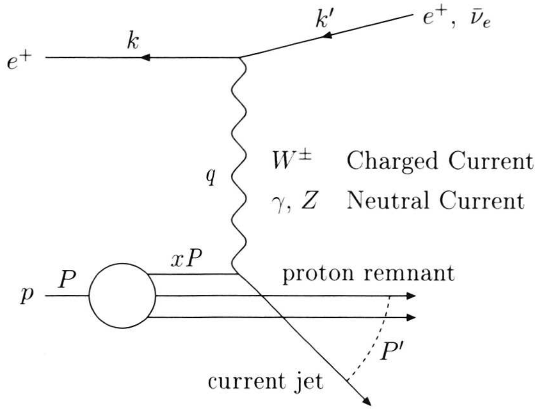

Figure 1.1: *a schematic view of a deep inelastic scattering event.*

Here k' is the four-momentum of the final state lepton and P' is the four-momentum of the hadronic final state consisting of the proton remnant and the current jet. The variable Q^2 sets the length scale λ at which the proton is probed:

$$\lambda \sim \frac{1}{\sqrt{Q^2}} \tag{1.3}$$

Here results will be presented that correspond to Q^2 values up to 20000 GeV^2 or, equivalently, to distances of the order of 10^{-3} fm, about one thousandth of the radius of a proton.

The measurements that will be presented are restricted to inclusive deep inelastic scattering. This means that no attempt is made to identify individual particles in the hadronic final state X. The kinematics of an inclusive DIS event are described by two independent variables, one of which is the scale Q^2. The second, independent, quantity that is often used is Bjorken-x which is defined as

$$x = \frac{Q^2}{2\,P\cdot q} \tag{1.4}$$

Note that both Q^2 and x are Lorentz-invariant quantities and thus valid in every reference frame. In the "infinite momentum" frame of the proton in which the masses and transverse momenta of the partons can be neglected, x can be identified as the fraction of the momentum of the proton carried by the struck parton. In the proton rest frame the variable y which is defined as

$$y = \frac{P\cdot q}{P\cdot k} \tag{1.5}$$

is equal to the fraction of the energy of the positron that is transferred to the proton. The three kinematic variables x, y and Q^2 are related as

$$Q^2 = s\,x\,y \tag{1.6}$$

where the square of the centre-of-mass energy $\sqrt{s}$ is given as $s = (P+k)^2$. This relation is only valid if $s \gg m_p^2$ with m_p the mass of the proton.

The invariant mass W of the hadronic final state X and thus the centre-of-mass energy of the V^*p system ($V = \gamma, Z, W^\pm$) is given by

$$W^2 = (P')^2 = Q^2 \frac{1-x}{x} + m_p^2 \tag{1.7}$$

1.2 Cross sections

The electroweak Born cross section for the neutral current DIS process $e^\pm p \to e^\pm X$ can be expressed in the following form

$$\frac{d\sigma^{NC}(e^\pm p)}{dx\, dQ^2} = \frac{2\pi\alpha^2}{x\, Q^4} \left[Y_+ F_2^\pm(x,Q^2) - y^2 F_L^\pm(x,Q^2) \mp Y_- xF_3^\pm(x,Q^2)\right] \tag{1.8}$$

where $Y_\pm = 1 \pm (1-y)^2$ and α is the QED coupling constant which equals $1/137$ at $Q^2 = 0$. The partonic content of the proton that enters the cross section is parametrised by three structure functions F_i. In the quark-parton model (see section 1.4) they are given by

$$F_2^\pm(x,Q^2) = \sum_q A_q(Q^2)\left[xq(x,Q^2) + x\bar{q}(x,Q^2)\right] \tag{1.9}$$

$$xF_3^\pm(x,Q^2) = \sum_q B_q(Q^2)\left[xq(x,Q^2) - x\bar{q}(x,Q^2)\right] \tag{1.10}$$

$$F_L^\pm(x,Q^2) = 0 \tag{1.11}$$

where the sum runs over all quark flavours q in the proton. The functions $q(x, Q^2)$ describe the density of quark flavour q inside the proton. The xF_3 term only has contributions due to pure Z exchange and due to the γZ interference. The structure function F_L arises from the exchange of longitudinal photons and is thus absent in the quark-parton model. The coefficients A_q and B_q contain the dependence on the vector and axial vector couplings of the photon and the Z particle to the scattered lepton and quark:

$$A_q(Q^2) = e_q^2 + 2\, e_l\, v_l\, e_q\, v_q\, \mathcal{P}(Q^2) + (v_l^2 + a_l^2)(v_q^2 + a_q^2)\, \mathcal{P}^2(Q^2) \tag{1.12}$$

$$B_q(Q^2) = 2\, e_l\, a_l\, e_q\, a_q\, \mathcal{P}(Q^2) + 4\, v_l\, a_l\, v_q\, a_q\, \mathcal{P}^2(Q^2) \tag{1.13}$$

The three terms in A_q describe the pure photon exchange, the γZ interference and the pure Z exchange, respectively. The latter two are heavily suppressed at low Q^2 due to the propagator function $\mathcal{P}(Q^2)$ given by

$$\mathcal{P}(Q^2) = \frac{1}{4\sin^2\theta_w \cos^2\theta_w} \frac{Q^2}{Q^2 + M_Z^2} \tag{1.14}$$

which contains the ratio of the photon propagator to the Z propagator. Likewise the xF_3 contribution to the cross section at low Q^2 is negligible.

The vector and axial vector couplings v_f and a_f can be expressed as

$$v_f = T_{3f} - 2\, e_f \sin^2\theta_w \quad ; \quad a_f = T_{3f} \tag{1.15}$$

In these equations e_f is the charge of fermion f in units of the proton charge. T_{3f} is the third component of the weak isospin vector: $T_{3f} = 1/2$ for ν, u and $T_{3f} = -1/2$ for e^-, d. Under charge conjugation it changes sign so that $T_{3f} = -1/2$ for $\bar{\nu}$, $\bar{u}$ and $1/2$ for e^+, $\bar{d}$.

The double differential electroweak Born cross sections for the charged current DIS processes $e^- p \to \nu_e X$ and $e^+ p \to \bar{\nu}_e X$ are given by

$$\frac{d\sigma^{CC}(e^\pm p)}{dx\,dQ^2} = \frac{G_F^2}{4\pi x}\frac{M_W^4}{(Q^2+M_W^2)^2}\left[Y_+ W_2^\pm(x,Q^2) - y^2 W_L^\pm(x,Q^2) \mp Y_- xW_3^\pm(x,Q^2)\right] \tag{1.16}$$

where $W_i^\pm$ are structure functions analogous to the F_i that appear in the neutral current DIS cross section, formula 1.8. The mass of the W boson is 80.41 GeV and the factor G_F is the Fermi coupling constant, equal to 1.6639×10^{-5} GeV^{-2} [1]. Note that in the absence of electroweak radiative corrections the following relation holds

$$\frac{G_F^2}{2\pi}M_W^4 = \frac{\pi\alpha^2}{4\sin^4\theta_w} \tag{1.17}$$

The charged current structure functions W_i are given by

$$W_2^+(x,Q^2) = \sum_{q=d,s,b} xq(x,Q^2) + \sum_{q=u,c,t} x\bar{q}(x,Q^2) \tag{1.18}$$

$$xW_3^+(x,Q^2) = \sum_{q=d,s,b} xq(x,Q^2) - \sum_{q=u,c,t} x\bar{q}(x,Q^2) \tag{1.19}$$

$$W_2^-(x,Q^2) = \sum_{q=u,c,t} xq(x,Q^2) + \sum_{q=d,s,b} x\bar{q}(x,Q^2) \tag{1.20}$$

$$xW_3^-(x,Q^2) = \sum_{q=u,c,t} xq(x,Q^2) - \sum_{q=d,s,b} x\bar{q}(x,Q^2) \tag{1.21}$$

while $W_L^\pm(x,Q^2) = 0$ in the quark-parton model. The contributions from bottom and top to the structure functions can safely be neglected in charged current scattering at HERA energies. Note that in neutral current scattering all quark and antiquark flavours contribute to the cross section while charged current scattering is only sensitive to certain combinations of quark and antiquark densities. Substituting the structure functions into equation 1.16 yields

$$\frac{d\sigma^{CC}(e^+p)}{dx\,dQ^2} = \frac{G_F^2}{2\pi x}\frac{M_W^4}{(Q^2+M_W^2)^2}\left[(1-y)^2(xd+xs)+x\bar{u}+x\bar{c}\right] \tag{1.22}$$

$$\frac{d\sigma^{CC}(e^-p)}{dx\,dQ^2} = \frac{G_F^2}{2\pi x}\frac{M_W^4}{(Q^2+M_W^2)^2}\left[(1-y)^2(x\bar{d}+x\bar{s})+xu+xc\right] \tag{1.23}$$

The factor $(1-y)^2$ is a direct consequence of the $V-A$ structure of the weak interaction.

Measurements of the charged current cross section and structure functions have been reported from neutrino scattering experiments on hydrogen, deuterium and other nuclear targets [3]. These fixed target experiments typically explore the region 0.1 GeV$^2 < Q^2 <$ 200 GeV^2

and $0.01 < x < 0.7$. First measurements of the charged current cross section at higher values of Q^2 have been presented previously by the ZEUS and H1 collaborations [4, 5, 6]. These measurements comprise both e^-p and e^+p scattering and extend the kinematic range by about two orders of magnitude in Q^2.

1.3 Electroweak radiative corrections

The expressions 1.8 and 1.16 for the neutral current and charged current DIS cross sections have to be modified to account for the presence of higher order electroweak interactions. In the analysis of the experimental data this additional contribution to the cross section has to be separated from the lowest order electroweak Born cross section in order to get the most direct information on the structure of the proton (see also section 7.3).

The electroweak radiative corrections for the charged current process have been calculated by two independent groups [7] and agree within 1%. The corrections can be divided in two classes. Firstly, there are corrections involving fermionic or bosonic loops and corrections due to the exchange of multiple intermediate vector bosons. The size of these corrections is dominated by the W self-energy and is of the order of a few percent and increases to about 10% at high y for $x > 0.9$.

Secondly, there are contributions due to the emission of a photon from either the lepton or the quark legs and due to photon emission from the exchanged W boson. These three contributions, however, cannot be separated as such in a gauge invariant way. Therefore, in theoretical calculations they are rearranged according to their dependence on the electrical charge of the incoming particles. This yields three terms that are referred to as the quarkonic part, the leptonic part and the interference term.

The quarkonic contributions contain terms proportional to $\log(Q^2/m_f^2)$ with m_f the mass of the incoming or outgoing quark. As discussed in the next section similar divergences appear in the QCD radiation of gluons, which are absorbed in the quark distribution functions. Therefore, also the quarkonic QED radiative corrections are chosen to be absorbed in this way. The interference term can be neglected as it only gives a contribution less than 1% for $x < 0.5$.

The leptonic part of the purely photonic radiative corrections contains terms proportional to $\log(Q^2/m_e^2)$ with m_e the electron mass. This part dominates the size of the total electroweak radiative corrections to the charged current cross section. For x around 0.1 the correction ranges from -20% at low y to 10% at values of y close to 1.

Currently, two programmes incorporating the full $\mathcal{O}(\alpha)$ electroweak corrections, EPRC [8] and HECTOR [9], are available. They have been compared in [10] and the agreement between the two is satisfactory except in the region where $x < 0.01$, $y < 0.05$ and in the region above $x = 0.9$ for all y where a maximum difference of 2% is observed. The drawback of these programmes, however, is that they are not suitable for experimental applications since the possibility to apply experimental cuts has not been implemented. Moreover, they can only use kinematic variables calculated with the information from the scattered lepton while in the experimental analysis of charged current DIS the hadronic side of the event has to be used (see also chapter 6). These two restrictions are circumvented in the Monte Carlo programme HERACLES [11]. This programme, however, uses an approximation of the radiative corrections as it neglects the interference and the quarkonic terms in the photonic corrections. An agreement with EPRC is achieved at the level of 1% at low x but a difference of the order of 3% is observed at $x = 0.4$ [12].

1.4 Quark-parton model

In the naive quark-parton model the proton is regarded as a collection of non-interacting partons which can be identified with the quarks. The lepton-proton scattering cross section is then an incoherent sum over all elastic lepton-parton scattering cross sections. For neutral current scattering in the absence of Z exchange this yields

$$\frac{d\sigma}{dx\,dQ^2} = \frac{4\pi\alpha^2}{x\,Q^4} \sum_f \int_0^1 d\xi\, q_f(\xi)\, e_f^2\, \frac{\xi}{2} \left[1 + (1-y)^2\right] \delta(x-\xi) \tag{1.24}$$

where the sum runs over all quark flavours f in the proton with charge e_f. The probability density to find a quark in the proton with a fraction ξ of the total proton momentum is given by $q(\xi)$. It can be shown that in this model the longitudinal structure function F_L vanishes as a consequence of the spin-1/2 nature of the quarks. The model also predicts that the momentum distribution functions q_f and thus the cross section only depend on one dimensionless variable. This is called Bjorken scaling and is indeed observed in the data at $x \sim 0.1$.

For lower and higher values of x severe violations of Bjorken scaling are observed and the cross section shows a dependence on the scale Q^2 of the interaction. The quark-parton model can explain these scaling violations if interactions between the quarks in the proton are allowed. The quarks are confined to the proton by the strong interaction as described by the non-Abelian gauge theory QCD. In this theory the interaction between quarks proceeds via the exchange of gluons and is described by a Lagrange density that is invariant under local $SU(3)$ transformations. This $SU(3)$ invariance reflects the three varieties, or colour charges, with which quarks occur in nature. Local invariance necessitates the introduction of eight gluon fields. As the gluons themselves carry a colour charge they can interact mutually. This property of QCD can be traced back to the non-Abelian nature of the theory. In QED, the theory that describes electromagnetism using an Abelian gauge theory, the photon has no self-interactions.

Another consequence of the non-Abelian nature is the effect of antiscreening. In QED the effective electrical charge of an electron increases when the cloud of virtual charges around the electron is penetrated. This leads to a stronger coupling α if the scale Q^2 of the interaction increases. In QCD, however, the observed coupling to the quarks is reduced when the colour charge cloud is penetrated. This antiscreening effect is usually referred to as asymptotic freedom: the interaction becomes weaker at higher Q^2 or, equivalently, at shorter distances.

Antiscreening is quantified by calculating virtual corrections to the $gq\bar{q}$ vertex which is basically the value of the coupling constant α_s. To regularise the singularities a renormalisation scale μ_R^2 has to be introduced. As physical observables cannot depend on an arbitrary scale it follows, via the renormalisation group equations, that the effective couplings α_s at different values of the scale μ_R^2 are related. In DIS this scale is usually chosen as Q^2. The running coupling constant α_s can then be expressed as

$$\alpha_s(Q^2) = \frac{4\pi}{(11 - 2n_f/3)\,\log(Q^2/\Lambda^2)} \tag{1.25}$$

where n_f is the number of quark flavours. Λ is a parameter that sets the scale above which perturbative QCD can be applied. Measurements indicate a value of Λ between 200 MeV and 400 MeV.

Although the coupling of the probing gauge boson to the quarks is now dependent on the scale of the interaction incoherence between the partons in the proton is still assumed. This leads to the important principle of factorisation: the cross section for lepton-proton scattering can be written as a convolution of universal parton density functions describing the structure of the proton and a hard scattering process that describes the interaction between the lepton and the quarks in the proton

$$\sigma(x, Q^2) = \sum_f \int_x^1 \frac{dz}{z}\,\hat{\sigma}(z, Q^2, \mu_F^2)\,q_f(\frac{x}{z}, Q^2, \mu_F^2) \tag{1.26}$$

Here $\hat{\sigma}$ is the hard scattering cross section calculable in perturbation theory. The soft parton density functions q_f describe the non-perturbative part of the interaction and have to be measured experimentally. Via a redefinition of the parton densities collinear divergences originating from gluon radiation off quarks are absorbed in q_f. The factorisation scale μ_F^2 defines the boundary between hard and soft physics. In deep inelastic scattering this scale is usually chosen as $\mu_F^2 = \mu_R^2 = Q^2$. Factorisation implies that the structure functions F_i and W_i can be written as a convolution of parton density functions and a hard interaction which is denoted by the coefficient function $C_{i,f}$:

$$F_i(x, Q^2) = \sum_{n=1,\ldots} \left(\frac{\alpha_s(Q^2)}{2\pi}\right)^{n-1} \sum_{f=q,\bar{q},g} \int_x^1 \frac{dz}{z}\,C_{i,f}^{(n)}(z, Q^2)\,q_f(\frac{x}{z}, Q^2) \tag{1.27}$$

and similarly for $W_i(x, Q^2)$. Here n represents the order of perturbation theory in the strong coupling constant $\alpha_s(Q^2)$. Beyond the lowest order the parton densities and coefficient functions become specific for the factorisation scheme that is used. The $\overline{\text{MS}}$ scheme is favoured in the theoretical literature. For deep inelastic scattering, however, the DIS scheme is sometimes more convenient. In the latter scheme the coefficient functions for the purely electromagnetic structure function F_2 are zero in second and higher orders in perturbation theory.

To first order in α_s the processes responsible for parton interactions are gluon radiation $q \to q\,g$ from quarks or antiquarks, gluon pair production $g \to g\,g$ and quark pair production $g \to q\,\bar{q}$. The observed scaling violations can be explained intuitively by these processes. Consider a photon (or a Z or $W^\pm$ particle) at a certain scale Q_0^2 (figure 1.2). At this scale the photon probes the proton, with a finite resolution proportional to $1/\sqrt{Q_0^2}$, and sees for example a gluon but no interaction takes place. At a higher scale $Q^2 \gg Q_0^2$ the proton is probed with an improved resolution. If there would be no QCD radiation the photon would still see the same gluon distribution leading to exact scaling. However, due to radiation there is a certain probability that the photon will interact with one of the quarks from a virtual quark-antiquark

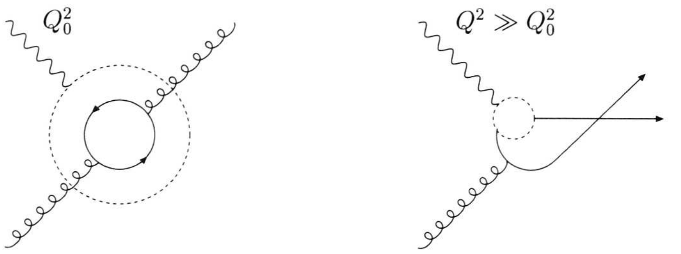

Figure 1.2: *an illustration of the Q^2 dependence of the observed proton structure. In the left plot the proton is probed by a photon at a scale Q_0^2 but no interaction takes place between the photon and the gluon. As the scale increases to $Q^2 \gg Q_0^2$ as in the right plot the photon sees a virtual quark-antiquark pair into which the gluon might fluctuate. The dotted circles indicate the minimum length scale that can be resolved by the photon.*

pair in which the gluon fluctuates. Thus a Q^2 dependence is introduced which gives rise to scaling violations.

The evolution of the quark and gluon densities $q_f(x, Q^2)$ and $g(x, Q^2)$ in the proton as a function of Q^2 is governed by the DGLAP equations [13]:

$$\frac{dq_f(x,Q^2)}{d\log Q^2} = \frac{\alpha_s(Q^2)}{2\pi}\int_x^1 \frac{dz}{z}\left[q_f(z,Q^2)\,P_{qq}\left(\frac{x}{z}\right) + g(z,Q^2)\,P_{qg}\left(\frac{x}{z}\right)\right] \tag{1.28}$$

$$\frac{dg(x,Q^2)}{d\log Q^2} = \frac{\alpha_s(Q^2)}{2\pi}\int_x^1 \frac{dz}{z}\left[\sum_f q_f(z,Q^2)\,P_{gq}\left(\frac{x}{z}\right) + g(z,Q^2)\,P_{gg}\left(\frac{x}{z}\right)\right] \tag{1.29}$$

Equation 1.28 expresses the fact that a quark with momentum fraction x could have originated from a quark with a larger momentum z that radiated off a gluon or from a gluon with momentum z that produced a quark-antiquark pair. Analogously, the second equation describes the change in the gluon density due to gluon radiation from quarks or gluons. The functions P_{ab} are so-called splitting functions that are calculable from perturbative QCD [14]. For a variation per unit $\log Q^2$ the quantity $(\alpha_s(Q^2)/2\pi)P_{ab}(x/z)$ is the probability density of finding a parton a originating from a parent parton b with a fraction x/z of the momentum of the parent parton.

In the region of low Q^2 and high x, i.e. the region where W^2 is small, the structure functions get extra contributions originating from so-called higher twist effects. These originate from non-perturbative interactions between the scattered quark and the proton remnant. Usually these terms can be neglected as they vanish like $(1/Q^2)^k$, $k \geq 1$.

1.5 Parametrisation of parton densities

The variation of the parton densities with the scale Q^2 is described by the DGLAP equations. Thus if the parton densities are known at some initial scale Q_0^2 they can be predicted at any value of Q^2 in the region where perturbative QCD is applicable. The x dependence of the parton densities, however, is not predicted by QCD. Usually a functional form is assumed for the parton densities at Q_0^2 that describes the behaviour as a function of x. This functional form is then fitted to a wide variety of data including the fixed target and HERA data on structure functions, the inclusive jet production measurements of Tevatron and data on Drell-Yan and W production at hadron-hadron colliders.

One of the groups that perform this kind of global fits is the CTEQ collaboration [15]. At an input scale $Q_0^2 = 2.56$ GeV^2 this group uses the following functional form to parametrise the gluon density $g(x, Q^2)$:

$$xg(x, Q_0^2) = A_0\, x^{A_1}(1-x)^{A_2}(1 + A_3\, x^{A_4}) \tag{1.30}$$

with five free parameters A_i. The valence quark densities $u_v = u - \bar{u}$ and $d_v = d - \bar{d}$, the sea quark density and the $\bar{u} + \bar{d}$ density are parametrised similarly, each with five parameters. The $\bar{d} - \bar{u}$ density is parametrised differently as

$$\bar{d} - \bar{u} = A_0\, x^{A_1}(1-x)^{A_2}(1 + A_3\sqrt{x} + A_4\, x) \tag{1.31}$$

Some of the free parameters are constrained when the momentum sum rule and valence quark sum rules are imposed. Two sets of parametrisations that are frequently used are the so-called CTEQ4M and CTEQ4D parametrisations which are obtained as a result of a full NLO QCD fit to the data in the $\overline{\mathrm{MS}}$ and DIS scheme, respectively. Also the CTEQ4L parametrisation will be used which is an identical analysis in leading order QCD.

In figure 1.3 the u valence and d valence quark distributions u_v and d_v, the sea quark distribution and the gluon distribution are shown as a function of x at $Q^2 = 100$ GeV^2 and at $Q^2 = 30000$ GeV^2. Note that the variation in the parton densities with Q^2 is only weak, illustrating that the DGLAP evolution is a function of $\log Q^2$. Around $x = 0.5$ the u_v distribution is dominating, being about an order of magnitude larger than the d valence distribution. The sea quark distribution is on its turn an order of magnitude smaller than the d_v distribution while the magnitude of the gluon density is comparable to the sea quark distribution. The neutral current DIS cross section in the high x region is therefore expected to be dominated by the u quark distribution, also because $|e_u| = 2|e_d|$. The e^+p charged current cross section is dominated by the d quark distribution as the u quark does not contribute. On the other hand, the e^-p charged current cross section is dominated by the u quark density yielding a cross section that is about an order of magnitude larger than for e^+p scattering.

Two other groups also perform global fits to the data. The MRS group uses very similar functional forms to parametrise the parton density functions (PDFs). Here the rather old MRSA and MRSH and the more recent MRST parametrisations will be considered [16, 17]. These parametrisations use an input scale somewhat different from CTEQ, $Q_0^2 = 4$ GeV^2 for MRSA and MRSH and 1 GeV^2 for MRST.

The GRV group [18] has a different approach in determining the parton densities. The original idea behind these parametrisations is that at some very low scale Q^2, around 0.30 GeV^2, the proton consists only of valence quarks. As Q^2 increases the gluons and sea quarks are generated dynamically through gluon radiation and splitting. It turns out, however, that it is not possible to describe all relevant data with these assumptions only. To obtain a good description it is necessary to introduce a valence like gluon and sea quark density at the initial scale Q_0^2.

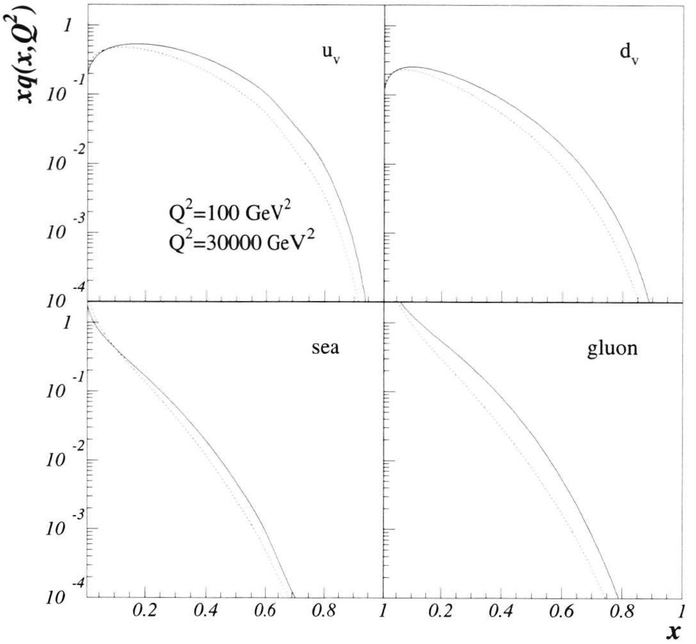

Figure 1.3: *several parton density distributions as parametrised by the CTEQ4D set as a function of x for $Q^2 = 100$ GeV^2 and $Q^2 = 30000$ GeV^2. Shown are the valence u and valence d quark distribution, the sea quark distribution and the gluon density.*

1.6 NLO QCD fit

The standard parton distribution sets of the CTEQ, MRS and GRV groups do not provide information on the uncertainties in the parton densities and thus on the predicted cross sections. This information is crucial to judge possible deviations of the data from the Standard Model expectations. A NLO QCD fit to HERA and fixed target data has been performed [19] which does contain estimates of the uncertainties in the extracted parton density functions. This fit takes into account the statistical and systematic errors on the data and all correlations.

The data that go into the fit are in the first place the measurements of the proton structure function F_2^p from ZEUS [20] and H1 [21]. To constrain the fit at high x also the fixed target measurements of the proton and deuteron structure functions F_2^p and F_2^d by E665, NMC, BCDMS and SLAC [22] are included. Furthermore, the NMC measurements [23] of the ratio F_2^d/F_2^p are used as well as data on $xF_3^{\nu Fe}$ from CCFR [24]. Finally, the data of E866 [25] on $x(\bar{d}-\bar{u})$ in the range $0.02 < x < 0.345$ are included in the fit. This asymmetry is obtained from measurements of Drell-Yan production in pp and pn collisions. These data are particularly interesting as they provide a constraint on the $\bar{d}$ density at high x, a region that is also probed by the charged current DIS measurements at HERA. Note that the results of the measurements of the charged current cross section that will be presented are not included in the fit.

The data on xF_3, F_2^d and F_2^d/F_2^p are corrected for nuclear effects [19]. In addition, the proton and deuteron structure functions are corrected for higher twist (HT) contributions which become important at high x and low Q^2. The effect of higher twist contributions to the leading twist (LT) structure functions F_2^{LT} which obey the DGLAP evolution is parametrised as

$$F_2^{HT} = F_2^{LT}\left[1 + H(x)/Q^2\right] \tag{1.32}$$

where $H(x)$ is a fourth degree polynomial depending on x. It is assumed that $H(x)$ is the same for proton and deuteron which implies that F_2^d/F_2^p is not affected by higher twist contributions. No separate corrections for target mass effects are applied so that they are effectively included in $H(x)$. To reduce the sensitivity to the higher twist and target mass effects a cut $W^2 > 7$ GeV^2 is applied to the data.

The QCD evolutions as governed by the DGLAP equations and the structure function calculations are performed with the programme QCDNUM [26]. The fit uses 28 free parameters that are evaluated at an input scale Q_0^2 chosen as 4 GeV^2. A χ^2 minimisation is used to find the best values of these parameters yielding a minimum $\chi^2 = 1540$ for 1578 data points. The estimated error on the results of the fit comprises the statistical and systematic errors on the measurements, but also errors originating from the uncertainties in the strong coupling constant $\alpha_s(M_Z^2)$, the nuclear corrections and the charm threshold. Additional errors are included as the envelop of the results of the nominal fit and various alternative fits. These alternative fits use e.g. a different input scale ($Q_0^2 = 7$ GeV^2) or different cuts on the invariant mass W.

Figure 1.4 shows the prediction of the fit for the ratio d/u, or rather $(d+\bar{d})/(u+\bar{u})$, together with the estimated error. The ratio as obtained in the fit shows a behaviour $d/u \to (1-x)^{-1}$ as x approaches 1 in contrast to the CTEQ group that finds $d/u \to 0$ at large x. The possibility of a larger d/u ratio than previously assumed has been of interest in recent years, see for example [27] and [28]. In [27] a reanalysis of deuteron data is presented that takes into account the most recent knowledge of Fermi motion, nuclear binding effects and nucleon off-shell effects in the deuteron. This analysis yields a non-vanishing d/u ratio as x approaches 1. In [28] a NLO analysis is performed on the NMC F_2^d/F_2^p data [23] to extract d/u. From these data the ratio F_2^{p+n}/F_2^p is extracted by applying the nuclear binding correction F_2^d/F_2^{n+p} that has been extracted emprically from SLAC data [29]. At high x this corrected F_2^{p+n}/F_2^p is not described by the standard parton density parametrisations of MRS and CTEQ. Since the u density is relatively well constrained by the HERA measurements a correction term is added to the d density which is parametrised as

$$xd' = xd + B(x+1)xu \tag{1.33}$$

with $B = 0.1 \pm 0.01$. This modification also yields a finite d/u ratio of 0.2 ± 0.02 when x approaches 1 as illustrated in figure 1.4. However, the NLO QCD fit [19] obtains a similar result without any modification. If a term as in equation 1.33 is added in the fit with B as a free parameter a value $B = -0.02 \pm 0.01$ is found, thus close to zero. Of course, in view of the large uncertainty in the d/u ratio at high x it is not possible at present to discriminate between the various scenarios.

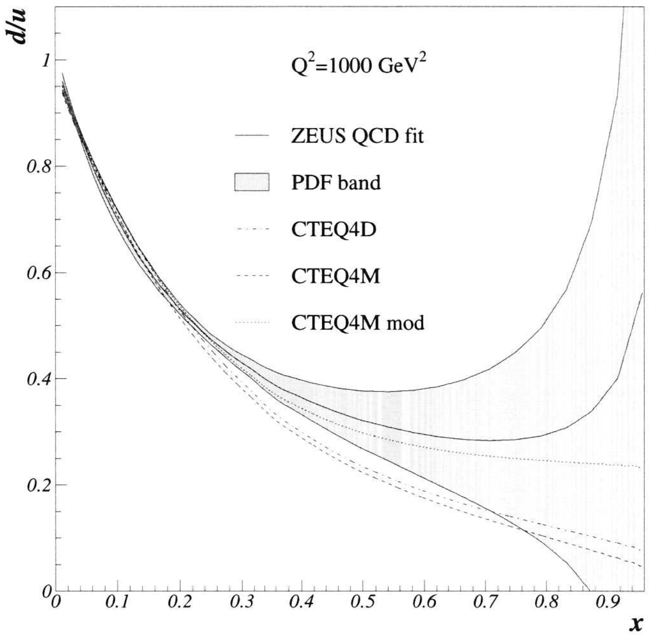

Figure 1.4: *the ratio $(d+\bar{d})/(u+\bar{u})$ as a function of x at $Q^2 = 1000$ GeV^2 as predicted by the NLO QCD fit (full line). The shaded band shows the uncertainty on the predicted ratio. The other curves show the LO CTEQ4D prediction (dot-dashed curve), the LO CTEQ4M prediction (dashed curve) and the prediction of CTEQ4M modified according to [28] (dotted curve).*

Chapter 2

HERA and the ZEUS detector

2.1 The HERA accelerator

The HERA (Hadron Electron Ring Accelerator) facility is the first accelerator in the world that makes it possible to perform deep inelastic positron-proton scattering experiments with colliding beams. The positron beam has an energy of 27.5 GeV while the protons have an energy of 820 GeV yielding a centre-of-mass energy of 300 GeV. Both beams are stored in 220 bunches that are spaced 96 ns apart, corresponding to 29 m. The maximum Q^2 value that can be reached is 90200 GeV^2. This implies an extension of the kinematic plane by roughly two orders of magnitude both in $1/x$ and Q^2 as compared to previous fixed target experiments.

A layout of the HERA ring and the four experiments that employ one or both beams is shown in figure 2.1. Two multipurpose experiments, ZEUS and H1, use both the positron and proton beam. Their measurements do not only include measurements of the proton structure but also cover a wide scala of other processes ranging from soft physics to very hard interactions. HERA-B is a fixed target experiment that will study $\mathcal{CP}$ violation in the B-system. The HERMES experiment is an internal target experiment in the positron beam that focuses on measuring the spin distributions of the quarks and gluons in protons and neutrons.

Operation of HERA started in 1992 with an electron and a proton beam. In the course of 1994 the machine switched to a positron beam because the electron beam had too short a lifetime due to positively charged dust in the ring. HERA continued running with positrons until 1997. This analysis will only concentrate on the positron-proton measurements from 1994 to 1997. The total integrated luminosity taken in this period amounts to 47.53 pb^{-1} (2.99 pb^{-1} in 1994, 6.31 pb^{-1} in 1995, 10.55 pb^{-1} in 1996 and 27.68 pb^{-1} in 1997). In figure 2.2 the integrated luminosity is shown versus days of running for each of the years of data taking.

2.2 The ZEUS detector

Looking at the ZEUS detector (figure 2.3) the first thing that draws the attention is the asymmetric design. This is due to the fact that the centre-of-mass system does not coincide with the laboratory system. As the protons come from the right the particles in the final state will generally be boosted to the left. Thus a detector elongated in that direction is required.

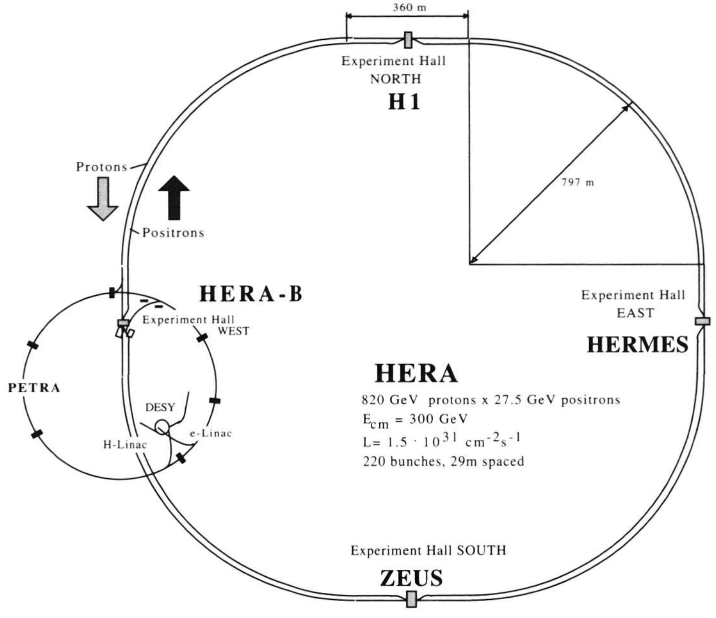

Figure 2.1: *layout of the HERA collider.*

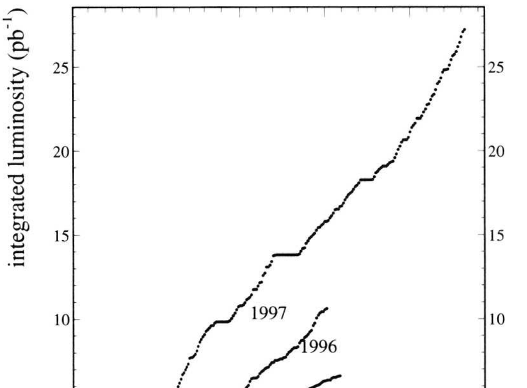

Figure 2.2: *luminosity in pb^{-1} useful for physics analyses versus the days of running as collected by the ZEUS detector during the years 1993 to 1997.*

In the heart of the detector, closest to the interaction point, is a vertex detector (VXD), which is surrounded by a drift chamber (CTD) and two tracking devices for forward and very backward going particles (FDET and RTD). The tracking system is surrounded by a solenoidal magnet that provides a longitudinal field of 1.43 T.

The tracking system is enclosed by the calorimeter (CAL) that is segmented in a forward (FCAL), barrel (BCAL) and rear (RCAL) sector. An iron yoke that acts as a return path for the magnetic flux is equipped with a backing calorimeter (BAC). A muon detection system (FMUON, BMUI, BMUO, RMUI, RMUO) is partially mounted on this yoke. The effect of the magnet system on the beam is compensated by an opposite field from a special magnet (Compensator). The veto wall shields the detector from particles in the proton beamhalo and provides a veto for beam-gas interactions.

A detailed description of the ZEUS detector can be found in [30]. In the remainder of this chapter only the components that play a role in the analysis that is presented here will be briefly described.

2.3 ZEUS coordinate system

The coordinate system of the ZEUS detector is chosen such that the z-axis is pointing along the proton beam direction. The x-axis lies in the HERA accelerator plane and is pointing towards the centre of the ring. To get a right-handed coordinate system the y-axis is pointing upwards, perpendicular to the accelerator plane. The point $(0, 0, 0)$ is the nominal interaction point where the proton and positron bunches collide.

Often spherical coordinates (R, θ, ϕ) will be used instead of the Cartesian coordinate system. Here R is the distance to the nominal interaction point. The polar angle θ is measured with respect to the positive z-axis, which means that the forward part of the detector is situated at a low angle θ. The azimuthal angle ϕ is measured with respect to the x-axis. Sometimes, instead of θ, the pseudorapidity η is used. It is defined as

$$\eta = -\log\left(\tan\frac{\theta}{2}\right) \tag{2.1}$$

The advantage of using pseudorapidity instead of polar angle θ is that event shapes are invariant in η under Lorentz boosts in the longitudinal direction.

2.4 Calorimeter

The uranium calorimeter (CAL) [31] is the key component for this analysis as the energy measurement is of crucial importance. Therefore, the description will be more extensive than for the other components afterwards. The CAL consists of layers of depleted uranium that act as absorber interspersed with plastic scintillator material. It turns out that choosing a uranium thickness of 3.3 mm and a scintillator thickness of 2.6 mm yields an equal response to positrons and hadrons. Under test beam conditions the energy resolution is then $\sigma(E)/E = 18\%/\sqrt{E}$ for positrons and $\sigma(E)/E = 35\%/\sqrt{E}$ for hadrons.

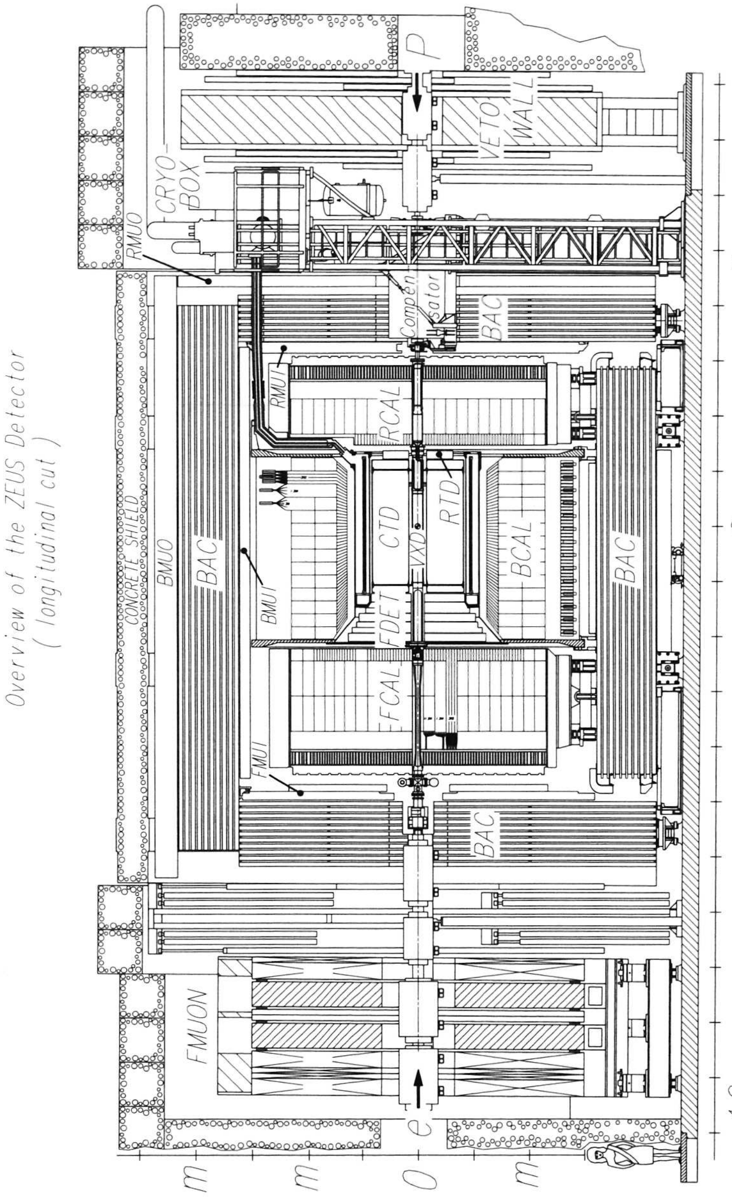

Figure 2.3: *cross section along the beamline of the ZEUS detector. The dimensions of the apparatus are compared to an average-sized charming Miss ZEUS.*

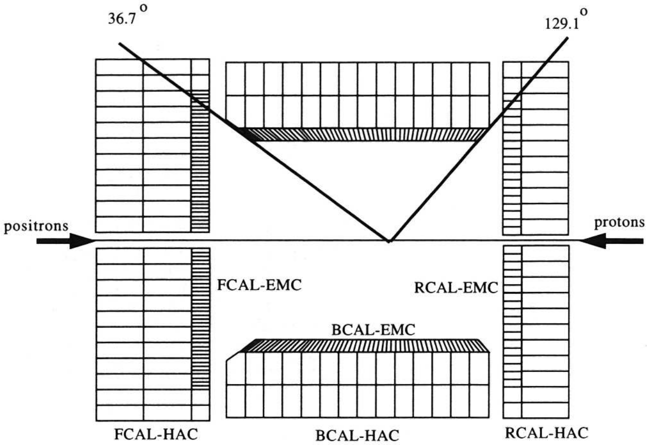

Figure 2.4: *schematic layout of the ZEUS uranium calorimeter.*

The calorimeter covers 99.7% of the total solid angle. It is divided into three overlapping sections, the forward calorimeter (FCAL) covering the polar angle range $2.6^\circ < \theta < 39.9^\circ$, the barrel calorimeter (BCAL) covering $36.7^\circ < \theta < 129.1^\circ$ and the rear calorimeter (RCAL) covering $128.1^\circ < \theta < 176.2^\circ$ (see figure 2.4). Each calorimeter part is divided into electromagnetic (EMC) and hadronic (HAC) sections. These sections are further subdivided into cells of 5×20 cm^2 (10×20 cm^2 for the RCAL) for the EMC and 20×20 cm^2 for HAC sections. A HAC section is combined with four EMC cells (FCAL and BCAL) or two EMC cells (RCAL) to form a so-called tower. The HAC sections in BCAL and FCAL are split into two separate units. The FCAL and RCAL each contain 23 modules, each with a width of 20 cm, that accommodate the towers, varying from 11 towers in the outermost modules to 23 for the modules in the centre. The BCAL consists of 32 wedge shaped modules that each span 11.25° in azimuth. To prevent particles escaping through the intermodular gaps the BCAL modules are rotated by 2.5° around an axis parallel to beampipe. The depths of the FCAL, BCAL and RCAL are 7λ, 5λ and 4λ respectively, where λ is the interaction length. A length of 7λ is enough to contain 95% of the energy of a few hundred GeV hadronic shower [32]. The depths of the EMC sections in radiation lengths (X_0) are $26X_0$, $23X_0$ and $26X_0$ for FCAL, BCAL and RCAL respectively, which is enough to absorb electromagnetically showering particles. In figure 2.5 the shower development for various types of particles is drawn schematically. The figure illustrates that the difference in shower shape can be used for particle identification.

To improve the ability to distinguish hadronic and electromagnetic energy deposits in the EMC section of the forward and rear calorimeter planes of 3×3 cm^2 silicon diodes have been installed inside the calorimeter. This hadron electron separator (HES) is placed after $3.3X_0$ in both the FCAL and the RCAL, as viewed from the interaction point. A high signal in the HES indicates an early showering. This is more likely to originate from an electromagnetic shower than from a hadronic shower.

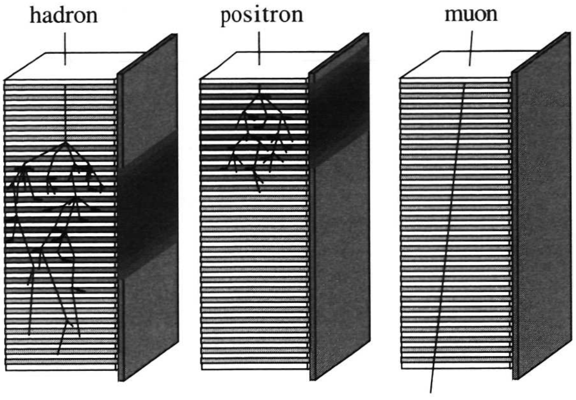

Figure 2.5: *different types of shower shapes in the calorimeter. Three towers are drawn with the wavelength shifter on the right-hand side. Also shown is the sandwich structure of the uranium and scintillator layers. A hadron produces a wide shower starting only after having passed the first part of the tower. A positron produces a narrow shower that will be contained in this section. The energy left behind by a muon will be equally distributed over the whole tower. (At very high energy it becomes more likely that the muon also produces bremsstrahlung photons while traversing the calorimeter.)*

In 1995 a presampling detector [33] was installed on the front surfaces of the forward and rear calorimeter. The two presamplers consist of 576 scintillator tiles with transverse dimensions of 20×20 cm^2. They measure the shower multiplicity of a particle entering the calorimeter. This multiplicity is correlated with the energy loss of the particle in the inactive material between the interaction vertex and the surface of the calorimeter. This information helps to improve the energy measurement and resolution of positrons. For hadronic showers there is, however, no significant improvement in the resolution. Therefore, the presampler is not used here.

Calorimeter cells are read out by two photomultipliers (PMTs) that collect the signals from wavelength shifters along both sides of the cell. This dual read out is used to determine the impact position of the energy deposit in the cell. A further advantage is that in case of failure of one PMT the energy can still be measured by the other PMT.

2.4.1 Calorimeter noise

Noisy cells might give a bias in the reconstruction of the kinematics of a charged current event. Especially at low y a noisy cell in the rear calorimeter might give a considerable contribution to the measured y. Therefore, certain cuts are applied on individual calorimeter cells.

The main source of noise is radioactive decay of uranium in the calorimeter. This type of noise is suppressed by requiring an energy deposit of at least 60 MeV in EMC and 110 MeV in HAC cells. These numbers are obtained from studies of empty events in which any energy deposit must be caused by noise. If the cell is isolated, i.e. there are no surrounding cells with energy, the thresholds are raised to 100 MeV for EMC cells and 150 MeV for HAC cells.

Another source of noise are sparks caused by the electrical discharge of one of the PMTs of a calorimeter cell. This will result in a signal in the cell, but this signal will have a large imbalance *imb*, which is defined as the difference in energy recorded in the two PMTs. Usually the imbalance is divided by the sum of the energies

$$\frac{imb}{E_{cell}} = \frac{E_{PMT1} - E_{PMT2}}{E_{PMT1} + E_{PMT2}} \tag{2.2}$$

where E_{PMT1} and E_{PMT2} are the energies detected by the two PMTs and $E_{cell} = E_{PMT1} + E_{PMT2}$. The background from sparks is reduced by requiring $|imb/E_{cell}| < 0.8$ if the cell is isolated and has an energy of more than 200 MeV. This cut does not work for cells with a bad PMT since then the imbalance is set to zero by the reconstruction software. Such a bad cell is rejected if it is isolated and has more than 100 GeV of energy.

Although the uranium noise is deteriorating the reconstruction of kinematic variables it has the large advantage that it can be used for calibration purposes. A daily measurement of the integrated uranium current results in a calibration that is constant over a running period.

2.4.2 Calorimeter timing

The time at which a particle enters a cell is extracted from the shape of the pulse in the PMT. The error σ_t on this time can be parametrised as

$$\sigma_t(E) = 0.4 + \frac{1.4}{E^{0.65}} \text{ ns} \tag{2.3}$$

where E is the energy recorded in the PMT in GeV. The average calorimeter time is *not* simply the average time recorded by each individual cell relative to the time of the bunch crossing. Instead, each calorimeter cell has a local clock that has an offset such that a particle coming from an *ep* interaction at the nominal interaction point will arrive at time zero at that cell. These offsets are determined from the different geometrical positions of each cell.

The average time of (a section of) the calorimeter (R/B/FCAL) is calculated as an energy weighted average over the individual times of the PMTs in the section

$$t_{section} = \frac{\sum_{iPMT} w_i t_i}{\sum_{iPMT} w_i}; \quad \begin{array}{l} w_i = \min(E_{PMT}, 2 \text{ GeV}) \\ w_i > 0.2 \text{ GeV} \end{array} \tag{2.4}$$

At least two PMTs have to contribute to the calculation and the imbalance should be smaller than $0.35\,E_{PMT}$. Events that do not satisfy these conditions do not have a timing measurement in that particular calorimeter section.

Usually for a given run the times still do not peak around zero. This is due to run to run shifts in the proton and positron bunch crossing times. If for example the positron bunch is in time with respect to the HERA clock but the proton bunch is too late, the interaction will take place closer to the RCAL. When the positron is detected in the RCAL it will still arrive at a time around zero. On the other hand, the hadronic system which is measured mostly in the FCAL will be too late. To correct for this effect a special detector (the C5 detector) measures the offsets of the positron and proton bunches and this information is used to adjust the geometrical timing corrections for each calorimeter cell.

2.5 Inner tracking

The central tracking detector (CTD) [34] is the *omphalos* of the inner tracking system in ZEUS. It consists of nine so-called superlayers each with eight sense wires (see figure 2.6). Five of these superlayers have wires parallel to the beam and four have wires with a small angle ($\pm 5^{o}$) with respect to the beamline. The CTD covers the polar angle range between 15^{o} and 165^{o}. The interaction vertex is measured with a typical resolution of 0.4 cm in the beam direction and 0.15 cm in the transverse direction. The momentum resolution for tracks traversing all nine superlayers is $\sigma(p_T)/p_T = 0.005\, p_T \oplus 0.016$ (p_T is the transverse momentum in GeV).

The vertex detector (VXD) [35] is a high precision cylindrical wire drift chamber that is installed between the outer radius of the beampipe and the inner radius of the CTD. Its aim is to improve the vertex resolution to $\sim 50\ \mu$m by measuring r and ϕ of the traversing particles. Because of problems with the high voltage this detector was taken out before the 1996 running. Although the VXD performed quite well in 1994 it is excluded from the track reconstruction in this analysis in order to obtain a similar reconstruction for all the years under consideration.

The track measurement of particles in the rear direction is improved by the rear tracking detector (RTD). This detector consists of a single three layer planar drift chamber and covers the polar angle range $160^{o} < \theta < 170^{o}$. Since this detector has only been fully operational since 1995 and to reduce uncertainties in acceptance corrections it is not used in the track reconstruction in this analysis.

The small angle rear tracking detector (SRTD) [36] improves the position measurement of positrons that are scattered under very low angles ($\theta > 165^{o}$). This detector is mounted on the surface of the calorimeter and consists of two overlapping layers of scintillator strips, one layer with horizontal strips and one layer with vertical strips. The angular coverage is $162^{o} < \theta < 176^{o}$. Here the SRTD is only used in the online trigger to reject non-ep background.

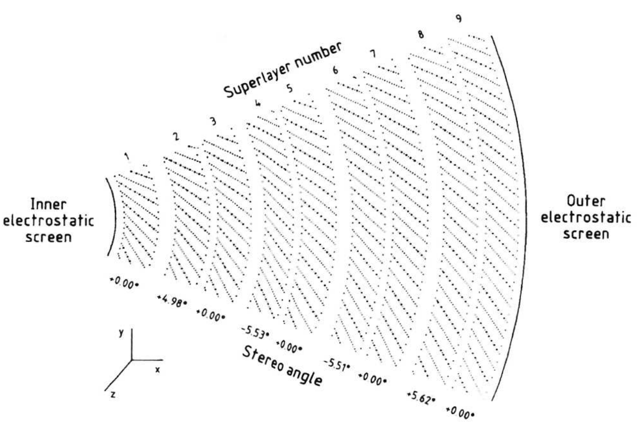

Figure 2.6: *layout of the nine superlayers in one octant of the CTD. The stereo angle of each superlayer is also indicated.*

The forward tracking detector (FDET) is used to measure very forward tracks and it covers the angular range $7^o < \theta < 28^o$. The FDET consists of three planar drift chambers of the RTD type which are interleaved with two transition radiation detectors (TRDs). Installation of this detector was completed during the 1995 running, but severe problems arose in the offline reconstruction due to the very high hit multiplicity. Therefore, the FDET is excluded from the track reconstruction in this analysis.

2.6 Muon detection

Forward going muons are measured by the forward muon detector (FMU). The FMU is equipped with four layers of limited streamer tubes (LSTs) with polar coordinate (ρ-ϕ) read out and four drift chambers that give a precise position measurement to evaluate the momentum of the muon. One LST and one drift chamber are mounted on the inner surface of the iron yoke while the other chambers and tubes are attached to an extra magnetic system outside the yoke that provides an additional toroidal field of 1.7 T. This detector covers the polar angle range $6^o < \theta < 20^o$ while two additional LST planes extend this region up to 32^o.

The barrel (BMU) and rear (RMU) muon detectors [37] cover the polar angle ranges $34^o < \theta < 135^o$ and $134^o < \theta < 171^o$, respectively. The barrel muon chambers do not have full coverage in ϕ as there is no bottom octant. The chambers consist of four double layers of LSTs placed both inside (BMUI, RMUI) and outside (BMUO, RMUO) the magnetised iron yoke (see figure 2.7). The wires are running parallel to the beam in the BMU and normal to it in the RMU. Signals are read out by TDC electronics on every wire and by ADCs on external strips orthogonal to the wires. A position resolution of ~ 1 mm is observed for the strip read out and ~ 2.5 mm for the wire read out.

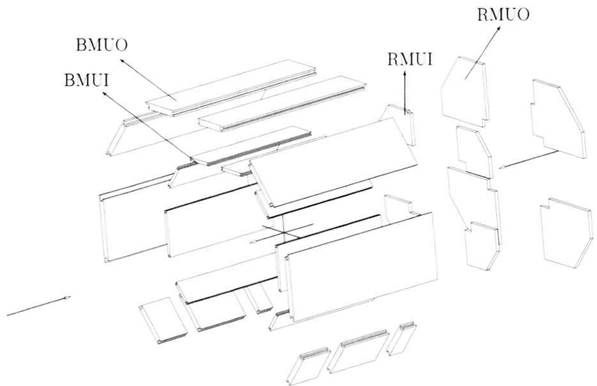

Figure 2.7: *exploded view of the barrel and rear muon detector. In this plot the protons come from the right and positrons from the left.*

2.7 Backing calorimeter

The iron yoke surrounding the main components of the detector is instrumented to allow an energy measurement for showers leaking from the back of the uranium calorimeter. This backing calorimeter (BAC) [38] consists of 7.3 cm thick iron plates interleaved with aluminium proportional chambers. Each chamber contains eight wires in 1.5×1.1 cm^2 tubes and is covered with a 50 cm long cathode pad. Neighbouring wire chambers are grouped together into non-projective wire towers that are 25 to 50 cm wide (2 to 4 modules) over the full depth of the BAC. Energy is measured by summing the analog signals from the wires leading to a resolution of $\sigma(E)/E = 120\%/\sqrt{E}$ for the BAC as stand-alone unit. The position coordinate corresponding to the deposited energy is obtained from 50×50 cm^2 pad towers formed by adding pads from 2 to 4 modules.

Every wire is also equipped with a digital hit read out that gives very precise information about the exact position in two dimensions but does not contribute to the energy measurement. This position measurement can be used for muon identification, especially in the bottom yoke where no muon chambers are present. Since the installation of the hit read out was only completed in 1996 it is not used in this analysis.

2.8 C5 counter and beampipe calorimeter

The C5 counter [40] is located at $z = -315$ cm, directly behind the RCAL. It consists of four scintillation counters, two placed above the beampipe and two below. Each pair is separated by 0.3 cm of lead. The counter records the arrival time of particles associated with the proton and positron bunches and is used to reject upstream proton-gas interactions.

In 1995 the C5 counter was replaced by a new version and the timing measurement was taken over by a new detector, the beampipe calorimeter (BPC) [39]. This detector is located at $z = -294$ cm and consists of two tungsten-scintillator sampling calorimeters that are located on either side of the beampipe. A new beampipe was installed with two exit windows in front of the BPC such that there is almost no inactive material between the interaction point and the BPC. Apart from a timing measurement the main motivation for the BPC is the extension of the kinematic plane to low x and Q^2 by measuring positrons that are scattered under very small angles.

2.9 Luminosity monitor

The luminosity monitor consists of a lead-scintillator photon calorimeter (LUMI$_\gamma$) positioned at $z = -107$ m (see figure 2.8). It accepts bremsstrahlung photons that are produced at an angle below 0.5 mrad with respect to the positron beam with an efficiency of 98% [40]. Under test beam conditions the calorimeter has an energy resolution of $\sigma(E)/E = 18\%/\sqrt{E}$. An additional electromagnetic calorimeter (LUMI$_e$) located at $z = -35$ m detects positrons with energies in the range 7 to 18 GeV produced at angles up to 5 mrad with respect to the positron beam direction.

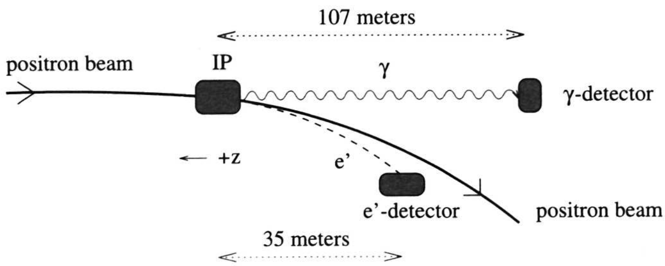

Figure 2.8: *schematic view of the positioning of the LUMI detectors with respect to the nominal interaction point IP.*

The luminosity is measured using the Bethe-Heitler bremsstrahlung process $e\,p \to e\,p\,\gamma$. The cross section for this process is very accurately known [41] and contributions from higher order effects are less than $\sim 0.3\%$. The photon is measured in the photon calorimeter and the luminosity is then determined as the number of events produced by the bremsstrahlung process divided by the cross section. The largest errors on the determination of the luminosity come from the uncertainties in the calibration of the LUMI$_\gamma$ detector and the photon acceptance. The LUMI$_e$ detector provides an independent but less accurate measurement of the luminosity.

2.10 Trigger system

Most of the events detected by ZEUS are not coming from *ep* collisions but from beam-gas interactions. As it is impossible to write all these events to the storage devices an online selection is performed by means of a three level triggering system that reduces the output rate to an acceptable level of about 5 Hz. This trigger chain is drawn schematically in figure 2.9.

The first level trigger (FLT) has to cope with an input rate of ~ 10 MHz, i.e. one event every 96 ns, which is the time between two bunch crossings. The data are stored in a pipeline for about 5 μs while the FLT calculations are being performed on a subset of these data. Each component completes its internal calculations in 1 to 2.5 μs and passes the result to the global first level trigger (GFLT). The GFLT calculations take an additional 1.9 μs (20 bunch crossings) before a decision is issued. If the decision is positive the data are transported from the pipeline to buffers for processing by the second level trigger. The output rate of the FLT is about 1 kHz.

The data in the second level trigger (SLT) are digitised, which means that more precise calculations can be done. For each component these calculations are performed by a network of programmable transputers. The decision of each component is sent within ~ 5 ms to the global second level trigger (GSLT) that combines the component triggers and decides to keep or reject the event. The SLT reduces the rate further to 100 Hz.

After the GSLT has given a positive decision the digitised data are sent from the buffers to the event builder (EVB) that collects all data from all components into one event. This event is then passed to the third level trigger (TLT) that consists of a farm of SGI workstations. These machines run a version of the offline reconstruction package and reduce the output rate to 3–5 Hz. Accepted events are written to a storage device and can be used for physics analyses.

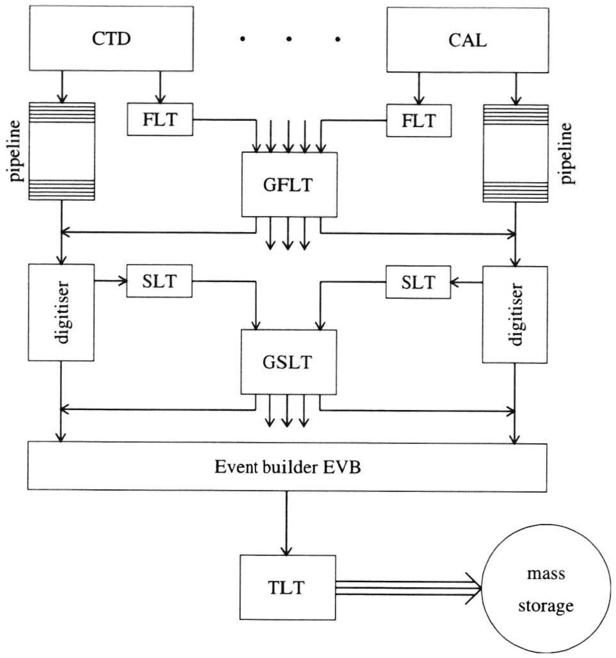

Figure 2.9: *schematic diagram of the trigger read out chain.*

2.11 Detector upgrades

After the shutdown of 1997/98 HERA switched back to an electron beam while the proton beam energy was raised to 920 GeV. At the end of 1998 ZEUS had been able to collect an integrated luminosity of ~ 4.5 pb^{-1}, which is far more than the harvest from the electron runs in 1992 and 1993. Electron running continued in the first part of 1999 but in the summer HERA went back to positrons once more.

Starting in the early summer of 2000 there will be a long shutdown that will be used for a major upgrade of HERA. The aim is to create an accelerator that will deliver an integrated luminosity of ~ 150 pb^{-1} per year. In ZEUS a new silicon vertex detector will be installed that will have a large angular acceptance ($10^o < \theta < 170^o$) and a longitudinal vertex resolution of 100 μm. This detector will be very useful for studies of heavy flavour physics, the measurement of F_2^{charm} in particular, which heavily relies on the tracking performance [42]. Charged current analyses will profit from the improved track reconstruction in the very forward direction.

ZEUS also plans to upgrade the FDET by replacing the drift chambers and radiators with straw drift tube planes interleaved with radiator material. The new detector will cover the angular range between 4^o and 28^o and a resolution of a few hundred micron seems to be feasible.

Chapter 3

Event simulation

Monte Carlo (MC) simulations are used to calculate the efficiency with which charged current DIS events are detected and to study smearing effects introduced by the detector resolution. They can also give an estimate of the contamination of the final signal sample with events coming from *ep* processes other than charged current DIS.

The generation of charged current DIS Monte Carlo data proceeds via the DJANGO 6.24 package [46]. This simulation programme forms an interface between the Monte Carlo programme LEPTO 6.5 [47] that describes lepton-nucleon scattering including QCD corrections and the generator HERACLES 4.5.2 [11] that incorporates the first order electroweak corrections. The generation of events breaks up into three successive steps:

- the hard lepton-nucleon scattering process.
- initial and final state QCD cascades.
- hadronisation.

This generation process is schematically drawn in figure 3.1. All steps are briefly described in the next three sections. The output of the generator is fed into the simulation of the ZEUS detector that is based on the GEANT [45] package. This simulation contains the most recent knowledge of the detector and the trigger system for a specific running period.

3.1 Hard interaction subprocess

The hard lepton-nucleon scattering subprocess $V^* q \rightarrow q'$ is simulated by LEPTO. Here V^* is the virtual gauge boson (γ, Z or W), q is a quark from inside the proton and q' is the scattered quark. This interaction is generated according to the lowest order Standard Model electroweak cross section in which contributions from the longitudinal structure function F_L are not included (see also section 7.4.6). The CTEQ4D [15] parton density function parametrisation is used to describe the parton content of the proton.

Contributions due to higher order QCD processes are simulated up to order α_s by including their exact matrix element (ME) expressions. These processes include boson-gluon fusion ($V^* g \rightarrow q \bar{q}$) and gluon radiation or QCD Compton scattering ($V^* q \rightarrow q' g$). The matrix

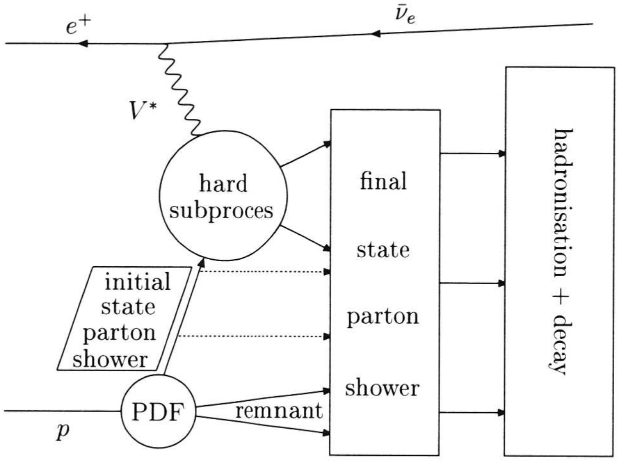

Figure 3.1: *schematic overview of the generation of a charged current DIS event.*

elements are divergent in the limit when the gluon energy or the $q'\,g$ opening angle vanishes. These divergences are partly absorbed in the parton density functions and partly cancelled by virtual corrections to the lowest order graph.

3.2 Parton shower development

In order to describe the development of the QCD cascade that follows the hard interaction the parton shower (PS) model is adopted [48]. In this model the development of a parton shower can be simulated to arbitrarily high order in α_s but only in the leading $\log Q^2$ approximation as governed by the DGLAP splitting functions. A distinction is made between initial state showers before the interaction with the gauge boson V^* and final state showers after the interaction.

The final state shower is modelled as a cascade initiated by the scattered quark. This quark has a timelike virtuality and will radiate partons with decreasing off-shell mass. These partons will also radiate partons. This process goes on until all partons have a virtuality below some cut-off, usually chosen around 1 GeV^2. This final state showering model has been well tested in $e^+\,e^- \rightarrow q\,\bar{q}$ processes at lower energy e^+e^- colliders and at LEP.

The initial state shower starts from an on-shell parton in the incoming proton. In each branching one parton becomes increasingly off-shell with a spacelike virtuality and the other parton is on-shell or has a timelike virtuality. This results in a spacelike parton (quark) interacting with the gauge boson while the timelike partons will develop like a final state shower. The most convenient way to describe the initial state shower is a backward evolution from the hard interaction vertex towards the on-shell parton in the proton. This makes the description more complicated than for the final state showering since, for example, in each branching the parton densities must be taken into account. Moreover, this model is less well tested by experiment as the measurements at hadron colliders are less "clean" than those at e^+e^- experiments.

A different formulation of the QCD cascade, i.e. of parton showers, is implemented in ARIADNE 4.0.8 [49]. This package uses the Colour Dipole Model that describes the QCD shower in terms of radiation from colour dipoles between partons. In a DIS event a dipole is created between the pointlike scattered quark and the extended proton remnant. This dipole will radiate gluons such that new independent dipoles are formed that in turn start to radiate. The ordering in the cascade is now in decreasing $p_\perp^2$ (transverse momentum squared) of the emitted parton instead of the virtuality of the emitter. ARIADNE explicitly incorporates the boson-gluon fusion process but assumes that the QCD Compton process is implied in the dipole radiation.

3.3 Hadronisation

Whereas the showering of partons can be modelled with perturbative QCD the hadronisation phase of the interaction has to be described by non-perturbative processes. Both ARIADNE and LEPTO use the LUND string model as implemented in JETSET/PYTHIA 7.4 [50] to simulate the hadronisation. In this model strings are stretched between colour triplet (quark, antidiquark) and colour antitriplet states. When the potential energy contained in one of these strings is large enough the system may produce a quark-antiquark or a diquark-antidiquark pair. This breaking-up of strings continues until only on-shell hadrons remain where a hadron consists of a small string with a quark or diquark on one side and an antiquark or antidiquark on the other side. A large fraction of the hadrons will be unstable and decay to particles that are eventually "detected" in the experiment.

3.4 Monte Carlo samples

This section gives a short overview of the various charged current and neutral current DIS Monte Carlo samples that are used in the analysis. Also the Monte Carlo samples for background studies are listed.

3.4.1 Charged current DIS

Various samples of charged current DIS Monte Carlo have been generated with the programmes described above. In order to be independent of Monte Carlo statistics a good coverage of the entire phase space is necessary even at very high Q^2 and x where the data are statistically limited. This is achieved by applying several cuts on Q^2 and x at the generator level. Afterwards the various samples need to be combined with an appropriate reweighting procedure. In table 3.1 the cross section and the number of events in each sample are listed.

The default set of Monte Carlo data, i.e. the set that will be used in the comparisons with real data, is generated with the ARIADNE colour dipole model to simulate the QCD showering. An alternative set with equal equivalent luminosity has been generated with the matrix element parton shower (MEPS) model of LEPTO. This set will be used to investigate the systematic effects on the measured cross section due to the uncertainties in the modelling of the initial and final state shower development.

Q^2_{gen} cut (GeV^2)	x_{gen} cut	σ (pb)	N_{gen} (kEvts)
10	–	40.5	205
10	0.1	9.02	75
10	0.3	1.10	50
10	0.5	0.115	20
5000	–	2.51	75
10000	–	0.477	55
20000	–	0.0324	40

Table 3.1: *cross sections σ and number of events N_{gen} of the ARIADNE charged current DIS Monte Carlo samples for each cut Q^2_{gen} and x_{gen}.*

In the reweighting procedure of the various samples the kinematics must be computed from the four-momenta of the incoming and outgoing lepton since this is the way the generator calculates the cuts on Q^2_{gen} and x_{gen}. However, in general these kinematics are different from the true kinematics due to electroweak radiative effects. The true kinematics which are used in e.g. acceptance corrections are calculated from the hadronic side of the generated event.

The shape of the input vertex distribution that goes into the simulations is determined from a high-statistics low Q^2 neutral current DIS data sample [51]. In constructing this sample the strong dependence of the trigger efficiency on the z-position of the vertex is removed by requiring that the positron is detected far enough from the rear beampipe and that the vertex is well measured by the hadronic side of the event. In this way an event sample is obtained of which the observed vertex distribution reflects the underlying true vertex distribution.

3.4.2 Photoproduction

Photoproduction of high transverse energy jets is one of the most important background processes contaminating the final charged current sample. When one of the jets loses energy in inactive material in front of the calorimeter or when it enters an uninstrumented region of the detector the measured event will have a missing transverse momentum that might be large enough to lead to selection as a charged current event (see also the next chapter).

In lowest order QCD, photoproduction processes can be separated into two classes, direct and resolved photoproduction, as illustrated in figure 3.2. In direct photoproduction the whole photon interacts with a parton (gluon) inside the proton and two jets are produced, apart from the proton remnant. In the resolved process the photon acts as a source of partons and one of these partons has an interaction with the parton originating from the proton. The unscattered constituents of the photon recombine into a remnant similar to the proton remnant and is usually found in the backward part of the detector. The exchanged photon has a very low invariant mass Q^2, typically smaller than 1 GeV^2, such that the scattered positron escapes

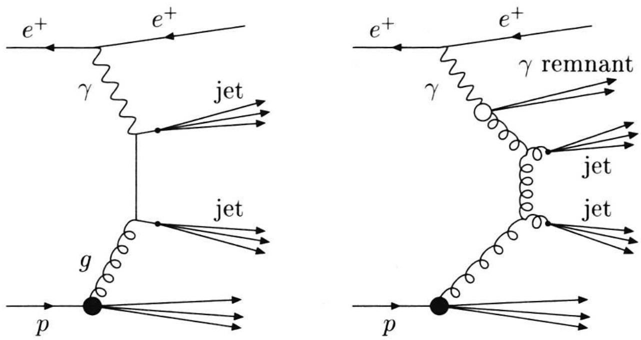

Figure 3.2: *diagrams showing a direct (left) and a resolved (right) photoproduction event. In the latter case the photon acts as a source of partons.*

through the rear beampipe. The cross sections for these processes are large, of the order of tens to hundreds of nanobarns, which means that it is almost impossible to generate a sample with an equivalent luminosity that is a few times the luminosity of the data.

Photoproduction Monte Carlo samples have been generated with the HERWIG 5.9 package [52]. The number of events and the equivalent luminosity of the samples are given in table 3.2. To avoid wasting storage space with events that do not have any chance to be mistaken for a charged current event the samples are reduced by requiring that E_T of the generated hadronic final state exceeds 20 GeV or that P_T is larger than 6 GeV.

3.4.3 Lepton pair production

The most important Feynman diagram for lepton pair production in ep scattering is drawn in figure 3.3 where a photon from the initial positron and one from the proton interact creating a lepton pair l^+l^-. The reaction can be either elastic or inelastic.

Muon pair production forms a background to the charged current sample because the muons, acting as minimum ionising particles, will only lose a fraction of their energy in the calorimeter which might result in a missing transverse momentum. The final charged current sample might also contain some contamination coming from tau pair production where the tau particles decay hadronically. Therefore, four different samples of (in)elastic muon and tau pair production events have been generated with the LPAIR package [53]. The cross sections, the generated numbers of events and the equivalent luminosities of the samples can be found in table 3.2.

3.4.4 W production

Samples of W production ($e^+ p \to e^+ W^\pm X$) events have been generated with the EPVEC [54] generator package. This process can form a background, for example, when the W particle decays to a lepton-neutrino pair. The cross section is dominated by the diagram shown in figure 3.4 where an almost real photon and a u-channel quark are exchanged. Close to the

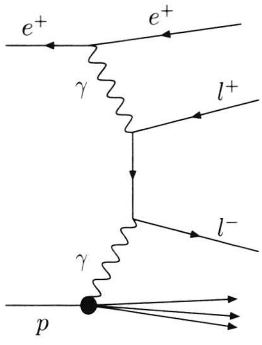

Figure 3.3: *diagram showing the production of a lepton pair l^+l^- via a two-photon interaction.*

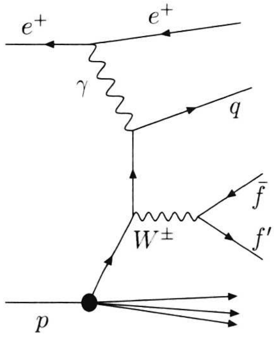

Figure 3.4: *dominant diagram in W production $e^+ p \rightarrow e^+ W^\pm X$. The $W^\pm$ can decay to a quark-antiquark pair or a lepton-antilepton pair.*

u-channel pole the QCD corrections become large and W production can be thought of as quark-antiquark annihilation where one of the quarks is considered as a constituent of the "resolved" photon. EPVEC carefully mixes this resolved photon region with the DIS photon region, far away from the pole. Table 3.2 lists the produced samples of resolved and direct $W^\pm$ production.

3.4.5 Neutral current DIS

Neutral current DIS Monte Carlo and data event samples are used to cross-check the predictions from the charged current Monte Carlo samples. Removing the scattered positron and the accompanying track in a neutral current event — a procedure that will be referred to as CCfying — yields an event topology very similar to that of a genuine charged current event. By properly reweighting the CCfied neutral current events to the charged current cross section a sample of

process	σ (pb)	N_{gen} (kEvts)	$\mathcal{L}_{equivalent}$ (pb^{-1})
direct photoproduction	51.02×10^3	2400	121
resolved photoproduction	73.96×10^3	3280	44
$\mu\mu$ elastic	36.79	20	546
$\mu\mu$ inelastic	70.75	40	567
$\tau\tau$ elastic	105.79	60	567
$\tau\tau$ inelastic	71.38	60	842
W^- resolved	0.100	10	98.9×10^3
W^+ resolved	0.126	10	78.3×10^3
W^- DIS	0.324	20	61.2×10^3
W^+ DIS	0.392	10	24.6×10^3

Table 3.2: *samples used for background studies showing the cross section σ, the number of generated events N_{gen} and the equivalent luminosity $\mathcal{L}_{equivalent}$ for each background process.*

fake charged current events is obtained.

The neutral current data used in the CCfying process are taken to be the set of data selected in [55] which corresponds to the same integrated luminosity of e^+p data as used in this analysis. Samples of neutral current Monte Carlo are generated with DJANGO 6.24 and ARIADNE 4.0.8 where the proton is described by the CTEQ4D set of parton density functions. A total of 13 pb^{-1} of equivalent luminosity is used with a minimum generated Q^2 of 100 GeV^2.

Some quality criteria are imposed on the neutral current events. The energy of the scattered positron has to exceed 10 GeV, while the accompanying track is required to have a distance of closest approach to the positron of less than 10 cm. Furthermore the quantity δ, defined in equation 4.7, should be in the range between 38 GeV and 65 GeV. The "true" kinematics of the neutral current data and Monte Carlo events are calculated with the double angle method as described in chapter 6. With these kinematics comparisons can be made between CCfied Monte Carlo and data. However, sometimes it is necessary to compare charged current Monte Carlo and CCfied neutral current Monte Carlo. In that case the true kinematics are calculated from the generated hadronic side of the event as mentioned before in section 3.4.1. Although the double angle method has a systematic bias in the reconstruction of the kinematics at low values of y compared to the generated kinematics it can safely be used for comparisons between data and Monte Carlo since only the relative differences between the two sets are important.

Chapter 4

Selection of CC DIS events

A characteristic experimental property of charged current DIS events is missing transverse momentum P_T in the calorimeter which is defined as

$$P_T^2 = P_x^2 + P_y^2 = \left(\sum_i E_i \sin\theta_i \cos\phi_i \right)^2 + \left(\sum_i E_i \sin\theta_i \sin\phi_i \right)^2 \tag{4.1}$$

where the sum runs over all calorimeter energy deposits E_i, and θ_i and ϕ_i are their polar and azimuthal angle as seen from the interaction vertex. Therefore, the online trigger chain is designed as to detect events with this characteristic. However, a considerable amount of background is also selected by the rather loose criteria used in the trigger such that more refined cuts are necessary further down the selection chain. First of all halo muons and cosmic rays form a substantial background. Also genuine ep processes such as neutral current DIS and photoproduction can have a missing transverse momentum due to an incomplete measurement of the scattered positron or the hadronic final state. Finally, special cuts are necessary to get rid of events caused by malfunctioning of the detector. In this chapter all the selection criteria that are necessary to obtain a pure charged current DIS sample are described.

4.1 Trigger and pre-selection

Events are filtered online by a three level triggering system which has been described in section 2.10. In the charged current trigger selection chain the main components are the calorimeter and the CTD. During the years 1994 to 1997 the trigger chain was modified several times. These modifications mainly concerned the requirement on the minimum transverse momentum recorded in the calorimeter which was gradually lowered in the course of the years. Also new cuts were introduced, however, and other cuts discarded. This results in a rather complicated history of the trigger and many pages would be necessary to give a detailed account of all different trigger configurations. Here only a global overview of the essential steps in the trigger chain will be given.

At the first trigger level events are selected as an OR of various trigger conditions that require a sizeable amount of energy in the calorimeter, optionally accompanied by a track in the CTD. Other conditions require a minimum total transverse energy E_T (larger than 30 GeV in 1996 and 1997) or a minimum missing transverse momentum, above 5 GeV. Usually when a track is found in the event the requirements on energy and momentum related quantities are less stringent.

At the second trigger level the calorimeter information is available with higher accuracy. Therefore, the requirements on the missing transverse momentum can be raised to about 7 GeV (9 GeV in 1994). Again, if a good track is found these threshold values are lower. Background originating from cosmic rays and beam-gas events upstream of the detector are removed by requiring a timing measurement for the event compatible with an *ep* collision in the interaction region.

At the third trigger level the full event information is available with full resolution. The missing transverse momentum can now be calculated with the highest accuracy. Basically the same threshold values are used as at the second trigger level. The background due to beam-gas events is further reduced by using tracking information.

Events that pass all three trigger levels are written to Data Summary Tape (DST). A "fourth" level trigger selection is done by combining the results of those branches at the third trigger level that accept events with missing transverse momentum. The minimum cut on P_T at this level equals 9 GeV in 1994 and was lowered to 8 GeV in 1995 and to 7 GeV in 1996 and 1997. Furthermore, triggers due to a sparking photomultiplier are removed. A total number of about 1.5 million events are accepted by this DST filter in the 1994–1997 running period.

4.2 Vertex determination

The CTD is used to reconstruct the longitudinal coordinate of the primary vertex of the event, z_{vertex}. Since the other tracking detectors VXD, FDET and RTD are not available for all the years of data taking they are left out from the vertex and track reconstruction (see also section 2.5). The transverse coordinates of the vertex are set to zero as the beam width is about 10 times smaller than the transverse resolution of the CTD. In principle the transverse vertex for events in a specific run could be set at the mean transverse vertex position averaged over a whole run. This mean position, however, is at most of the order of a millimeter and introduces only a negligible effect in the reconstruction of the kinematics of charged current events.

The efficiency with which vertices are found by the CTD depends on the hadronic angle of the event. This is shown in figure 4.1a where this efficiency is plotted versus γ_0, the hadronic angle as defined in section 6.1 with the vertex fixed at the nominal interaction point $(0, 0, 0)$. Below $\gamma_0 \sim 0.4$ ($\sim 23^o$) the efficiency drops and becomes essentially zero at very forward angles. This is the region where the hadronic particles cross only one or two superlayers. The quality of the reconstructed tracks is then rather poor and the measured vertex becomes unreliable. Sometimes there will not even be a vertex as there are no reconstructed tracks at all. So it is clear that in this region another way of vertex reconstruction is needed. The method that is adopted here is to employ the timing information of the forward calorimeter to measure the vertex [56].

Since the proton bunches have a length of about 20 cm while the size of the positron bunches is negligible in comparison the *ep* interaction can happen at any point inside the proton bunch. This results in a spread of the interaction vertex around the nominal vertex position z_{int}, which

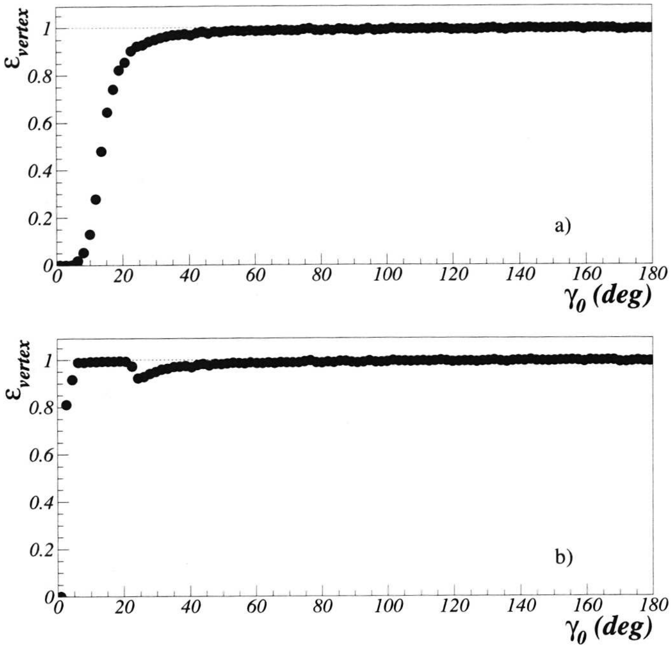

Figure 4.1: *(a) efficiency ϵ_{vertex} of measuring a vertex with the CTD as a function of the hadronic angle γ_0, (b) idem when both the CTD vertex ($\gamma_0 > 0.4$) and the FCAL timing vertex ($\gamma_0 < 0.4$) are used.*

is the point where the positrons cross the middle of the proton bunch. Note that this position is in general different from the nominal interaction point that defines the centre of the ZEUS detector. If the position of the interaction, i.e. z_{vertex}, is known then the time t_{vertex} at which the interaction happens is given by

$$t_{vertex} = \frac{1}{c}(z_{int} - z_{vertex}) + t_{int} \tag{4.2}$$

where c is the speed of light and t_{int} is the time at which the positrons cross the middle of the proton bunch. Both z_{int} and t_{int} are determined from the information provided by the C5 detector.

Now it is assumed that particles coming from the interaction vertex z_{vertex} travel at the speed of light towards the forward calorimeter. The time t_c at which a particle arrives at an FCAL cell at position (x_c, y_c, z_c) is then

$$t_c = t_{vertex} + \frac{1}{c}\, d((0,0,z_{vertex}),(x_c,y_c,z_c)) - \frac{1}{c}\, d((0,0,0),(x_c,y_c,z_c)) \tag{4.3}$$

where $d(\vec{A},\vec{B})$ is the distance between the two points $\vec{A}$ and $\vec{B}$. The last part of this equation takes into account the online correction for the time-of-flight from the nominal interaction point to the FCAL cell. From this equation it is clear that there is a direct relation between the time recorded in an FCAL cell and the vertex of the interaction. The latter is then determined as

$$z_{vertex} = \frac{\sum_i \frac{1}{\sigma_i^2} z_{vertex,i}}{\sum_i \frac{1}{\sigma_i^2}} \tag{4.4}$$

Here the sum runs over all FCAL cells with energy exceeding 0.5 GeV for EMC cells or 1 GeV for HAC cells, so-called "good" cells. For each individual cell the event vertex $z_{vertex,i}$ can be computed, using relation 4.3, from the timing information given by the two photomultipliers. The weight σ_i is the timing resolution for the cell calculated with formula 2.3.

The vertex $z_{vertex,i}$ is corrected for several effects. One of these effects is a run to run shift between the time of a cell expected from the position of the CTD vertex with respect to the actual measured time. Other effects include dependences on the energy recorded in a cell and on how much energy the cell has in comparison with its neighbouring cells. The corrections have been obtained from a neutral current sample consisting of data collected during the years 1994 to 1997 in which the timing vertex has been optimised to match the CTD vertex of the event.

For real data this vertex reconstruction method works quite well. In Monte Carlo data, however, the timing is not very well simulated so the timing vertex cannot be used in the same way as described before. This problem is solved as follows. In the data the vertex resolution is measured as a function of the number of good FCAL cells. This resolution is around 20 cm if there are less than 10 good cells and improves to 8 cm for more than 20 good cells. The true vertex in the Monte Carlo simulation is then smeared according to a Gaussian distribution that has a width equal to this resolution.

In figure 4.2 the bias of the timing vertex z_{timing} with respect to the CTD vertex z_{CTD} is shown for CCfied neutral current data and Monte Carlo and for the final charged current data sample. This bias is obtained via a Gaussian fit to the distribution of $z_{timing} - z_{CTD}$ in several bins in z_{CTD}. The upper plot shows the bias in the high γ_0 region above 0.4 as a function of the CTD vertex of the CCfied or the genuine charged current event. A bias of at most 2 cm is observed and this is only at the most forward and backward vertices where statistics are limited. The error bars indicate the resolution of the timing vertex, which is around 8 cm. In the lower plot the bias for events having $\gamma_0 < 0.4$ is plotted as a function of the CTD vertex of the entire neutral current event, i.e. including the track pointing to the DIS positron. Of course, for charged current events no such CTD vertex exists. Also in this region no substantial bias is observed. Thus using the timing vertex at low γ_0 is legitimate if it is assumed that CCfied neutral current data and real charged current data have a very similar hadronic final state.

In the remainder of the selection procedure and in the kinematic reconstruction the timing vertex will be used in the region $\gamma_0 < 0.4$ whereas above 0.4 the CTD vertex is taken. The efficiency with which this vertex can be measured is plotted in figure 4.1b as a function of γ_0. In figure 4.3 the measured vertex distribution is compared to the ARIADNE Monte Carlo prediction. In this plot all selection cuts that are described in this chapter are applied except for the vertex cuts. The measured distribution is well reproduced by Monte Carlo although there is some overshoot in the data for $z_{vertex} > 75$ cm which is possibly due to very forward

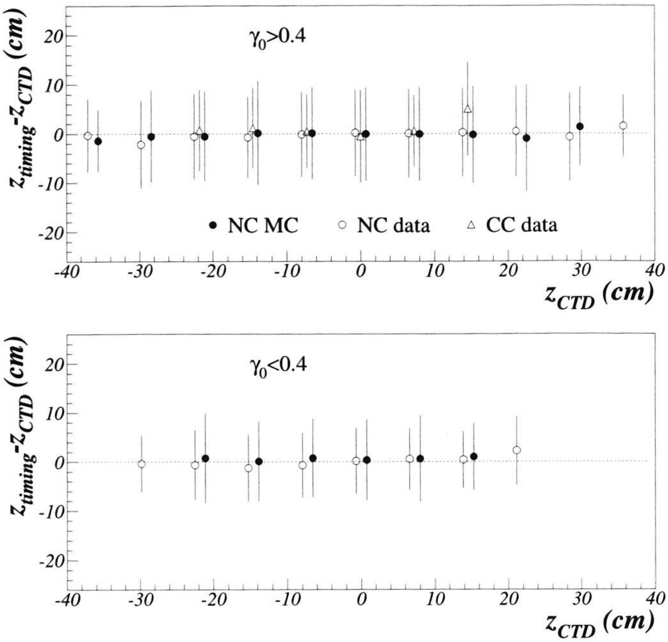

Figure 4.2: *bias of the timing vertex z_{timing} with respect to the CTD vertex z_{CTD} for CCfied neutral current data (circles) and Monte Carlo (dots) and charged current data (triangles). The upper plot shows the bias for $\gamma_0 > 0.4$ as a function of the CTD vertex position of the CCfied or genuine charged current event while the lower plot shows the bias for $\gamma_0 < 0.4$ as a function of the vertex position of the entire neutral current DIS event.*

beam-gas interactions, outside the acceptance region of the CTD. These events do not have a proper tracking vertex but they do have a timing vertex since the number of good FCAL cells is large for this type of events.

The events in the final charged current sample are required to have a vertex between -50 cm and 50 cm. This corresponds to the region between the two vertical lines in figure 4.3. The vertex cut throws away a large fraction of the cosmic and halo muon background, typically events where a muon only hits the calorimeter without entering the inner detector. The satellite peaks originating from collisions with protons in neighbouring RF buckets are also rejected by this cut. Although events in this peak can be good physics events they have a trigger efficiency that is different from the efficiency for events coming from the main peak region.

4.3 Tracking

In many cosmic and halo muon events the muon traverses the ZEUS detector without entering the CTD. Nevertheless, the track reconstruction package might still find one or more low

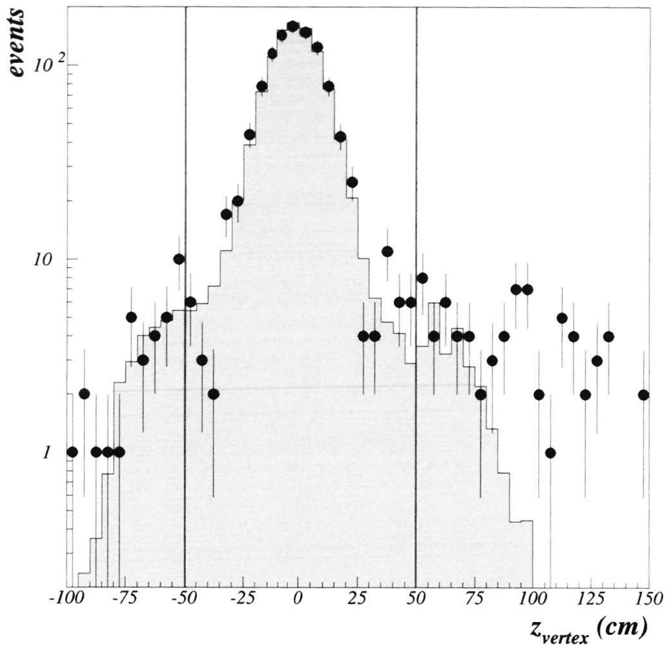

Figure 4.3: *the z_{vertex} distribution for events that pass all selection cuts. The Monte Carlo prediction is given by the shaded histogram while the data are represented by the dots. The region in between the two vertical lines is accepted by the vertex cuts.*

momentum tracks that are due to particles originating from a bremsstrahlung shower caused by the muon. Sometimes noise in the CTD will also lead to a reconstructed track. As a track close to the beamline (the line $(x, y) = (0, 0)$) always yields a reconstructed vertex the vertex cuts are not very effective in this case. By requiring at least one "good" track in the event the halo and cosmic muon background can be further reduced. A good track is defined as a track fulfilling the following criteria

- the distance to the beamline is less than 1.5 cm.
- the transverse momentum of the track is larger than 0.2 GeV.
- the track has a polar angle between 15^o and 165^o. This range corresponds to the region of the CTD where at least two superlayers are hit.
- the track reconstruction package can fit the track to the vertex. This implies that tracks far away from the vertex are not classified as good tracks.

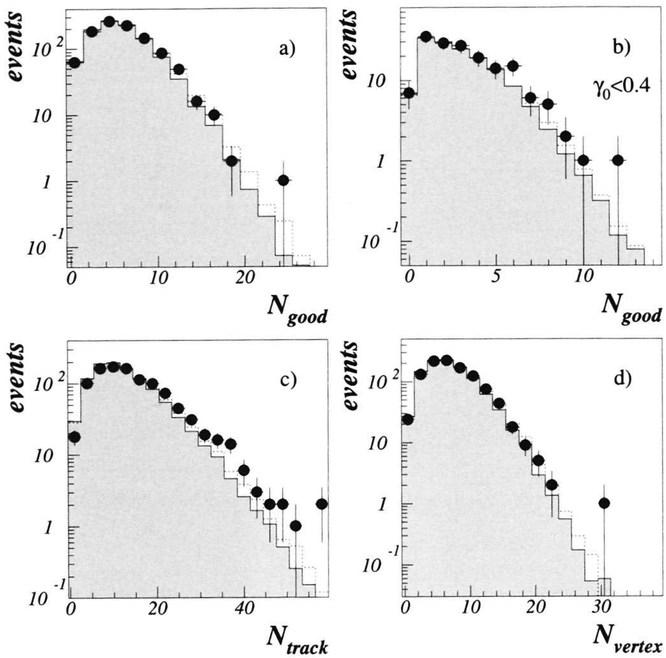

Figure 4.4: *several tracking distributions for events that pass all selection criteria, (a) number of good tracks, (b) number of good tracks for events with $\gamma_0 < 0.4$, (c) number of tracks, (d) number of vertex fitted tracks. The dots represent the final sample of charged current data, while the shaded histogram denotes the ARIADNE prediction and the dotted line the prediction of MEPS.*

This definition is only used in the region where γ_0 exceeds 0.4. Below 0.4 the quality of the tracks is in general worse but still the Monte Carlo simulation is able to describe these tracks[1]. Therefore, in this region the requirement on the minimum polar angle is lowered from 15^o to 10^o and the transverse momentum of the track has to be larger than 0.1 GeV. The requirement that the track is fitted to the vertex is replaced by $|z_{beamline} - z_{timing}| < 50$ cm where z_{timing} is the timing vertex and $z_{beamline}$ is the z-position of the track in the point of closest approach to the beamline. If no good track is found in an event with $\gamma_0 < 0.4$ but the transverse momentum of the event exceeds 50 GeV the event is also accepted.

In figure 4.4a the number of good tracks, N_{good}, is displayed for the final charged current sample. The shaded histogram is the ARIADNE Monte Carlo expectation, the dotted histogram is the prediction of MEPS and the dots represent the data. Figure 4.4b shows the number of good tracks for events in the region with low hadronic angle $\gamma_0 < 0.4$. The total number

[1]A good track in the region $\gamma_0 < 0.4$ does not necessarily mean that the CTD vertex can be measured accurately. As the track and the beamline are almost parallel a small change in the polar angle of the track yields a large variation in the CTD vertex position. Thus it is still better to use the timing vertex.

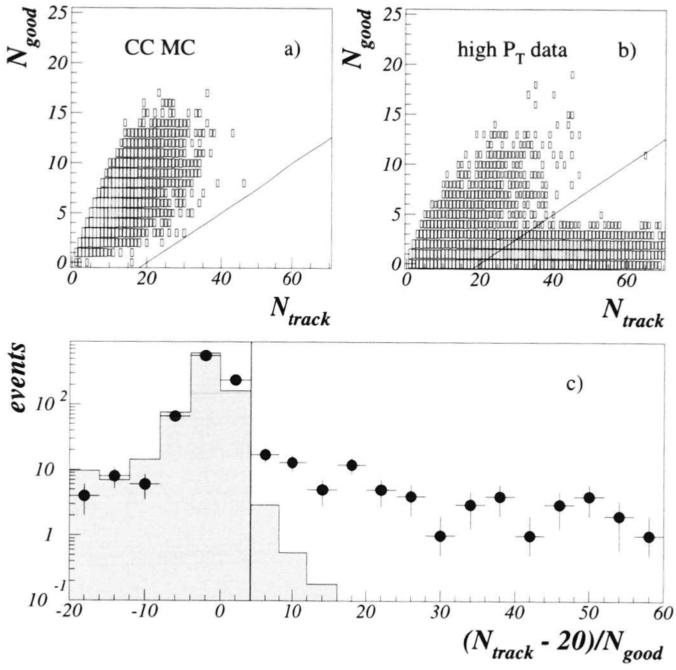

Figure 4.5: *the number of good tracks versus the total number of tracks for (a) charged current Monte Carlo and (b) a sample of high missing transverse momentum data that passes the trigger and pre-selection cuts. The area of the boxes is proportional to the number of events. All events below the solid line are rejected by the cut* $N_{good} \geq \frac{1}{4}(N_{track} - 20)$. *(c) Distribution of* $(N_{track} - 20)/N_{good}$ *for data (dots) and ARIADNE Monte Carlo (filled histogram) after all cuts have been applied except for the cut on* N_{good} *versus* N_{track}. *All events to the right of the vertical line are rejected by the cut.*

of tracks, N_{track}, is given in figure 4.4c where a slight discrepancy is observed between data and Monte Carlo as the track multiplicity in data is higher than expected. The number of tracks in data that can be fitted to the vertex, N_{vertex}, by the track reconstruction package (not necessarily good tracks) does nevertheless agree with the expectations as is shown in figure 4.4d. The two different Monte Carlo sets give very similar results in all distributions.

For beam-gas and beam-wall interactions the number of reconstructed tracks is in general very large compared to genuine charged current events. On the other hand, the fraction of good tracks is small since the number of tracks associated with the primary vertex is usually small. In figures 4.5a and 4.5b the number of good tracks in an event is shown versus the total number of tracks for Monte Carlo data and for a data sample that passes the trigger and pre-selection cuts, respectively. In real data a large number of events is observed that have many tracks but only a few good tracks whereas in Monte Carlo data no or very few such events are seen. Based on these plots a cut is applied, only in the region $\gamma_0 > 0.4$, that removes a large fraction of these data events:

$$N_{good} \geq \frac{1}{4}(N_{track} - 20) \tag{4.5}$$

In the plots the equality is shown as a solid line. Events that are below this line are rejected. Figure 4.5c shows the distribution of $(N_{track} - 20)/N_{good}$ in the charged current sample (dots) and the expectation of the ARIADNE Monte Carlo simulation (filled histogram). All selection cuts have been applied in this plot except for cut 4.5. Events to the right of the vertical line are rejected by this cut.

4.4 Calorimeter cuts

A malfunctioning of the calorimeter can easily lead to an effective missing transverse momentum that will fire the charged current trigger. On one hand this can be caused by energy loss, e.g. due to a broken module, such that the final state of *ep* events is only partially measured. This type of events is removed by deselecting the (few) runs that have a broken calorimeter. On the other hand, a spark in a single cell or a faulty read-out card might add some extra energy to an event. Often cells that record such fake energy will also have a large imbalance. Therefore, these events can easily be removed by requiring that not all missing transverse momentum P_T originates from cells with a high imbalance. Events are accepted if they satisfy

$$0.5 < \frac{P_T^{imb<0.8}}{P_T} < 2 \tag{4.6}$$

where $P_T^{imb<0.8}$ denotes the missing transverse momentum of the event that is calculated by only using cells with imbalance $|imb/E_{cell}| < 0.8$ (see also section 2.4.1).

Another type of background is formed by events where a single cell is responsible for the bulk of the missing transverse momentum. This can be a non-isolated spark (isolated sparks are removed in the trigger chain), a spark in a cell where one of the PMTs is broken or a cosmic muon that deposits a considerable amount of energy in only one cell. Events are rejected if they fulfil at least one of the following criteria

- $imb_{max} = 0$ and $P_T(-cell)/P_T < 0.15$
- $imb_{max} = 0$ and $P_T(-cell)/P_T < 0.25$ and $P_{T,max}/E_{max} > 0.5$.
- $|imb_{max}/E_{max}| \geq 0.6$ and $P_T(-cell)/P_T < 0.25$.

Here imb_{max}, E_{max} and $P_{T,max}$ are the imbalance, the energy and the transverse momentum of the cell that has maximum transverse momentum. $P_T(-cell)$ is the transverse momentum that remains in the event if this cell is removed. The first two cuts are meant to remove events where a spark occurred in a cell with one broken photomultiplier leading to an imbalance exactly equal to zero. If this spark is roughly in the barrel or rear calorimeter then the cut on $P_T(-cell)/P_T$ is increased to 0.25. The last cut rejects events with sparks occurring in a good but non-isolated cell.

4.5 Neutral current background

Low Q^2 neutral current events can have a large missing transverse momentum if the final state positron is not fully contained in the calorimeter or if the proton remnant and current jet are both very forward and a large fraction of the jet is lost in the forward beampipe or in inactive material. Hence such events might contaminate the charged current event sample. This background can be removed very efficiently by finding the DIS positron and identifying the event as a neutral current DIS event. Four different branches labelled as A, B, C and D are used for this purpose. If one of these branches classifies the event as a neutral current DIS event then it is rejected from the final charged current event sample.

To identify the final state positron a neural network algorithm called SINISTRA [57] is used. This algorithm has been tuned on Monte Carlo events and assigns a probability $\mathcal{P}_{sinis}$ to each energy cluster in the calorimeter. A large value of $\mathcal{P}_{sinis}$ means that the respective cluster has a large probability to be a positron. The final state DIS positron is defined as the cluster that has highest probability above some minimum probability cut $\mathcal{P}_{cut}$ which is set to 0.9. To ensure a sufficient purity a minimum positron energy of 4 GeV is required. In addition the positron has to be isolated, i.e. there is not more than 5 GeV of energy not assigned to the positron in a cone of radius 0.8 in (η, ϕ) around the positron.

In some of the four branches a track matching with the positron is required. Of course, this is only done when the positron is within the acceptance region of the CTD. A matching track is defined as a track extrapolated to the surface of the calorimeter that has a distance of closest approach (DCA) to the positron less than 15 cm. Furthermore, the momentum of the track has to exceed 1 GeV and it should be at least 5% of the positron's energy. Moreover, the matching track has to be the only one, which means that there is no other track carrying a momentum of more than 5% of the positron's energy within a distance of 1 unit in (η, ϕ) space to the matching track.

Branch A takes care of positrons that enter the rear calorimeter. No matching track is required in this branch since the acceptance of the CTD is very small in the region close to the rear beampipe. The cone radius in the isolation criterion of the positron is lowered from 0.8 to 0.6. If a positron is found in the RCAL and $\delta > 40$ GeV then the event is identified as a neutral current DIS event and rejected. Here δ is defined as

$$\delta = \sum_i E_i - P_{z,i} = \sum_i E_i(1 - \cos\theta_i) \tag{4.7}$$

where the sum runs over all calorimeter cells in the event. For a neutral current event that is fully contained in the calorimeter δ should be close to $2E_e = 55$ GeV, which is the total $E - P_z$ of the initial state.

For positrons that are in the acceptance region of the CTD branch B requires a track matching with the positron if the positron has a polar angle between 15° and 165°. The region where the polar angle is less than 15° is covered by branch C. Here no matching track is required but instead the positron has to have at least 20 GeV of transverse energy. In both branches δ should be larger than 25 GeV.

Finally, branch D handles some special cases where δ is very low or where there is hardly

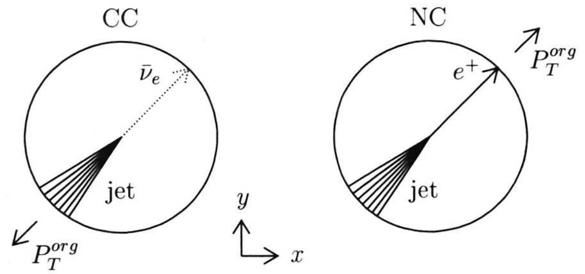

Figure 4.6: *illustration of the definition of ϕ_T. In the charged current event in the left plot a positron may be found in the jet leading to a small ϕ_T as the direction of P_T calculated with the positron removed is not very different from that of the transverse momentum P_T^{org} of the entire event. In the right plot, however, the direction of $P_T(-e)$ can be very different from that of P_T^{org} and thus ϕ_T will be large.*

any hadronic activity in the calorimeter. This branch uses a transverse angle ϕ_T defined as

$$\cos\phi_T = \frac{\vec{P}_T \cdot \vec{P}_T(-e)}{|\vec{P}_T||\vec{P}_T(-e)|} \tag{4.8}$$

where $\vec{P}_T$ is the transverse momentum of the entire event and $\vec{P}_T(-e)$ is the transverse momentum that remains when the positron is removed from the event. Figure 4.6 illustrates the definition of ϕ_T. The left plot shows a schematic view in azimuth of a one-jet charged current event. The evanescent neutrino is drawn as a dotted arrow opposing the jet in azimuth. If a positron is found in the jet then the direction of P_T will not change drastically compared to the transverse momentum of the entire event, P_T^{org}, when the positron is removed from the event. Hence in this case ϕ_T will be small. On the other hand, for a neutral current event as shown in the plot on the right the positron that is found is the scattered DIS positron which is opposite to the hadronic side of the event. If this positron is removed the direction of P_T can be very different from the direction of P_T^{org}. Branch D now identifies an event as a neutral current event if there is a positron with polar angle larger than 15^o and a matching track. In addition it is required that either $\phi_T > 60^o$ or that the ratio of the total electromagnetic energy to the total energy in the calorimeter is larger than 0.95.

Figure 4.7 shows distributions of a few variables that are used in the neutral current DIS rejection. The first two plots show the distribution of the energy of the positron $E_{positron}$ and of δ for the charged current sample where all cuts have been applied except those intended to reject neutral current background. As expected the neutral current background is observed at positron energies around the beam energy and at large δ which means that the bulk of the background is found in the rear calorimeter. In figure 4.7c and 4.7d the same distributions are displayed for the final charged current sample with neutral current background removed. Figures 4.7e–g show the distribution of the momentum of the matching track, the distance of closest approach of this track to the positron and ϕ_T for events in the final charged current sample in which a positron is found.

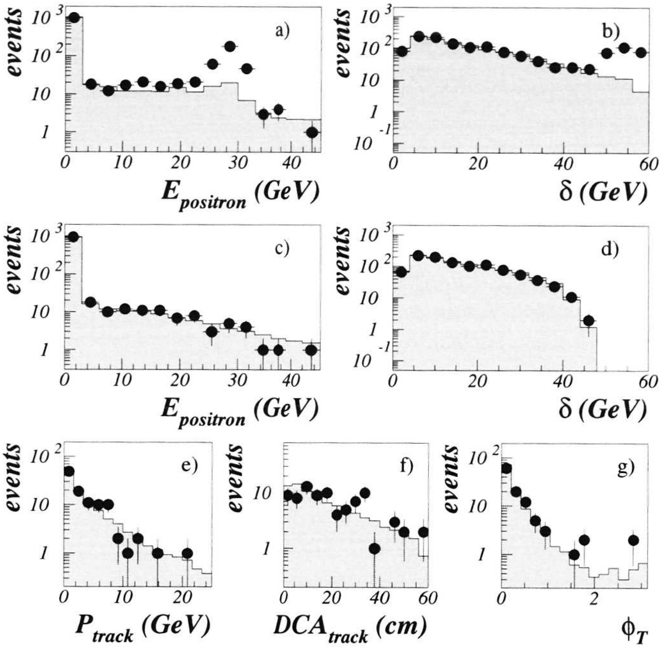

Figure 4.7: *comparison of various distributions of variables used in the neutral current DIS rejection. The dots represent the data and the shaded histogram shows the ARIADNE Monte Carlo prediction. (a) Positron energy and (b) δ for the final charged current data sample with all cuts applied except the neutral current DIS cuts. (c,d) The same plots but now with all cuts applied. The last three plots show distributions for events from the final sample in which a positron is found: (e) momentum P_{track} of the matching track, (f) distance of closest approach of the matching track to the positron, (g) transverse angle ϕ_T.*

4.6 Events with a high-momentum track

A small background is formed by events that have a high-momentum track in the CTD and some energy deposit in the calorimeter that is responsible for the missing transverse momentum that fires the charged current trigger. Such events can, for example, be events that contain a muon originating from the vertex that escapes from the detector leaving only very little energy in the calorimeter. Or it can be a neutral current event with a positron that is not recognised as such by SINISTRA. An example of an event with a high-momentum track is displayed in figure 4.8. In this particular event a muon is produced at the vertex and it leaves the detector through the rear part of the barrel calorimeter and the uninstrumented gap between the barrel and rear calorimeter.

This background can be removed by requiring that the high-momentum track is isolated and that the missing transverse momentum vanishes if the track momentum is added to the

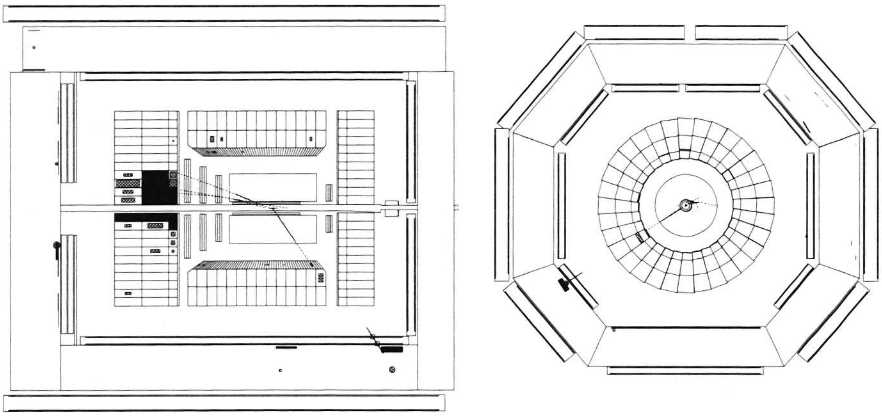

Figure 4.8: *example of an event that has high missing transverse momentum because of a muon. In this particular event the muon is produced at the vertex and leaves the detector via the rear part of the barrel calorimeter and the gap between RCAL and BCAL.*

transverse momentum of the calorimeter. A track is called isolated if there is no other track within a cone of radius 0.8 in (η, ϕ) space around the high-momentum track. Furthermore, the momentum of the track has to exceed 10 GeV and its polar angle should be larger than 50°. The latter requirement ensures that the track is not pointing to the proton remnant or a forward jet. If an event fulfils these criteria it is rejected from the final sample if $P_T^{new}/P_T < 0.6$ where P_T^{new} is the missing transverse momentum of the event when the track is taken into account. This quantity is computed as

$$(P_T^{new})^2 = (P_{x,cal} + P_{x,track})^2 + (P_{y,cal} + P_{y,track})^2 \tag{4.9}$$

where $P_{x,cal}$ and $P_{y,cal}$ are the sums of the calorimeter energy deposits projected onto the x and y axis, respectively, as defined in equation 4.1, while $P_{x,track}$ and $P_{y,track}$ are the projections of the track momentum.

4.7 Photoproduction background rejection

Another important source of background originates from photoproduction events with high transverse energy jets. In fact this is the most serious background as the event shapes are indistinguishable from genuine charged current events, especially in the region at low P_T where the jets are very forward and close together. Nevertheless, a considerable fraction of the photoproduction background can still be removed by cutting on the event shape. The cuts that are applied require that there is an azimuthally collimated energy flow as is expected for the current jet in a charged current event. This cut, however, might be dangerous for events with two or more jets. Therefore, in the region where these multi-jet events are expected, the region

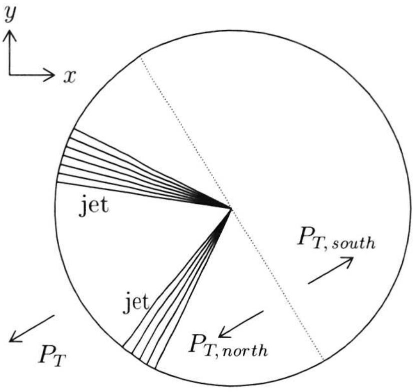

Figure 4.9: *schematic cross section of a two jet charged current event in the transverse plane. The dotted line is the plane along the z-axis perpendicular to the vector P_T. The transverse momentum calculated from all calorimeter cells to the left of this plane is called $P_{T,\,north}$, whereas the remaining cells yield a transverse momentum $P_{T,\,south}$.*

where $P_T > 35$ GeV, no cut specifically designed to remove photoproduction is applied. Note that the photoproduction background is located mainly at lower values of P_T.

In the region of intermediate P_T, i.e. 25 GeV $< P_T <$ 35 GeV, the requirement $P_T/E_T > 0.4$ is imposed. For events with $P_T <$ 25 GeV this cut is raised to 0.5 if $\gamma_0 > 0.4$ and to 0.6 if $\gamma_0 < 0.4$. In addition in this lower P_T region an extra cut

$$\frac{P_T(-ir)}{P_{T,\,north}(-ir)} > 0.85 \tag{4.10}$$

is applied where $-ir$ means that the innermost ring around the forward beampipe is removed from the event. The reason for this is that the proton remnant fragmentation close to the beampipe is less well simulated in Monte Carlo. $P_{T,north}$ is defined as the total transverse momentum originating from all calorimeter cells on the "north" side of the plane perpendicular to the P_T vector. This is illustrated in figure 4.9 that shows a schematic cross section of a two jet charged current event in the (x, y) plane. The transverse momentum vector P_T lies in the direction of the jets. The dotted line is the plane perpendicular to this vector, parallel to the z-axis. The transverse momentum calculated from all calorimeter cells that are on the left side of this plane, in the "northern hemisphere", is called $P_{T,\,north}$.

Figure 4.10 shows several distributions that are related to the cuts described above. In these plots the filled histograms show the ARIADNE charged current Monte Carlo expectation, while the white histogram is the extra contribution expected from the HERWIG photoproduction samples. The dots represent the data. The first plot shows the distribution of P_T/E_T for P_T exceeding 25 GeV. All selection cuts are applied in this plot except for those intended to reject photoproduction events. The arrow indicates the value of P_T/E_T where a cut is made. In the second plot P_T/E_T is shown for P_T below 25 GeV, again with no photoproduction cuts.

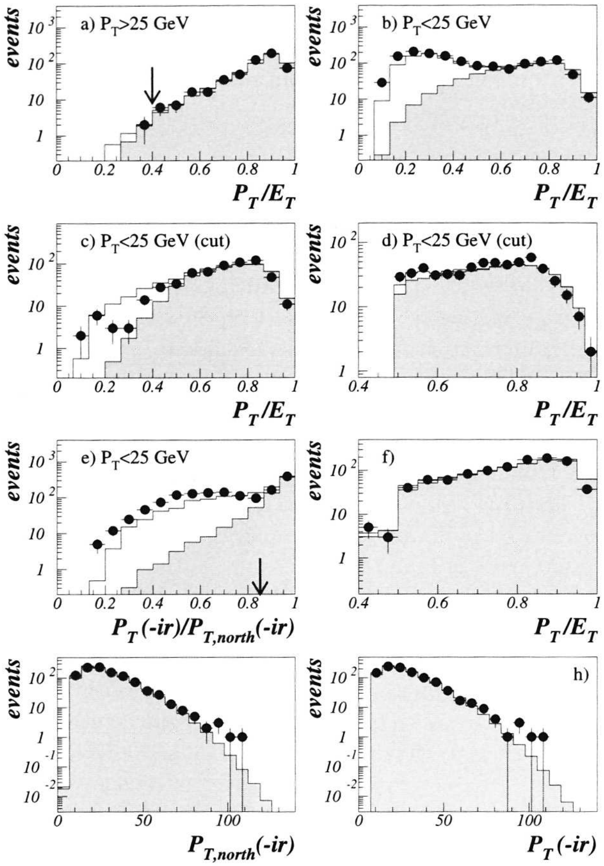

Figure 4.10: *various distributions comparing charged current data (dots) with ARIADNE charged current Monte Carlo data (filled histogram) and photoproduction Monte Carlo (open histogram). The arrows indicate the values in the distribution where a cut is made. (a) P_T/E_T for $P_T > 25$ GeV, (b) P_T/E_T for $P_T < 25$ GeV with no photoproduction cuts applied, (c) P_T/E_T for $P_T < 25$ GeV with the cut on $P_{T,north}$ applied, (d) P_T/E_T for $P_T < 25$ GeV with the cuts on P_T/E_T applied. (e) $P_{T,north}(-ir)$ in the region $P_T < 25$ GeV, with no photoproduction cuts applied. For the final charged current sample (f) shows the distribution of P_T/E_T, (g) that of $P_{T,north}(-ir)$ and (h) that of $P_T(-ir)$.*

A considerable background is present in the data below $P_T/E_T = 0.5$. Figure 4.10c shows the distribution of P_T/E_T, but now the cut on the ratio of $P_T(-ir)$ and $P_{T,north}(-ir)$ has been applied yielding a reduction of the photoproduction background at low values of P_T/E_T. In figure 4.10d the same distribution is shown but now the cut on P_T/E_T has been applied instead of the $P_{T,north}(-ir)$ cut. For values of P_T/E_T between 0.4 and 0.6 there is still some background that will largely be removed by the additional cut on $P_{T,north}(-ir)$. The distribution of $P_T(-ir)/P_{T,north}(-ir)$ is shown in the figure 4.10e, again without any photoproduction cut. The last three figures show the P_T/E_T distribution, the $P_{T,north}(-ir)$ distribution and the $P_T(-ir)$ distribution of the final charged current event sample.

4.8 Cosmic and halo muon background

In the next chapter a detailed description will be given of a special package that has been developed to identify and subsequently remove cosmic and halo muons from the charged current data sample. This package is able to remove most of the background muons that are still in the sample after all cuts described before have been applied.

For events with a low hadronic angle a background is formed by cosmic muons traversing the forward calorimeter that produce a large bremsstrahlung shower. These events typically lose a considerable energy in the hadronic section of the calorimeter. Also events are observed that produce a large electromagnetic shower in the FEMC, mainly due to showering halo muons that are close to the beampipe. Since the muon finder package is less efficient in recognising these muons they are removed by looking at the energy distribution in the event. Events with $\gamma_0 < 0.4$ in which no good track is found are removed if either more than 90% of the energy in the FCAL is recorded in the hadronic sections FHAC1 and FHAC2 or if more than 95% of the energy in the FCAL is recorded in the electromagnetic section. In addition the FCAL energy for these events has to exceed 100 GeV and this energy has to be more than 95% of the total energy recorded in the entire calorimeter.

Not all halo muons that are close to the beampipe will produce a heavy shower in the forward calorimeter. Nevertheless, they still can produce a considerable amount of transverse momentum which is mainly due to energy in the first ring of cells around the forward beampipe. Hence a cut on $P_T(-ir) > 8$ GeV is applied to remove this background. For events in the low gamma region $\gamma_0 < 0.4$ this cut is raised to 12 GeV.

4.9 Kinematic cuts and selection summary

To restrict the sample of charged current events to regions where the resolution in the kinematic variables is sufficiently good and the expected background as predicted from Monte Carlo simulations is small, a minimum Q^2 cut is applied of 200 GeV^2 and maximum y cut of 0.9. In addition $P_T > 11$ GeV is required for events having $\gamma_0 > 0.4$. This threshold is raised to 15 GeV for the timing vertex region $\gamma_0 < 0.4$. In figure 4.11 the selected events in the final sample are plotted in the (x, y) plane. The black dots represent the events that have a vertex reconstructed with the CTD while the open circles are events that have a vertex determined with the FCAL timing. The latter type of events dominates the region $x > 0.3$.

A summary of all cuts that are applied to obtain the final charged current event sample is given in table 4.1. Starting from the total ARIADNE Monte Carlo sample with $Q^2_{true} > 10$ GeV^2 in the upper row each succeeding row gives in the second column the fraction of events that remain in the sample if only the cut in the first column of this particular row is applied. The third column shows the fraction of the events that remain after applying this cut and all the

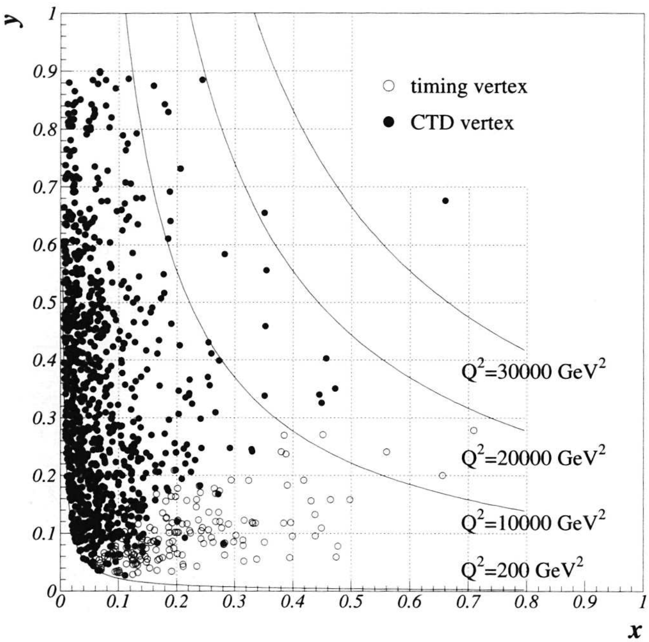

Figure 4.11: *distribution of the final sample of charged current events in the (x, y) plane. Open circles represent events where the FCAL timing is used to reconstruct the vertex ($\gamma_0 < 0.4$) while the dots are events where the CTD is used ($\gamma_0 > 0.4$).*

cuts in the preceding rows. In the fourth and fifth column the number of events in real data that remain after all cuts and the fraction that is selected are shown. A total of 1047 events are accepted in the final charged current sample.

cut	Monte Carlo % accepted of total	Monte Carlo % accepted in this step	data accepted events	data % accepted of total
$Q^2_{true} > 10\ \mathrm{GeV}^2$	100	100	—	—
FLT	88.2	88.2	—	—
SLT	83.1	79.8	—	—
TLT	83.4	79.2	—	—
DST	83.9	79.1	1319422	100
vertex requirement	93.0	74.9	626764	47.5
good track	91.1	71.2	294014	22.3
all tracks vs. good tracks	99.5	71.0	143587	10.9
spark rejection	100	71.0	135938	10.3
NC DIS	98.9	70.2	120189	9.1
photoproduction	72.3	58.2	7239	0.55
high-momentum track	100	58.2	7217	0.55
muon rejection	100	58.2	2700	0.20
FCAL cuts	99.9	58.2	2669	0.20
$P_T(-ir)$	74.4	56.1	1315	0.10
Q^2, y and P_T cuts	69.0	52.6	1047	0.08

Table 4.1: *summary of all selection cuts that are applied and their effect on Monte Carlo and on data. The second column shows the fraction of events in the ARIADNE charged current Monte Carlo sample that remains after the cut in the first column has been applied. In the third column the fraction of events is listed that remains after the cut in the first column and all preceding cuts have been applied. The number of events in data remaining after the cuts and the fraction that is selected are shown in the last two columns.*

Chapter 5

Identification of background muons

5.1 Introduction

The charged current event sample can be contaminated by cosmic and halo muons. Halo muons are produced in collisions between protons and residual gas in the beampipe or between protons and the beampipe wall, upstream of the detector. The resulting pions will decay into muons and some of those muons will travel parallel to the proton beam towards the detector. If they have enough energy they will traverse the veto wall, the rear calorimeter, the barrel calorimeter and finally the forward calorimeter depositing a trail of energy. This can result in a charged current trigger selection. An example of a halo muon event is displayed in figure 5.1.

Another source of background muons originates from cosmic rays. The cosmic muons that are found in the charged current sample can be overlapping with a real *ep* event or a beam-gas event as illustrated in figure 5.2. Another possibility is that the muon produces a bremsstrahlung photon in the calorimeter that might result in a large transverse momentum (see figure 5.3). Also multiple cosmic events form a substantial background.

This muonic background has to be removed from the charged current sample in an efficient and sophisticated way. To achieve this a special muon finder baptised MUFFIN has been developed. This muon finder searches for a topology consisting of long and narrow clusters of calorimeter cells consistent with a muon traversing the detector. If a muon is found the event is removed from the selected sample of charged current events.

In the remainder of this chapter a brief overview of the muon finder package will follow. A more elaborate description is available in [43] and in [44].

5.2 General description

MUFFIN assumes that the only reason for an event to be in the charged current sample is that a muon traversed the calorimeter. In other words, if all calorimeter cells belonging to the muon are removed then the remaining event will fail the trigger cuts. As the main charged current trigger is based on transverse momentum an event will be removed from the sample if the transverse momentum of the event without the muon is below a threshold which is set at 7 GeV.

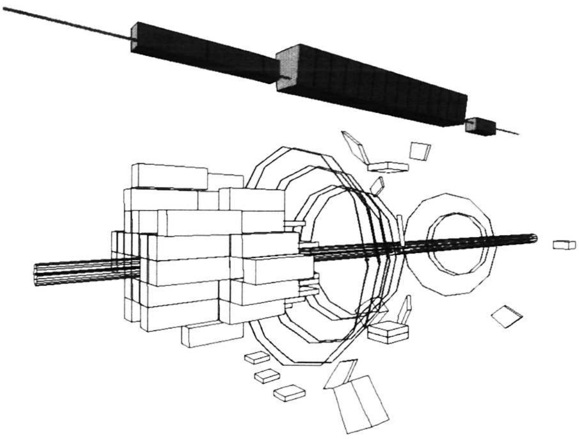

Figure 5.1: *example of a halo muon traversing the ZEUS detector, superimposed on a beam-gas event. The dark cells are the ones belonging to the halo muon and the line indicates the muon trajectory as found by the muon finder. In this plot and in later plots the dark thick cylinder is the beampipe while the thin lines indicate the contours of the inner tracking system. The calorimeter cells with energy are represented by grey or white blocks. CTD tracks are, in principle, also drawn in the picture.*

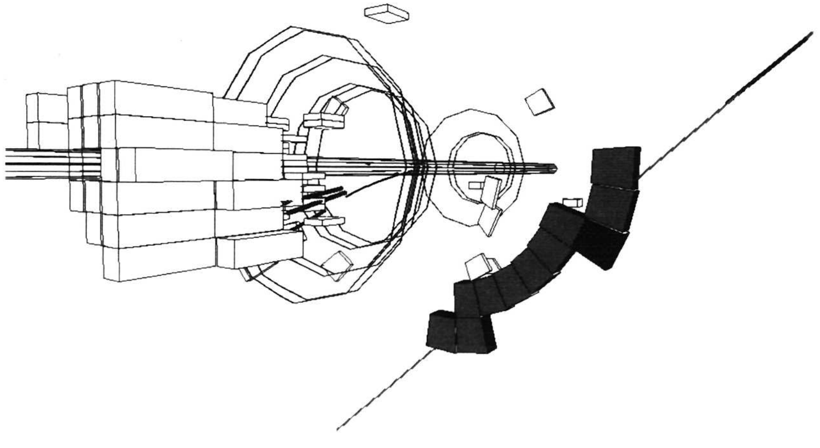

Figure 5.2: *example of a cosmic muon event traversing the barrel calorimeter, superimposed on a beam-gas event.*

The muon finder starts by looking for a possible muon pattern. This pattern is based on a combination of tracks from the muon and inner tracking chambers and clusters of calorimeter cells. Those combinations are found by dedicated algorithms that each have a different approach

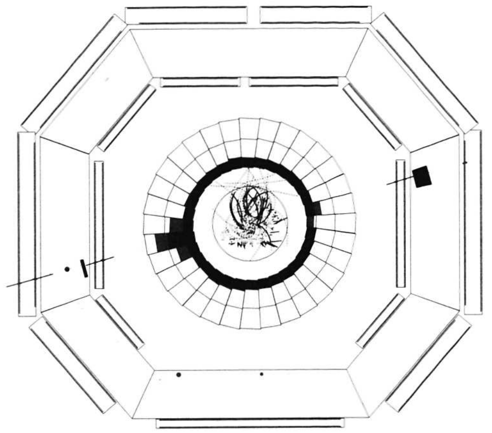

Figure 5.3: *transverse cross section of the ZEUS detector showing a cosmic muon that produces a bremsstrahlung shower in the barrel calorimeter. A part of this shower leaks into the inner detector. There the particles are bent by the magnetic field and they leave curved tracks in the CTD before depositing their energy in the barrel EMC cells. The tracking programme becomes quite confused by the abundance of particles.*

in finding muon patterns (see section 5.4). A muon "candidate" is then formed by calculating a set of parameters for each pattern which involves a three-dimensional linear fit to the calorimeter clusters. This fit yields the approximate trajectory traversed by the muon in the detector. To speed up calculations MUFFIN temporarily removes the candidate from the event and checks if the transverse momentum of the remaining event is still above the threshold value. If so MUFFIN will reject the candidate and search for other possible patterns.

For the candidates that pass this first step MUFFIN performs a more precise line fit to the clusters and recalculates all parameters. This set of parameters is then compared with a list of reference parameters [43] that characterise a traversing muon. If the candidate is identified as a muon the event is removed from the charged current sample.

5.3 Input data

As mentioned in the previous section MUFFIN is aimed at finding the calorimeter cells traversed by a cosmic or halo muon. Obviously the full geometry of the calorimeter has to be known by the muon finder. Each cell in the calorimeter is modelled as a box or several boxes that contain the scintillator-uranium sandwiches and the HES gaps. During a line fit a ray tracing algorithm is used to find the cells that are hit by the line (the muon trajectory). For this the calorimeter has been split up into 27 containers, $3 \times 3 \times 3$, and each of these containers is constructed of 27 boxes which then contain the calorimeter cells. When MUFFIN tries to find the cells that are hit by the muon trajectory it first checks which containers are hit. Inside each hit container it

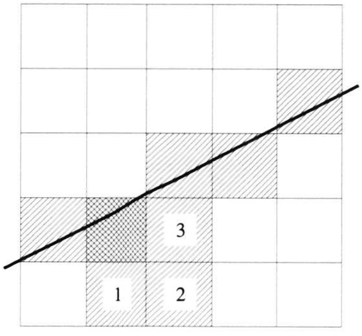

Figure 5.4: *schematic view (copied from [43]) of a muon traversing the calorimeter, producing a bremsstrahlung shower in the cross-hatched cell. Cells* 1, 2 *and* 3 *are part of the shower but are not hit by the line trajectory.*

checks which boxes are hit and only then it checks in each hit box which cells are hit.

Cells other than those hit by the fitted line may be associated to the muon track due to bremsstrahlung. This situation is schematically illustrated in figure 5.4 where the cells labelled as 1, 2 and 3 have energy because the muon produces a bremsstrahlung shower in the cross-hatched cell. MUFFIN will recognise such cells and give them an appropriate treatment when calculating the candidate parameters. An extreme example of such a showering muon is shown in figure 5.3 and another muon that showers in the wavelength shifter is displayed in figure 5.5.

MUFFIN tries to find muon patterns by combining calorimeter clusters. These clusters are composed of neighbouring cells where two cells are neighbours if they have a surface in common or if they touch each other at a common edge or corner. Cells in the outermost towers of the barrel calorimeter can be neighbours of cells in the FCAL and RCAL. Before searching for muon patterns the muon finder performs a line fit to the cells in each cluster which is used to determine the "shape" of the cluster. A long and narrow cluster is the most favoured shape as this is the most probable configuration of the energy depositions left by a minimum ionising particle. To speed up calculations this type of clusters is the first one MUFFIN looks at.

The muon finder uses tracks from the CTD that have been extrapolated to the inner surface of the calorimeter. One of the pattern recognition algorithms is based on high-momentum inner tracks connected to calorimeter clusters. Tracks are further used to separate the traversing cosmic or halo muon from genuine physics or beam-gas events.

The event vertex is used by MUFFIN to calculate the missing transverse momentum and energy. The distance of the muon to the vertex helps to discriminate the background muon from a muon coming from the vertex in an ep event. If there is no tracking vertex the muon finder uses the nominal vertex.

As can be expected the information from the forward, barrel and rear muon chambers is very useful for finding muon patterns in the detector and for muon identification. MUFFIN uses the full three-dimensional tracks from these chambers, but also BMUON and RMUON tracks that only have strip or wire information are used. For the latter type of tracks one of the coordinates is unknown.

To profit as much as possible from the muon chamber information MUFFIN tries to combine muon tracks (or rather muon track elements) with each other. Obviously the combination of two muon track elements far apart gives the best estimate of the muon trajectory in the detector.

5.4 Muon candidate finders

Eight different algorithms are used to find possible muon patterns in an event. The algorithms are executed one after the other until one of them gives a pattern that is identified as a muon. The sequence of algorithms inside MUFFIN is as follows

1. find patterns based on combined muon track elements.

2. find patterns based on single muon track elements.

3. find patterns based on combined inner tracks.

4. a quick search for halo muons based on calorimeter clusters only.

5. find halo muons close to the beampipe.

6. find muons that do not move along a straight line.

7. find patterns based on calorimeter clusters only.

8. find patterns based on calorimeter cluster timing.

All of these algorithms will be briefly explained below. More details are to be found in [43] and [44].

5.4.1 Muon track based finders

The finders based on combined and single muon track elements in the muon chambers work in the same way. A candidate is formed by all calorimeter clusters that are hit by the muon track elements and all candidate parameters are calculated with the highest precision. For the algorithm based on combined muon track elements no fit is performed as the line defined by the track elements is already the best estimate for the muon trajectory through the ZEUS detector. In principle this is also true for the candidates based on single muon track elements but the direction of the trajectory is less well constrained. Therefore, a fit is done in which only the direction of the trajectory is allowed to vary.

5.4.2 Combined inner track based finder

Sometimes the muon chambers fail to detect a traversing muon. The muon, however, can still leave two very nice back-to-back high-momentum tracks in the CTD that are connected with two calorimeter clusters. This is exactly the signature the combined inner track based finder looks for. An example of an event found by this algorithm is shown in figure 5.5 where a cosmic muon enters the barrel calorimeter from above and leaves the detector in the lower right corner. A shower is produced in the wavelength shifter between two BCAL modules and particles escape into the inner tracking detector. This algorithm does not involve a fit as the trajectory fixed by the two inner tracks is the best estimate of the muon trajectory.

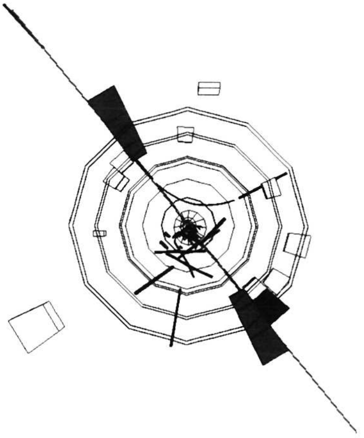

Figure 5.5: *example of a cosmic muon event that is found with the combined inner track finder. The muon travels in between two modules of the barrel calorimeter and produces a shower in the wavelength shifter.*

5.4.3 Halo muon pattern search

Two different algorithms perform a search for patterns that are compatible with a halo muon traversing the detector. The first algorithm combines calorimeter clusters that have the same position in the (x, y) plane into a candidate. A fast linear regression fit is performed on these clusters and MUFFIN decides whether the candidate looks promising enough to continue. This is done by applying the transverse momentum criterion as described previously. Also the number of cells without energy hit by the trajectory should be less than 40% of the total number of cells in the candidate. If so a more precise fit is performed and the set of parameters is calculated more accurately and compared with the reference parameters characterising a halo muon.

The other algorithm specialises in muons that are close to the beampipe which implies that they do not go through the barrel calorimeter. The pattern it looks for is a combination of one

FCAL and one RCAL cluster that is compatible with a halo muon connecting them. It is not unlikely that a low y neutral current DIS event is identified as a halo muon by this algorithm as the signature (positron in the RCAL close to the beampipe and a small proton remnant in the FCAL) is nearly the same as a halo muon. To prevent this MUFFIN checks if the muon candidate contains a positron and whether $E - P_z$ of the event is compatible with a DIS event. If so then the candidate is not identified as a muon.

5.4.4 Muons with a curved trajectory

A very special muon signature is generated by cosmic muons that lose nearly all their energy in the calorimeter. An example of such an event is shown in figure 5.6. A cosmic muon losing all of its energy will typically leave two energy deposits in the calorimeter that are connected by a curved track. The muon finder looks exactly for this curved track pattern. If this track can be connected with two clusters in the calorimeter a candidate is formed.

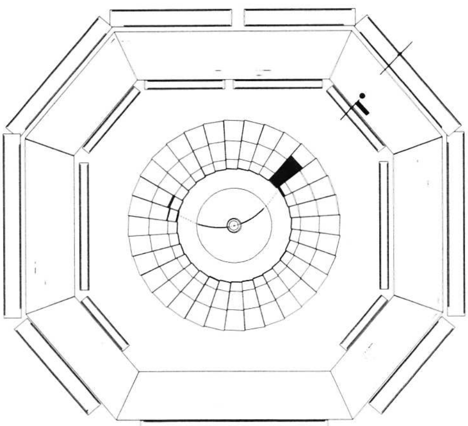

Figure 5.6: *transverse cross section of the detector showing an example of a cosmic muon travelling along a curved path. The muon enters the BCAL from the upper right corner and leaves a track in the BMUON. Then it deposits most of its energy in BHAC1 and enters the inner detector. The muon leaves a low momentum track in the CTD and re-enters the BCAL where it deposits the rest of its energy.*

5.4.5 Calorimeter cluster based finder

If none of the algorithms above could find a muon MUFFIN will try to find muon patterns that are only based on combinations of calorimeter clusters. This algorithm uses several sub-algorithms that each have a different approach in combining clusters. All algorithms start with a "seed cluster" and then try to add more clusters to this seed until the best possible combination is found. The algorithm involves many line fits making it rather slow.

An event can have more than one seed cluster and MUFFIN will try all of these until a muon is found. To speed up the calculations only clusters with three or more cells are allowed as a seed cluster. Moreover, a seed should not contain too many FCAL cells adjacent to the forward beampipe in order to avoid creating candidates that contain the proton remnant in an overlap event. Such candidates will never be identified as a muon as they contain many cells of which only a few are hit by the muon trajectory while MUFFIN requires that for a muon all or nearly all cells in the candidate are hit. The muon finder also looks which clusters have to be included in the muon candidate to get the transverse momentum of the event without the candidate below the threshold value. Obviously a muon candidate that does not include these clusters will never pass the threshold criterion.

A description of all sub-algorithms that add clusters to a seed can be found in [44]. MUFFIN performs a quick fit to the final list of clusters that is found by each sub-algorithm. It then decides whether this candidate has a chance of being identified as a muon as in section 5.4.3. If the candidate looks promising then a precise fit is done and all parameters are calculated with the highest accuracy. Otherwise the candidate is rejected and the muon finder will search for new combinations of clusters.

5.4.6 Calorimeter cluster timing based finder

The final algorithm that identifies possible muon candidates is based on the timing information from calorimeter clusters. Two clusters far away from each other are combined in a muon candidate if their timing information is compatible with a muon travelling from one to the other with the speed of light. Other clusters hit by the muon trajectory connecting the first two clusters are also added to the candidate.

Chapter 6

Kinematic reconstruction

6.1 Reconstruction methods

A DIS event can be characterised by four independent measurable quantities: the energy E'_e and the polar angle θ_e of the scattered positron, and the variables $\delta_h(= E_h - P_{z,h})$ and $P_{T,h}$. Here E_h is the energy of the hadronic final state and $P_{z,h}$ and $P_{T,h}$ are the longitudinal and transverse momentum, respectively. From the latter two an angle γ_h and an energy F_h can be defined which correspond to the polar angle and the energy of the scattered quark in the naive quark model (see figure 6.1):

$$\cos\gamma_h = \frac{P_{T,h}^2 - (E_h - P_{z,h})^2}{P_{T,h}^2 + (E_h - P_{z,h})^2} \tag{6.1}$$

$$F_h = \frac{P_{T,h}^2 + (E_h - P_{z,h})^2}{2\,(E_h - P_{z,h})} \tag{6.2}$$

Since a DIS event is completely determined by only two independent variables x and Q^2 there is some freedom to choose any two quantities out of the set of four to reconstruct the

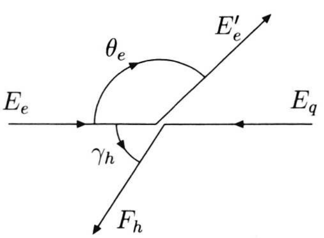

Figure 6.1: *schematic picture of a DIS event showing the definition of the measurable quantities E'_e, θ_e, F_h and γ_h. In this plot a positron with energy E_e comes from the left and a quark inside the proton with energy E_q from the right.*

kinematics. Traditionally the kinematics of a DIS event are reconstructed from the scattered lepton. This so-called "electron method" is used in all fixed target experiments. The kinematic variables calculated with this method are given by (using equations 1.2 and 1.5)

$$y_e = 1 - \frac{E'_e}{2\,E_e}(1 - \cos\theta_e) \tag{6.3}$$

$$Q^2_e = 2E_e E'_e(1 + \cos\theta_e) \tag{6.4}$$

while x_e is obtained from the relation $Q^2 = s\,x\,y$. Of course, this method is not available for charged current DIS as the scattered lepton is an antineutrino and remains undetected.

Complementary to the electron method is the Jacquet-Blondel (JB) reconstruction method that uses only the hadronic final state [59]. The kinematic variables are expressed in terms of $P_{T,h}$ and δ_h (or equivalently γ_h and F_h) as

$$y_{JB} = \frac{\delta_h}{2\,E_e} = \frac{F_h}{2\,E_e}(1 - \cos\gamma_h) \tag{6.5}$$

$$Q^2_{JB} = \frac{P^2_{T,h}}{1 - y_{JB}} = \frac{F_h^2 \sin^2\gamma_h}{1 - y_{JB}} \tag{6.6}$$

$$x_{JB} = \frac{Q^2_{JB}}{s\,y_{JB}} = \frac{E_e}{E_p}\frac{F_h(1 + \cos\gamma_h)}{2\,E_e - F_h(1 - \cos\gamma_h)} \tag{6.7}$$

This method is the only one that is available in charged current DIS. The resolution in Q^2_{JB} is given as

$$\left.\frac{\partial\,Q^2}{Q^2}\right|_\gamma = \frac{2 - y}{1 - y}\frac{\partial\,F}{F} \qquad \left.\frac{\partial\,Q^2}{Q^2}\right|_F = -\frac{E_p}{E_e}\frac{x\,y}{1 - y}\,\partial\gamma \tag{6.8}$$

from which it is clear that especially at high y the resolution in Q^2_{JB} is poor due to the factor $1/(1 - y_{JB})$. The same is true for the resolution in x_{JB}. At low y, however, the Jacquet-Blondel method gives a better estimate of y than the electron method [58].

To illustrate the effect of the finite resolution of the measured quantities $P_{T,h}$, δ_h, γ_h and F_h on the reconstruction of x and Q^2 it is instructive to draw isolines — lines of constant $P_{T,h}$ etc. — in the (x, Q^2) plane as is shown in figure 6.2. When isolines for a specific measurable quantity are close together the error on this variable leads to small uncertainties on the determination of x and Q^2. In figure 6.2a the isolines of $P_{T,h}$ are drawn. For low values of y the lines run parallel to the x axis which means that by measuring $P_{T,h}$ the Q^2 value is fixed and is nearly independent of y. On the other hand, this measurement contains no information about x. In the very high y region the isolines of $P_{T,h}$ and δ_h (or y) run parallel to each other which implies a large intrinsic uncertainty on both x and Q^2. A very precise measurement of the hadronic flow would be necessary to obtain a reasonable resolution. Therefore, events in the final charged current sample are rejected if they have a value of y exceeding 0.9. The same effect can be seen in figures 6.2b and 6.2c showing the isolines in γ_h and F_h. The lines of constant γ_h are evenly spread throughout the entire phase space, but for high y they run parallel to the isolines in F_h. The quark energy discriminates between different values of x, especially at high x, while it does not contain any information on Q^2.

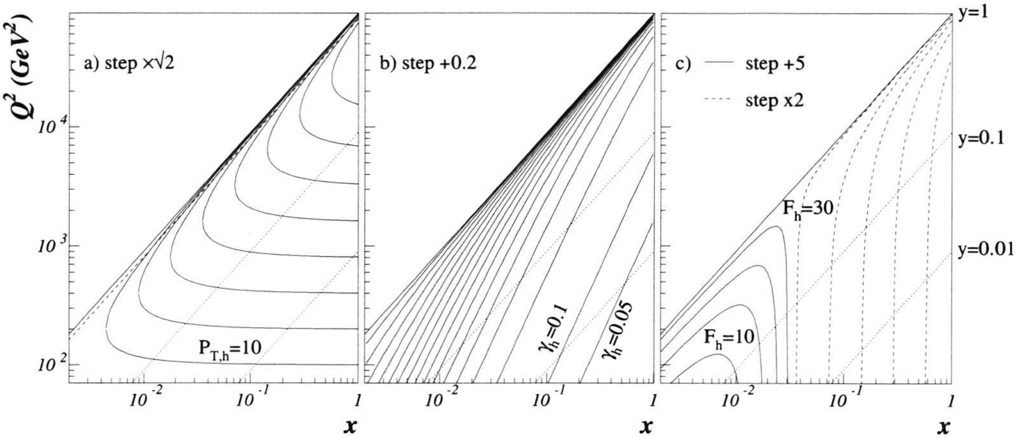

Figure 6.2: *isolines of $P_{T,h}$, γ_h and F_h in the (x, Q^2) plane. (a) Isolines in $P_{T,h}$ increasing with a factor of $\sqrt{2}$ starting from 10 GeV. The dashed line is the line $y = 0.9$ while the dotted lines represent $y = 0.1$ and $y = 0.01$. (b) Isolines in γ_h increasing in steps of 0.2. (c) Isolines in F_h increasing with steps of 5 GeV for $F_h < E_e$ and with a factor of 2 for $F_h > E_e$.*

The finite resolution in $P_{T,h}$ and δ_h is mainly caused by a mismeasurement of the hadronic energy. Unlike the positron the hadronic final state and thus the hadronic energy is not always fully contained in the calorimeter. First of all this can be due to particles escaping through the forward and backward beampipe. However, the energy loss through the backward beampipe is small for DIS events as the hadronic system is usually very forward. The loss through the forward beampipe can be substantial, but it has only little influence on the measurement of the kinematics. This is because the Jacquet-Blondel method is not very sensitive to this loss as the escaping particles only carry small $E - P_z$ and P_T.

The most serious source of energy loss that deteriorates the measured resolution is formed by energy loss in inactive material in front of the calorimeter. Later on in this chapter two methods will be presented that correct for this loss. Additionally there is also some loss, but to a lesser extent, due to leakage from the back of the calorimeter. The latter might be corrected for by using the information from the backing calorimeter. However, it turns out that only $\sim 1\%$ of the events that are selected in the final charged current data sample has more than 1 GeV of energy recorded in the BAC. Moreover, when this extra energy is taken into account for these events the relative change in $P_{T,h}$ and δ_h is at most 20%. The largest effect is observed in the low y region where the error on the reconstructed kinematics is already large. Because of this small effect and to avoid systematic uncertainties rising from the inclusion of an extra detector the backing calorimeter information will not be used. The correction for leakage will be effectively made by the aforementioned inactive material corrections.

For neutral current DIS events the problem of energy loss can be partially circumvented by using the double angle (DA) method [58] to reconstruct the event kinematics. This method combines the angular information from the scattered positron and the hadronic final state:

$$y_{DA} = \frac{\sin\theta_e(1-\cos\gamma_h)}{\sin\gamma_h+\sin\theta_e-\sin(\theta_e+\gamma_h)} \tag{6.9}$$

$$Q^2_{DA} = 4E_e^2\frac{\sin\gamma_h(1+\cos\theta_e)}{\sin\gamma_h+\sin\theta_e-\sin(\theta_e+\gamma_h)} \tag{6.10}$$

To first order these formulae are independent of the energy scale of the calorimeter. At low y, however, δ_h and thus the angle γ_h will suffer from noise in the calorimeter and the resolution in x and Q^2 deteriorates.

6.2 Calorimeter islands

The usual way in which the kinematic quantities are calculated is by summing over all individual calorimeter cells and taking the centre of the cell as the position of the energy deposit. This method is, however, rather unsophisticated as it does not take into account the shape of the showers generated by the particles that enter the calorimeter. It turns out that the resolution of the kinematic variables improves when individual cells are combined into clusters of cells that more or less correspond to the energy deposit of single particles or jets of particles.

To illustrate one of the effects of clustering consider the situation depicted in figure 6.3, where a few calorimeter cells around the forward beampipe are drawn. The cross indicates the beampipe and the grey boxes are FCAL cells with energy coming from the proton remnant. In the left plot δ_h is calculated by summing over all eight cells and taking the black dots as the positions of the cells. The black dot in the right plot is the position of the cluster formed by combining the eight cells. The contribution of the cluster to δ_h will be less than the total contribution of the individual cells. It turns out that this yields a better reconstruction of the kinematics of events, especially at low y. This improvement is due to a reduced contribution to δ_h of particles in the proton remnant that scatter on material inside the beampipe and that are detected in the FCAL. Apparently this effect is more important than the negative correction

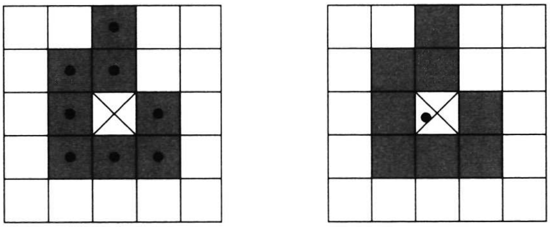

Figure 6.3: *schematic view of the proton remnant leading to energy deposits around the forward beampipe which is indicated by a cross. In the left plot the kinematic quantities are calculated by summing over individual cells, where the position of the cell is represented by a dot. In the right plot the cells are clustered and the position of this cluster corresponds to the position of the remnant.*

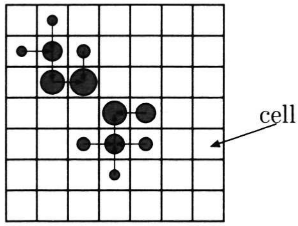

Figure 6.4: *schematic drawing of the formation of cell-islands. The size of the filled circles is a measure for the amount of energy deposited in a cell. Two separate clusters are formed by connecting cells to their nearest neighbour with highest energy.*

that is applied to particles in the proton remnant that are measured in the FCAL without additional scattering in the beampipe.

Of course, there are many possibilities to combine cells into clusters. Here the two stage algorithm as presented in [60] is adopted. In the first step of this algorithm cells in one layer of the calorimeter (FEMC, FHAC1, etc.) are combined into two-dimensional clusters, so-called cell-islands, which are formed as follows (see also figure 6.4). For each cell the algorithm makes a connection between the cell and its highest-energy neighbour. Two cells are neighbours if they have a common edge in a two-dimensional plot like figure 6.4. All cells that are connected to each other are then gathered into one cell-island. This procedure uniquely assigns each cell to one single cell-island.

In the second stage of the algorithm cell-islands that belong to the shower from a single particle or a jet of particles are combined into three-dimensional clusters extending over the full depth of the calorimeter. These clusters are called cone-islands or, in short, islands. The algorithm starts from HAC2 cell-islands and works inwards performing a clustering in (θ, ϕ) space. For each HAC2 cell-island the angular separation $\Delta\Psi$ in (θ, ϕ) space to all HAC1 cell-islands is determined. This separation is translated into a probability according to a distribution determined from a single pion Monte Carlo sample in which pions are shot from the vertex into the calorimeter thus allowing the study of the shower profile of hadrons. This probability is plotted as a function of $\Delta\Psi$ in figure 6.5 and is a measure for the probability that a HAC2 and a HAC1 cell-island originate from the shower of the same particle or the same jet of particles. A HAC2 cell-island is combined into a cluster with the HAC1 cell-island that gives the highest probability or, equivalently, the smallest angular separation, above a cut-off chosen at 0.1. When a HAC2 cell-island cannot be combined with a HAC1 cell-island the algorithm tries to combine it with an EMC cell-island, again by looking at the angular separation. A slightly different probability distribution is used for this with a probability cut at 0.3.

In a second step a similar procedure is performed to combine HAC1 cell-islands with EMC cell-islands. In the final step the algorithm tries to combine EMC cell-islands with other EMC cell-islands. These latter two steps employ the same probability curve as in the HAC2-EMC cell-island clustering step. All cell-islands that are combined with each other in this way form a cone-island.

The position $\vec{R}$ of a cone-island is usually estimated by the centre-of-gravity of all consti-

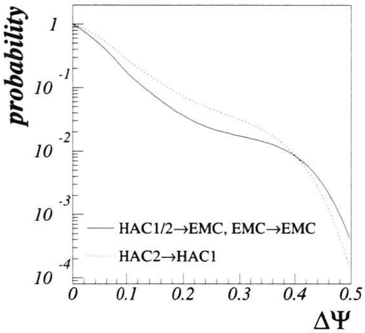

Figure 6.5: *curves giving the probability that two cell-islands with angular separation $\Delta\Psi$ in (θ, ϕ) space correspond to the same particle shower. The dashed curve gives the probability after combining a HAC2 and a HAC1 cell-island, the full curve corresponds to the combination of a cell-island with an EMC cell-island.*

tuting cells and is computed as

$$\vec{R} \equiv \frac{\sum_i w_i \vec{r}_i}{\sum_i w_i} \tag{6.11}$$

where $\vec{r}_i$ are the geometric positions of the centres of the individual cells i in the island. The weights w_i are usually taken as the energy E_i recorded in the cell. However, this linear weighting turns out to yield systematic shifts in the polar angle θ of the cluster. These biases can be removed by introducing two modifications. In the first place the position of the energy deposit inside a cell is not taken as the geometric centre of that cell. Instead the position is shifted from the centre in one dimension in the direction of the imbalance of the cell over a distance δx that depends logarithmically on the imbalance:

$$\delta x = \frac{\lambda}{2} \left| \ln \frac{E_{PMT1}}{E_{PMT2}} \right| \tag{6.12}$$

where E_{PMT1} and E_{PMT2} are the energies recorded in the two photomultipliers. The magnitude of λ has been extracted from test beam data as 54 cm [61]. This correction works properly within ± 8 cm from the centre of the cell. In the outer regions close to the wavelength shifters $\delta x = \pm 10$ cm is taken.

The second modification involves the weights w_i. Instead of just taking the energy E_i as a weight a logarithmic function of E_i is used:

$$\begin{aligned} w_i^{EMC} &= \max\left\{0,\, W_e + \ln \frac{E_i}{E_T}\right\} \\ w_i^{HAC} &= \max\left\{0,\, W_h + \ln \frac{E_i}{E_T}\right\} \end{aligned} \tag{6.13}$$

where $E_T = \sum E_i$ is the total energy of the island of which cell i forms a part and W_e and W_h are tuned parameters which are set to 4 and 2, respectively. This function properly takes into account the exponential fall off of the energy distribution from the shower maximum inside a cell [62]. The reason for introducing two parameters W_e and W_h is to account for the different sizes of the EMC and HAC cells.

6.3 Backsplash

After kinematic reconstruction of charged current events a systematic bias is observed in the reconstructed hadronic angle γ_h. In figure 6.6a the relative bias $(\gamma_h - \gamma_{true})/\gamma_{true}$ is plotted as a function of y_{true}. This bias is small at high values of y but increases to 20% at low y. It turns out that this overestimation is partly due to scattering of low momentum particles in material between the primary vertex and the calorimeter and partly due to backsplash from the calorimeter surface [63]. The scattered particles are then measured at higher polar angle compared to their original direction and thus the reconstructed hadronic angle γ_h of the event is increased. This effect is most noticeable at low y as the relative contribution of backward scattered low momentum particles grows with decreasing y.

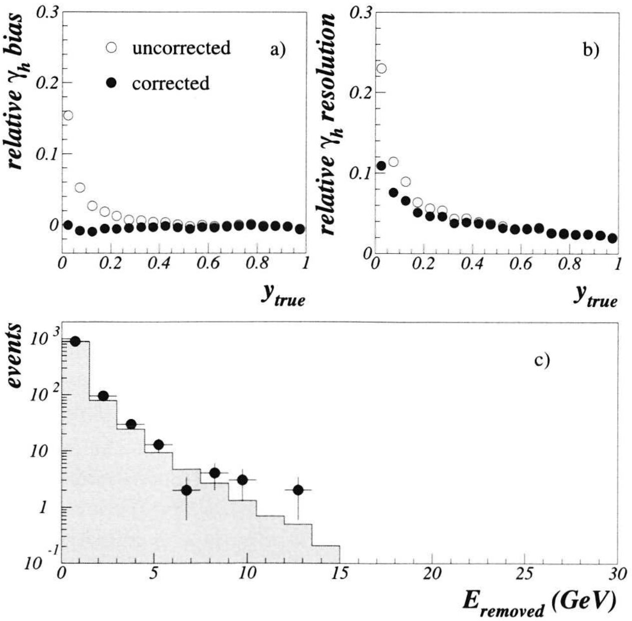

Figure 6.6: *effect of the backsplash correction on the reconstruction of the angle γ_h, (a) relative bias in γ_h as a function of true y before (open circles) and after (dots) the correction, (b) relative resolution in γ_h before and after the backsplash correction, (c) comparison of energy removed by the correction in the final charged current data sample (dots) and in the ARIADNE Monte Carlo sample (histogram).*

The bias in γ_h is minimised when clusters with an energy below 3 GeV and with a polar angle larger than γ_{max} are removed. The value of γ_{max} depends on the hadronic angle γ_h as

$$\gamma_{max} = \begin{cases} 0.151 + 1.372 \cdot \gamma_h & \gamma_h < 1.95 \\ 2.826 + 0.259 \cdot (\gamma_h - 1.95) & \gamma_h > 1.95 \end{cases} \tag{6.14}$$

This definition of γ_{max} has been obtained from a high Q^2 neutral current Monte Carlo sample by requiring that not more than 1% of the clusters not related to the two effects described above are removed. This yields a reconstruction of γ_h closest to the true value. After this first pass of cluster removal the value of γ_h is recalculated and the procedure is repeated until the change in γ_h is less than 1%. Typically this procedure converges after two or three steps.

The agreement between the removed energies in data and in Monte Carlo is shown in figure 6.6c. In this plot the dots represent charged current data and the shaded histogram is the Monte Carlo expectation. The removed energy can be quite sizeable but this is only the case for a few events and the removed energy is always less than 10% of the total energy. In figure 6.6a the relative deviation of γ_h from the true value after the backsplash correction is shown. The bias at low y has now almost completely vanished. Moreover, the resolution improves substantially, from about 25% to 10% as illustrated in figure 6.6b.

6.4 Island energy correction

Not all the energy of an event will be contained in the calorimeter, mainly because energy is lost in inactive material between the interaction vertex and the calorimeter. This energy loss will result in a substantial bias in the reconstruction of the kinematic variables. To reduce this bias the kinematic reconstruction employs islands instead of individual calorimeter cells. This gives a significant improvement in the reconstruction of very forward (low y, high x) events (see also section 6.2).

A further improvement in the reconstruction is obtained when the energy of each individual island is corrected. Two different correction methods are presented here. Both methods multiply the energy of each island with a correction function that depends on the energy and the polar angle of the island. Thus it is implicitly assumed that the energy loss is independent of the azimuthal direction which is a reasonable assumption in view of the symmetry of the detector.

The first method — referred to as method I — assumes that the correction function $\mathcal{C}$ can be factorised in a part depending on the island's energy E_{isl} and a part depending on its angle θ_{isl}:

$$\mathcal{C}(E_{isl}, \theta_{isl}) = \mathcal{E}(E_{isl})\ \Theta(\theta_{isl}) \tag{6.15}$$

This factorisation is only valid if the fractional energy loss of a particle is independent of the amount of dead material that is traversed. This is true within 10% for pions with initial energies ranging from 0.5 GeV to 100 GeV.

For every event the islands are binned according to their energy (17 bins) and to their polar angle (30 bins) into two one-dimensional grids. Then, instead of using a functional form, the correction functions are approximated by a set of independent parameters, one for each of the

17 + 30 bins. The correction does not take into account the position of the event vertex. Since most of the events have a vertex in a small interval around the nominal position this is justified.

The correction factors are obtained from the ARIADNE charged current Monte Carlo sample that is generated with a Q^2 cut of 10 GeV^2 and no x cut. A fiducial sample is obtained by imposing a measured vertex between -30 cm and 30 cm which ensures that the vertex position does not introduce a bias in the event kinematics. Furthermore, a minimum Q^2 cut of 200 GeV^2 and a P_T cut of 9 GeV are applied and a y cut of 0.05. This latter cut excludes events with a large enery loss through the forward beampipe which cannot be corrected by this method.

With the help of a MINUIT fit [64] the 47 different factors are obtained. During this fit the following function $\mathcal{F}$ is minimised

$$\mathcal{F} = \left(\frac{P_{T,cor} - P_{T,true}}{P_{T,true}}\right)^2 + \left(\frac{y_{cor} - y_{true}}{y_{true}}\right)^2 \tag{6.16}$$

where $P_{T,cor}$ and y_{cor} are the transverse momentum and y calculated with the corrected islands. The result of the fit is displayed in figure 6.7 where the upper plot shows the correction factors Θ as a function of the polar angle of the island while the lower plot shows $\mathcal{E}$ as a function of the island's energy. The transition zones between FCAL/BCAL and BCAL/RCAL are clearly visible in the upper plot. The large correction required at the corresponding angles is in agreement with the large amount of inactive material in these partly uninstrumented regions.

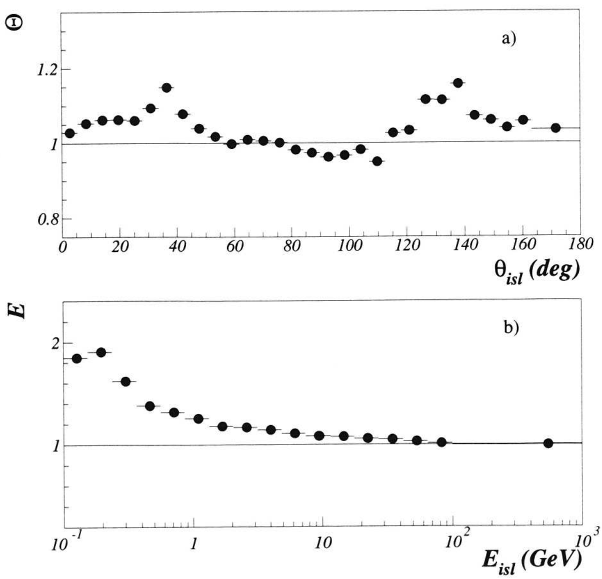

Figure 6.7: *correction factors Θ (upper plot) and $\mathcal{E}$ (lower plot) as a function of the island's angle and energy, respectively.*

It has been checked that the correction factors obtained in an analogous procedure from the MEPS sample are the same as for the ARIADNE sample. Only at high θ_{isl}, a region with limited statistics, and at low energies a small difference is observed.

The second correction method (method II) [63] uses a correction function depending on the energy of the island and the amount of inactive material in X_0 between the interaction vertex and the position of the island in the calorimeter. This function is parametrised as

$$\frac{E_{isl}}{E_{true}} = \left(1 - (p_1 + p_2 X_0)\, e^{(p_3 + p_4 X_0) E_{true}}\right) \left(1 - (p_5 + p_6 X_0)\, e^{(p_7 + p_8 X_0) E_{true}}\right) p_9 \qquad (6.17)$$

where the values of the nine free parameters p_i are obtained from a fit to a high Q^2 neutral current DIS Monte Carlo sample. At the beginning of the fit the left and right factor have been chosen to describe the low and high energy behaviour of the function, respectively. Note that as this function depends on E_{true} it has to be inverted to get a proper correction function depending on the measured energy E_{isl}. The fit yields the following values for the nine parameters

p_1	0.08 ± 0.02	p_5	-0.087 ± 0.009
p_2	0.06 ± 0.01	p_6	0.108 ± 0.007
p_3	0.02 ± 0.06	p_7	0.012 ± 0.004
p_4	-0.18 ± 0.05	p_8	-0.020 ± 0.003
p_9	0.95 ± 0.01		

The fit function is shown in figure 6.8a for three different amounts of inactive material expressed in the number of radiation lengths X_0. The energy loss is quite sizeable at low energies and can be as large as $\sim 35\%$. The fractional energy loss diminishes towards higher energies and is practically constant and independent of the amount of inactive material above 100 GeV. In figure 6.8b the inverted correction function is shown as a function of the measured island energy. The lines are the correction obtained in method II while the dots show the ratio of corrected and measured island energy for the correction of method I evaluated at the angle(s) θ_{isl} that correspond to the given amount of inactive material. Between 1 GeV and 100 GeV the two methods give the same correction although for the highest amount of inactive material there is some difference above 10 GeV. Below 1 GeV the two corrections differ as method I gives a larger correction. The error on the correction in this region is, however, rather large. It has been observed that variations in the parameters within 20% of the nominal value for energies below 0.5 GeV only have a negligible effect on the corrected kinematic variables. Above 100 GeV the fits are only loosely constrained as very energetic islands only occur in the very forward region and thus hardly contribute to δ_h and $P_{T,h}$.

For low energy islands it is not only energy loss by hadronic interactions in inactive material between the calorimeter and the primary vertex that causes a difference between the measured and the true energy of the island. Test beam experiments have shown [65] that the e/h ratio, the ratio of the response of the calorimeter to electrons and to hadrons, is close to 1 for energies above 3 GeV, but that the ratio decreases when going to lower energies. This is illustrated in figure 6.9 that shows the ratio e/h for pions and protons as a function of the kinetic energy of

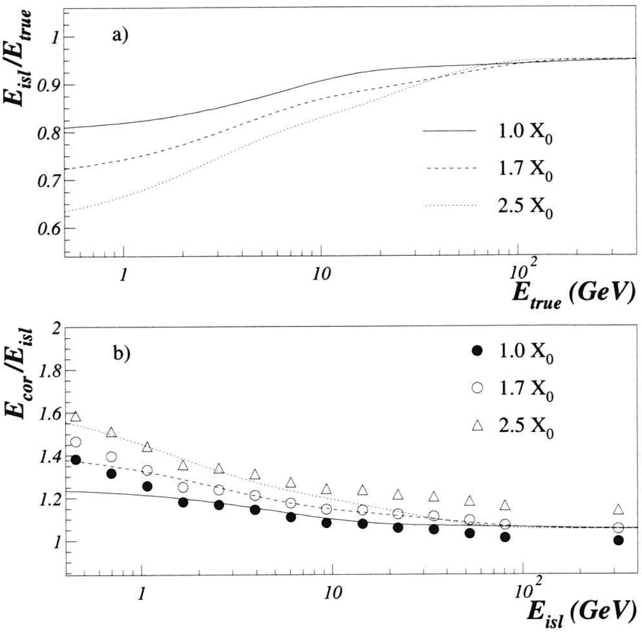

Figure 6.8: *(a) correction function of method II as a function of the true energy of an island for various amounts of inactive material, (b) comparison between method I (points) and method II (lines) of the ratio of the corrected and the measured energy of an island as a function of the measured energy.*

the particles. The response to pions at low energies can be qualitatively understood. Since the interaction length of pions is $1.2\,\lambda$ and energy loss in the calorimeter by ionisation for minimum ionising particles (mips) is 200 MeV/λ pions with kinetic energies below 250 MeV lose their energy almost completely by ionisation before undergoing any hadronic interaction. Therefore, a ratio $e/h \sim e/mip$ is expected where e/mip is equal to 0.62 for the ZEUS calorimeter. This effect is observed both for pions and for protons and yields an overestimation in the energy measurement of low energy islands. Correction method II takes this different behaviour of low energy islands into account in an additional correction.

The bias and resolution of the uncorrected and corrected kinematic variables Q^2, x and y are shown in figure 6.10 for the ARIADNE charged current Monte Carlo sample. Open triangles represent the uncorrected variables calculated with islands while the corrected ones are indicated by dots (method I) and open circles (method II). The position of each point gives the bias in the reconstruction and the error bar represents the resolution. These are obtained by means of a Gaussian fit to the distribution of $(A_{rec} - A_{true})/A_{true}$ for Monte Carlo events that pass the charged current selection cuts where A denotes either Q^2, x or y. Both corrections succeed in reducing the bias to within a few percent with the exception of the very low x region.

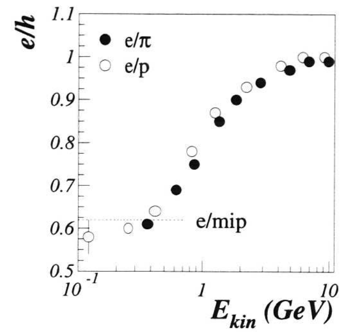

Figure 6.9: *ratio e/h of the response of the calorimeter to electrons and the response to pions (dots) or protons (open circles) as a function of the kinetic energy E_{kin}. At low energies the ratio approaches the theoretical value e/mip ~ 0.62 where the hadrons behave as minimum ionising particles (mips).*

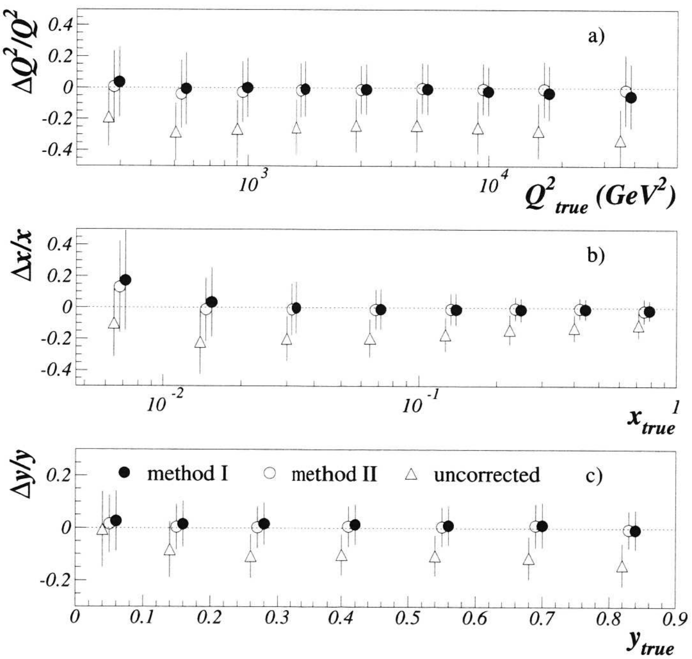

Figure 6.10: *bias and resolution of the uncorrected (triangles) and corrected (dots and open circles) kinematic variables Q^2, x and y as a function of their true value for the ARIADNE charged current Monte Carlo sample. Both correction methods succeed in removing the bias in the whole kinematic range except at very low x.*

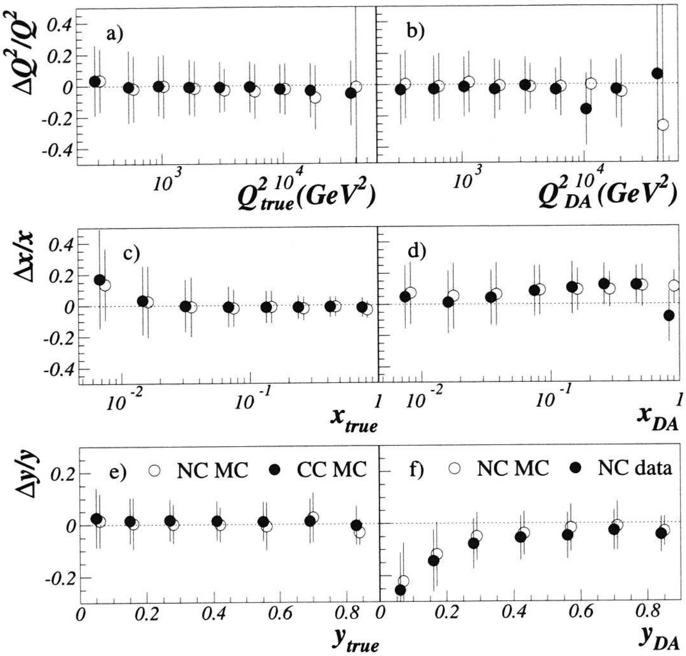

Figure 6.11: *bias and resolution in Q^2, x and y for CCfied neutral current data and Monte Carlo and for charged current Monte Carlo. The three plots on the left show the bias and resolution as a function of the true kinematics after correction with method I for CCfied Monte Carlo data (open circles) and charged current Monte Carlo (dots). The plots on the right show the bias and resolution as a function of the double angle kinematics for CCfied neutral current Monte Carlo (open circles) and CCfied neutral current data (dots).*

The two correction methods work very well for charged current Monte Carlo events. However, it has to be checked that they also give reliable results for charged current *data*. To this end the samples of CCfied neutral current data and Monte Carlo are used. When the two correction methods are applied on CCfied neutral current Monte Carlo very similar results should be obtained as for genuine charged current Monte Carlo. Analogously, neutral current data and Monte Carlo should agree with each other.

In the plots on the left of figure 6.11 the open circles denote the residual bias in Q^2, x and y after correction for CCfied neutral current Monte Carlo while the dots represent charged current Monte Carlo. Only results for method I are shown here. Over the whole range in Q^2, x and y the two sets of Monte Carlo data basically have the same bias and resolution thus showing that the hadronic final states of both samples are very similar.

In the three plots on the right of figure 6.11 CCfied neutral current Monte Carlo (open circles) is compared with CCfied neutral current data. The bias and resolution in Q^2, x and y are now given as a function of the double angle kinematics. Since the data sample only has events above ~ 300 GeV^2 while the Monte Carlo starts at 100 GeV^2 a minimum Q^2 cut of 300 GeV^2 is applied to both samples. The remaining bias and resolution after correction agree very well for both samples over the whole kinematic range. The deviations at high Q^2 and high x are to be blamed on lack of statistics in that particular region of the phase space.

Chapter 7

Cross section measurement

In the previous chapters the selection of the charged current data sample and the reconstruction of the event kinematics have been discussed. This chapter will focus on the extraction of charged current cross sections from this sample. For this a bin-by-bin unfolding method is employed in which the kinematic range is divided in a certain number of bins in which the cross sections are measured. Three measurements of single differential cross sections are presented ($d\sigma/dQ^2$, $d\sigma/dx$ and $d\sigma/dy$) as well as the double differential cross section $d\sigma/dxdQ^2$.

7.1 Bin definition

To minimise the systematic and statistical error in the measurement of the cross sections it is necessary to use a binning of the kinematic range that is not too narrow. If the bins are too narrow they will contain only a small number of events thus increasing the statistical error. Moreover, migration effects between neighbouring bins become important and a very accurate description of migration in the Monte Carlo simulations is required. Therefore, the bins are chosen such that the width is several times larger than the resolution in the variable that is binned.

For the measurement of the single differential cross section $d\sigma/dQ^2$ nine bins are used ranging from 200 GeV^2 to 60000 GeV^2. The resolution in each bin after kinematic correction is more or less constant, around 20%, over the entire Q^2 range as shown in figure 6.10a. The bins have equal width in $\log Q^2$ between 400 GeV^2 and 22494 GeV^2 while the lowest and highest Q^2 bins have a somewhat larger width.

In figure 6.10b the resolution in x is displayed as a function of x, varying from about 30% in the lowest x bins to 10% at high x. As the lowest x bin still has a large bias after correction the cross section measurement is performed for $x > 0.01$. Seven equidistant bins in $\log x$ are used, three between $x = 0.01$ and $x = 0.1$ and four between $x = 0.1$ and $x = 1$. The resolution in y varies from about 10% at low y to 7% at high y as shown in figure 6.10c. For the measurement of $d\sigma/dy$ the y range is divided linearly into seven bins, two between $y = 0$ and $y = 0.2$ and five between $y = 0.2$ and $y = 1$

The values of x and Q^2 where the cross sections are quoted, x_c and Q_c^2, are chosen close to the logarithmic centre of each bin, except in the highest x and Q^2 bins where they are chosen

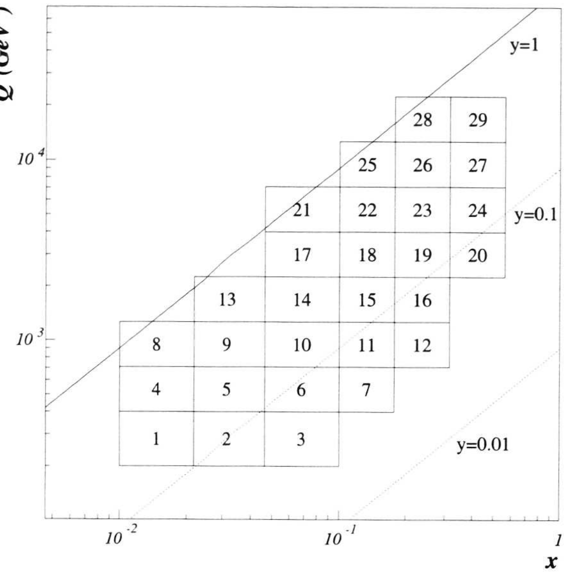

Figure 7.1: *(x, Q^2) binning used for the measurement of the double differential cross section. It is a combination of the binnings used for the extraction of $d\sigma/dQ^2$ and $d\sigma/dx$. A number is assigned to each bin for later reference.*

somewhat lower than the logarithmic centre reflecting the steeply falling cross sections. The single differential cross sections as a function of y are quoted at the centre y_c of each bin.

The binning in (x, Q^2) used for the measurement of the double differential cross sections is taken as a mixture of the binning in x and Q^2 used for the measurement of $d\sigma/dx$ and $d\sigma/dQ^2$. The highest x and highest Q^2 bins are not used, however, as the statistics in these bins are too limited to allow a reliable measurement of $d\sigma/dxdQ^2$. Figure 7.1 shows the resulting grid. For each of the 29 bins the distributions of $(Q^2_{rec} - Q^2_{true})/Q^2_{true}$ and $(x_{rec} - x_{true})/x_{true}$ are shown in figure 7.2. These plots show that the resolutions in both x and Q^2 deteriorate with increasing y. The best resolutions are found in the region of high x and high Q^2.

The measurements of the cross section are restricted to bins with a high purity $\mathcal{P}$ and a high acceptance $\mathcal{A}$. In this way large corrections for migration effects are avoided. Purity and acceptance are defined as follows:

- **purity** $\mathcal{P}$: number of events measured and generated in a bin divided by the total number of events measured in that bin.

- **selection efficiency** ϵ_{sel}: number of events generated in the bin and measured somewhere in the allowed kinematic range divided by the number of events generated in that bin.

- **acceptance due to migration** ϵ_{mig}: number of events measured in the bin divided

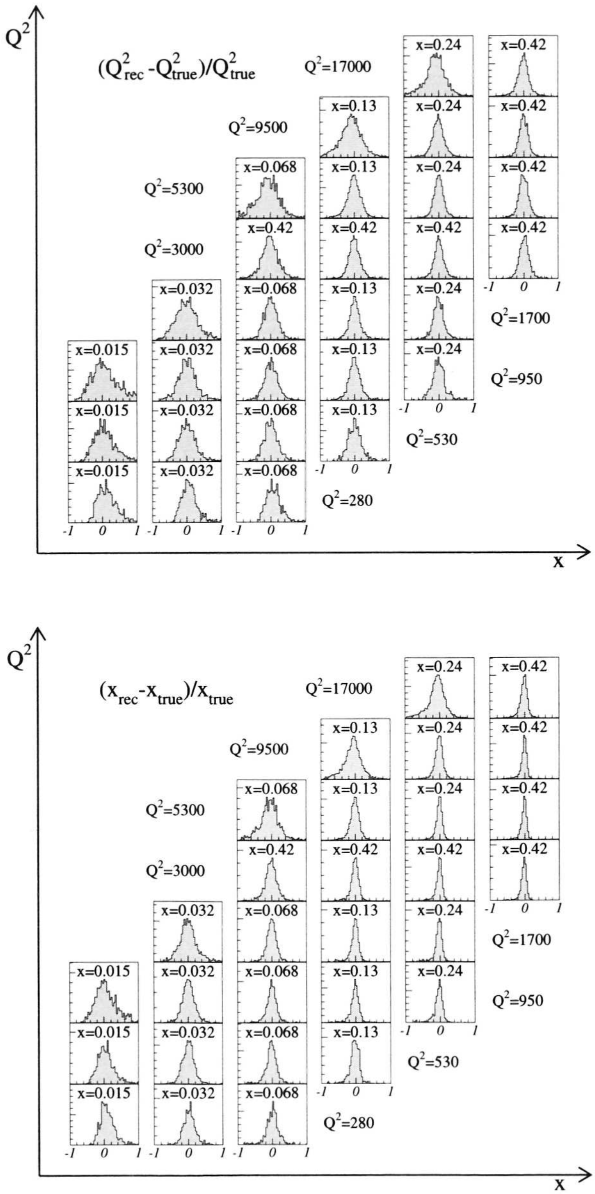

Figure 7.2: *distribution of* $(Q^2_{rec} - Q^2_{true})/Q^2_{true}$ *and* $(x_{rec} - x_{true})/x_{true}$ *in each* (x, Q^2) *bin obtained from the ARIADNE charged current Monte Carlo sample.*

by the number of events generated in that bin and measured somewhere in the allowed kinematic range.

- **total acceptance** $\mathcal{A}$: number of events measured in the bin divided by the number of events generated in that bin.

Here "measured in the bin" means that the event is reconstructed in the bin and also satisfies the selection criteria. "Measured somewhere" means that the event passes the selection cuts and is reconstructed in a certain bin in the allowed kinematic range. Note that with this set of definitions both the acceptance due to migration and the total acceptance in a bin can be larger than 1. The following relation holds

$$\mathcal{A} = \epsilon_{sel} \times \epsilon_{mig} \tag{7.1}$$

The purity, efficiency and acceptance in the different Q^2, x, y and (x, Q^2) bins are listed in tables 7.1 and 7.2. In the entire kinematic plane the purity is larger than 60%. Only at high y it can be as low as 40%. Also the selection efficiency is smallest at high y, mainly due to the photoproduction rejection cuts. It increases towards lower y but is again small at very low y, i.e. the region where the hadronic angle $\gamma_0 < 0.4$. A similar behaviour is observed for the acceptance. The total acceptance for events with Q^2 exceeding 200 GeV^2 is 68%.

7.2 Background estimation

The final selected data sample might still be contaminated by events originating from ep interactions other than charged current DIS. The magnitude of this background is estimated with the Monte Carlo samples that have been described in chapter 3. In tables 7.1 and 7.2 the estimated background is given for each of the different ep processes together with the observed number of events N_{obs} in the signal sample. The estimated fraction of background events in the final sample is typically below 1% at high Q^2 but increases to 20% in the lowest Q^2 region, below 400 GeV^2. Photoproduction and di-muon events are the main source of background at low Q^2 while W production dominates at high Q^2. In the region where $y < 0.1$ the di-muon channel is the largest background.

Note that background originating from neutral current DIS is not included in these tables. This is because it is almost impossible to estimate this particular background from Monte Carlo simulations as the bulk of the events rejected by the cuts in section 4.5 are at very low Q^2. In this region the neutral current cross section amounts to several hundred nanobarns. Millions of events would have to be generated to get an equivalent luminosity that is a few times the luminosity of the data. Therefore, the contamination coming from NC DIS is estimated by a visual scan of all events in the final sample. As no such events are found the remaining neutral current DIS background can be neglected.

7.3 Unfolding the cross sections

The single and double differential cross sections are obtained via a bin-by-bin unfolding method. The measured integrated cross section σ_{meas} in a bin is given by the expression

$$\sigma_{meas} = \frac{N_{obs} - N_{bg}}{\mathcal{A}\,\mathcal{L}} \tag{7.2}$$

where N_{obs} is the observed number of events in the bin and N_{bg} is the total number of background events in the bin as expected from the Monte Carlo simulations. The total acceptance of the bin is denoted as $\mathcal{A}$ and $\mathcal{L}$ is the total integrated luminosity collected during the different running periods, which amounts to 47.53 pb^{-1}.

The measured cross section includes the electroweak radiative effects as discussed in section 1.3. The correction factor to provide the Born level cross section is defined as

$$C_{rad} = \frac{\sigma^{SM}_{Born}}{\sigma^{SM}_{rad}} \tag{7.3}$$

where the numerator is the integrated Standard Model Born cross section without electroweak radiative effects which is obtained by numerically integrating equation 1.16 over the bin. The Standard Model cross section σ^{SM}_{rad} including electroweak radiative corrections is calculated using HERACLES 4.6.2[1]. The measured integrated Born cross section is then given by

$$\sigma_{Born} = \sigma_{meas} \times C_{rad} \tag{7.4}$$

Finally, the quoted differential cross section, for example $d\sigma/dQ^2$ at $Q^2 = Q^2_c$, is calculated as

$$\left.\frac{d\sigma}{dQ^2}\right|_{Q^2=Q^2_c} = \frac{\sigma_{Born}}{\sigma^{SM}_{Born}} \times \left.\frac{d\sigma^{SM}_{Born}}{dQ^2}\right|_{Q^2=Q^2_c} \tag{7.5}$$

No further iterations are done as the resulting changes in the extracted cross section are small compared to the experimental errors. A similar procedure is used for extracting $d\sigma/dx$, $d\sigma/dy$ and $d\sigma/dxdQ^2$. In this manner the effect of the selection cuts and migration is corrected and the cross sections are extrapolated to the full kinematic range. In particular the Monte Carlo simulations are used to extrapolate the cross sections to the y region above 0.9 that is rejected by the selecting criteria. The differential cross sections $d\sigma/dx$ and $d\sigma/dy$ are quoted in the region $Q^2 > 200$ GeV^2.

The statistical errors on the cross sections are calculated using the square root of the number of measured events N for $N > 100$. Otherwise they are computed from 68% Poisson confidence intervals around N.

[1]Note that this version of HERACLES is different from the one used in the charged current Monte Carlo samples. Version 4.6.2 has an improved description of electroweak radiative effects. The effect of this on event distributions and acceptance calculations is negligible.

7.4 Systematic checks

The most important sources of systematic uncertainties in the determination of the cross section are the energy scale of the calorimeter, the modelling of the QCD cascade and the effects of the selection cuts. Other systematic errors include the uncertainty in the parton density functions and in the photoproduction background subtraction. The results of the systematic studies that have been performed are summarised below. Also comparisons are made with CCfied neutral current data to investigate the quality of the description of the charged current data by the Monte Carlo simulations.

7.4.1 Calorimeter energy scale

The energy scale of the calorimeter is known with an accuracy of 3%. A variation in the scale will obviously affect the reconstructed values of Q^2 and x and thus the measured cross section. Especially at high Q^2 the systematic errors introduced by the scale uncertainty can be sizeable because of the steeply falling cross section in that region.

In principle the systematic error due to the energy scale uncertainty is determined from the number of events that is measured with the scale changed compared to the nominal number of events. However, this poses a problem as the statistics of the data sample are rather poor in the bins where the effect is expected to be maximal. Thus it is not possible to separate the systematic effect due to the scale uncertainty from the statistical error. To circumvent this problem the scale is changed in the Monte Carlo simulations and the relative systematic error δ_{syst} is determined as

$$\delta_{syst} = \frac{N_{scaled} - N_{nominal}}{N_{nominal}} \tag{7.6}$$

where $N_{nominal}$ is the nominal number of events expected from the ARIADNE Monte Carlo sample after all cuts and N_{scaled} is the number of expected events with the scale changed.

In some regions of the kinematic plane the effect of scaling the calorimeter energies up or down by 3% is very small, e.g. around $Q^2 \sim 2000$ GeV^2 where the shift in the number of expected events is always slightly positive. In these cases a change of 2% or 1% in the energy scale might give a larger (and opposite) effect than a 3% change. Therefore, the positive error coming from the energy scale uncertainty is determined as the largest positive deviation from the nominal number of expected events when the scale is changed by $\pm1\%$, $\pm2\%$ or $\pm3\%$. Similarly the negative error is determined as the largest negative deviation. Results on the energy scale systematic errors are summarised in tables 7.1 and 7.2. The systematic errors in the measured cross sections are typically below 10% but increase to $\sim 70\%$ in the highest Q^2 bin and 35% in the highest x bin.

7.4.2 QCD cascade

To test the sensitivity of the cross sections to the details of the simulation of the higher order QCD effects in the hadronic final state, the whole analysis is repeated using the MEPS Monte Carlo set instead of the ARIADNE sample. The largest effects on the cross section are observed at low Q^2 (8%) and at low x (5%). At low y the variation in the cross section is about 2% and rises to 4% in the bins at the highest y values.

7.4.3 Parton density function

In the Monte Carlo samples the CTEQ4D parton density function parametrisation is used to describe the partonic content of the proton. To examine the sensitivity of the acceptance determination and the bin centring correction factor on variations in the PDFs also the MRSA, MRSH and GRV94 sets of PDFs and the NLO QCD fit are considered. The events in the ARIADNE Monte Carlo sample are reweighted with these alternative PDFs and new acceptance correction factors are determined.

The variations in the acceptance compared to the nominal value are very small, typically less than 1%. Only at high Q^2 and at high y the acceptance changes by as much as 2%. The resulting error on the cross section can safely be ignored in view of the large systematic error due to the energy scale uncertainty in these regions of the kinematic plane. In all of the (x, Q^2) bins the variation in the acceptance is less than 1%. The QCD fit yields larger variations in the acceptance, although in most of the bins these variations do not exceed the 3% level. Only in the highest Q^2 bin the acceptance changes noticeably, decreasing by about 8%.

The measurement of the differential cross section in a given bin according to equation 7.5 uses the ratio of the differential to the integrated Standard Model Born cross sections. This ratio is, in principle, sensitive to the Q^2 and x dependence of the parton density functions within the bin. Evaluating the ratio with the aforementioned sets of PDFs yields an uncertainty of 6% in the highest Q^2 bin and 3% in the highest x bin. Elsewhere the effect is negligible.

7.4.4 Cut thresholds

The sensitivity to the cut thresholds is estimated by modifying the selection cuts and studying the effect on the measured cross section. The thresholds are varied by such an amount that the cut is still a "good" cut, i.e. the selection efficiency is still good and the number of background events does not become too large. Threshold effects are investigated for three different cuts, the photoproduction cut (C1), the good track cut (C2) and the requirement on the total number of good tracks versus the total number of tracks (C3). For each of these three sets various systematic variations are performed. The change in the cross section due to variation i is then determined as

$$\delta\sigma_i = \sigma_i \times \frac{N^i_{obs} - N^i_{bg}}{\mathcal{A}^i} \Big/ \frac{N^{nominal}_{obs} - N^{nominal}_{bg}}{\mathcal{A}^{nominal}} \tag{7.7}$$

Here N_{obs} is the number of events observed in the final charged current data sample, N_{bg} is the number of background events as expected from Monte Carlo and $\mathcal{A}$ is the acceptance. When by shifting the cut threshold the quantity $N_{obs} - N_{bg}$ in a bin changes by more than 5% or when the acceptance changes by more than 15% then $\delta\sigma_i$ is set to zero in that particular bin. This is done to separate the systematic effects of variation of cut thresholds from the effects due to the limited statistics in some of the bins. For each of the three sets C the systematic error is determined as the maximum $\delta\sigma_i$ in a bin. Thus it is possible that for example in the

$d\sigma/dy$ measurement the first bin gets its C1 systematic error from variation C1b but the last bin from C1f.

The following systematic shifts in the cut thresholds are performed:

C1: photoproduction cuts

In the first check C1a the P_T/E_T cut in the region 25 GeV $< P_T <$ 35 GeV is raised from 0.4 to 0.45. The second variation puts the cut on $P_T(-ir)/P_{T,north}(-ir)$ at 0.8 instead of 0.85. Checks C1c and C1d change the P_T/E_T cut in the P_T region below 25 GeV from 0.5 to 0.45 and 0.55, respectively. In the last two checks (C1e and C1f) the threshold that defines the lowest P_T region is changed from 25 GeV to 20 GeV and 30 GeV, respectively. The largest effect, around 4%, due to this set of variations is observed in the low Q^2 and the high y region where the largest amount of photoproduction background is expected.

C2: good track definition

Systematic effects due to a change in the definition of a good track as given in section 4.3 are only studied in the region where the hadronic angle γ_0 exceeds 0.4. The first three variations (C2a–C2c) involve the requirement on the minimum number of superlayers hit by the tracks. At least one, three or four superlayers are required to be hit which corresponds to the track polar angle ranges 11.5°–168°, 18.5°–160° and 22°–157°, respectively. Variation C2d requires a minimum transverse momentum of 0.3 GeV instead of 0.2 GeV. In the last two checks, C2e and C2f, the minimum distance of the track to the beamline is set at 1.1 cm and 2.1 cm, respectively.

The typical systematic uncertainty on the measured cross section due to these six variations C2 is less than 2%. Only in the region of low y and high x the change in the cross section is sizeable ($< 10\%$). This region is mainly populated with events where the hadronic system is very forward which means that the tracks in the CTD are found at rather low angles.

C3: total number of good tracks

The final set of variations in the cut thresholds concerns the cut on the number of good tracks compared to the total number of tracks as given in equation 4.5. These variations only affect the region $\gamma_0 > 0.4$. Equation 4.5 can be rewritten as

$$N_{good} \geq h(N_{track} - C) \tag{7.8}$$

where the slope $h = 0.25$ and $C = 20$. In systematic checks C3a and C3b the slope h is changed to 0.3 and 0.2, respectively. The constant C is decreased to 15 or increased to 25 in check C3c and C3d. The last two checks change h and C simultaneously: $h = 0.2$, $C = 15$ in check C3e and $h = 0.3$, $C = 25$ in check C3f. As can be seen from figure 4.5a these variations still reject almost no Monte Carlo data. The systematic uncertainty on the cross section arising from these variations is typically below 2%. Only in the region $x < 0.1$ it becomes of the order of 3%.

7.4.5 Background subtraction

The uncertainty in the expected photoproduction background is estimated by fitting a linear combination of the P_T/E_T distributions of the signal and the photoproduction Monte Carlo samples to the corresponding distribution in the data. During this fit the normalisations of the resolved and direct components are allowed to vary. No cut on P_T/E_T is applied for this check. A 40% uncertainty in the photoproduction background is found, leading to a sizeable error (5%) only in the lowest Q^2 bin.

7.4.6 Effect of F_L

The generator programme LEPTO that is used to simulate the hard scattering process neglects the contribution of the longitudinal structure function F_L to the charged current cross section. Calculations show, however, that for the highest y bin taking into account the contribution of F_L yields a rise of about 10% in the integrated cross section. In the unfolding of the cross sections as described in section 7.3 the cross sections σ_{rad}^{SM} and σ_{Born}^{SM} appearing in equation 7.3 have been computed with LEPTO and so they do not include F_L. On the other hand, the Standard Model cross section $d\sigma_{Born}^{SM}/dQ^2$ in equation 7.5 does include the contribution of F_L. In this way a consistent measurement of the cross section including F_L is obtained. The effect of F_L on the measurement of the cross sections can then only be due to a different acceptance.

To investigate this effect the ARIADNE Monte Carlo samples are reweighted to the electroweak Born cross section including F_L. The sensitivity to F_L is estimated by comparing the purities and the acceptances that are obtained with the full CTEQ4D cross section and the CTEQ4D cross section where F_L is set to zero. The change in the purity and the acceptance due to migration is everywhere less than 1% except in the region of high y and high Q^2. The variation in the selection efficiency is somewhat larger but still less than 2%. At low Q^2 and at high Q^2 the effect of F_L on the determination of the acceptance is smaller than $\sim 2\%$ while it is less than 0.5% at intermediate values Q^2. The acceptance as a function of x shows a change of less than 1% at low x. At high y the acceptance decreases by 2% while no change is observed for the lowest values of y.

7.4.7 Kinematics correction

The cross sections are extracted from the data using the kinematic correction of method I that has been described in the previous chapter. To investigate the sensitivity of the cross sections to the correction method they are also evaluated with method II. For the single differential cross section measurements this gives variations of the order of at most 10% in the whole kinematic range except for the highest Q^2 and x bins where a 20% effect is observed. The changes in the double differential cross section are less than 15% although in some of the bins at the edge of the kinematic plane the effect is somewhat larger.

7.4.8 Comparisons with neutral current DIS data

Neutral current data (and Monte Carlo) provide an excellent tool to study event characteristics that are possibly not well simulated in charged current Monte Carlo like vertex efficiency and

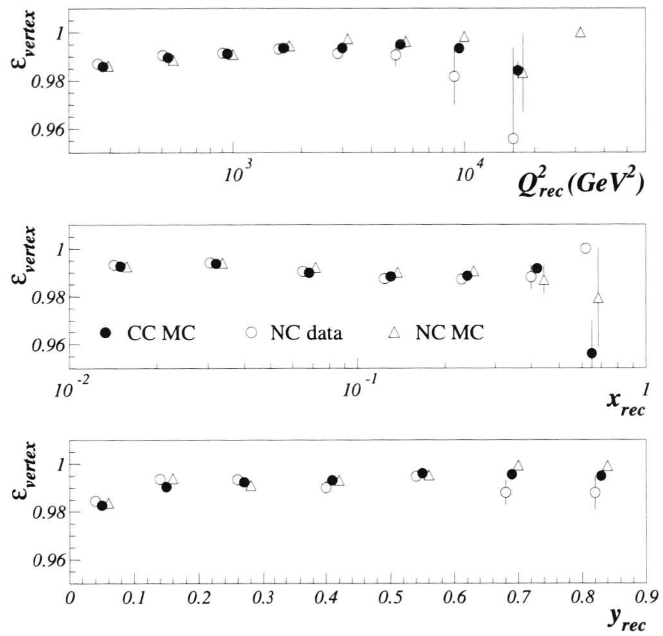

Figure 7.3: *efficiency ϵ_{vertex} with which a vertex is reconstructed as a function of the reconstructed Q^2, x and y for charged current Monte Carlo (black dots), CCfied neutral current data (circles) and CCfied neutral current Monte Carlo (triangles).*

timing. Also resolutions in kinematic quantities can be compared. It is even possible to do a complete charged current analysis on neutral current data.

Figure 7.3 shows the efficiency with which a vertex is found in the event as a function of the reconstructed kinematic quantities Q^2_{rec}, x_{rec} and y_{rec}, using the correction of method I. The black dots denote charged current Monte Carlo data, while the circles and triangles represent CCfied neutral current data and Monte Carlo, respectively. In the whole kinematic range the three sets of data agree very well. Only at high x and Q^2 the efficiencies differ but this is due to the lack of statistics in data in this region.

The efficiency with which a good track can be found in an event is displayed in figure 7.4. The three upper plots show the efficiencies in the region with hadronic angle $\gamma_0 > 0.4$ where particles go through several superlayers in the CTD, while the lower plots depict the efficiencies for the region where $\gamma_0 < 0.4$. In this latter region some difference is observed between CCfied neutral current data and both sets of Monte Carlo data. The efficiency with which a good track is found in data is slightly higher than in the Monte Carlo samples.

Since the true event kinematics are available in the CCfied neutral current samples the efficiency with which CCfied events are selected by the charged current selection criteria can be determined. These selection efficiencies should be more or less comparable both mutually

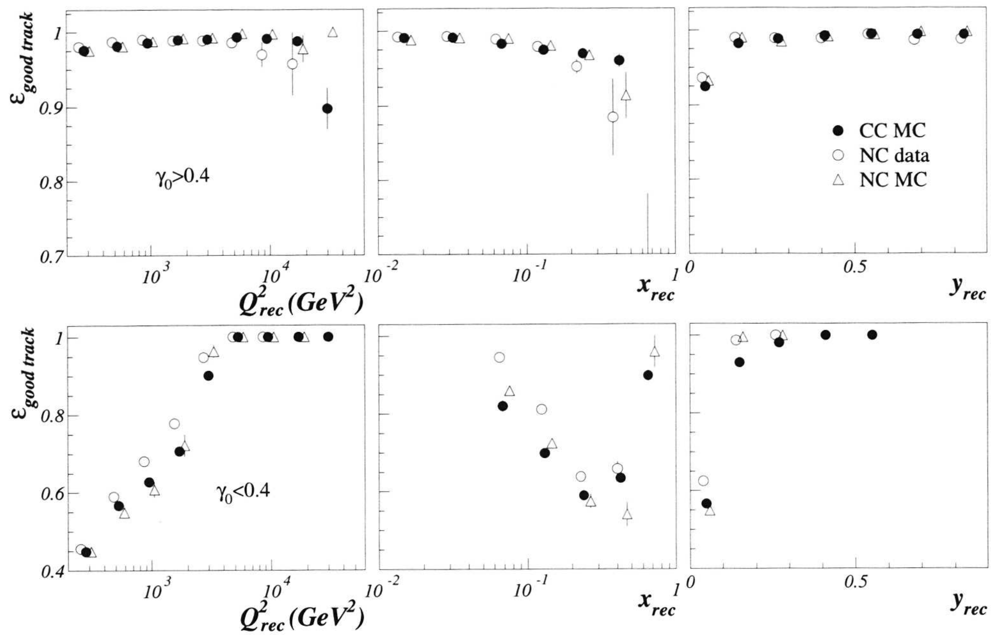

Figure 7.4: *efficiency $\epsilon_{good\ track}$ with which a good track is found in the event as a function of the reconstructed Q^2, x and y for charged current Monte Carlo (black dots), CCfied neutral current data (circles) and CCfied neutral current Monte Carlo (triangles). The upper plots show efficiencies in the region $\gamma_0 > 0.4$ while the three lower plots are for $\gamma_0 < 0.4$.*

and with the efficiencies obtained from genuine charged current Monte Carlo data. In the comparison between the selection efficiencies obtained from CCfied neutral current data and Monte Carlo the double angle kinematics are taken as the true ones. Also a Q^2 value of at least 300 GeV^2 is required as explained in section 6.4. The selection efficiencies computed in the bins used for the measurement of the single differential cross sections agree within 10%. In the (x, Q^2) bins the agreement is also within 10% except in the low y region where a difference of at most 20% is observed.

In the same way the selection efficiencies computed from genuine charged current and CCfied neutral current Monte Carlo data can be compared. Typically these efficiencies agree within 20% although at high y the difference tends to be larger but still less than 30%.

7.4.9 Summary of systematic checks

The systematic uncertainties on the measured cross sections are added in quadrature, separately for the positive and the negative deviations from the nominal cross section values. The results of each systematic check are summarised in tables 7.1 and 7.2. Figure 7.5 shows the relative systematic error for a couple of checks in each (x, Q^2) bin. The lower two plots show the total relative systematic and statistical error. They are quite comparable in size except in the highest x and highest Q^2 bins where the statistical error dominates. An additional overall normalisation error of 1.6%, arising from the uncertainty in the luminosity measurement, is not included in the systematic errors.

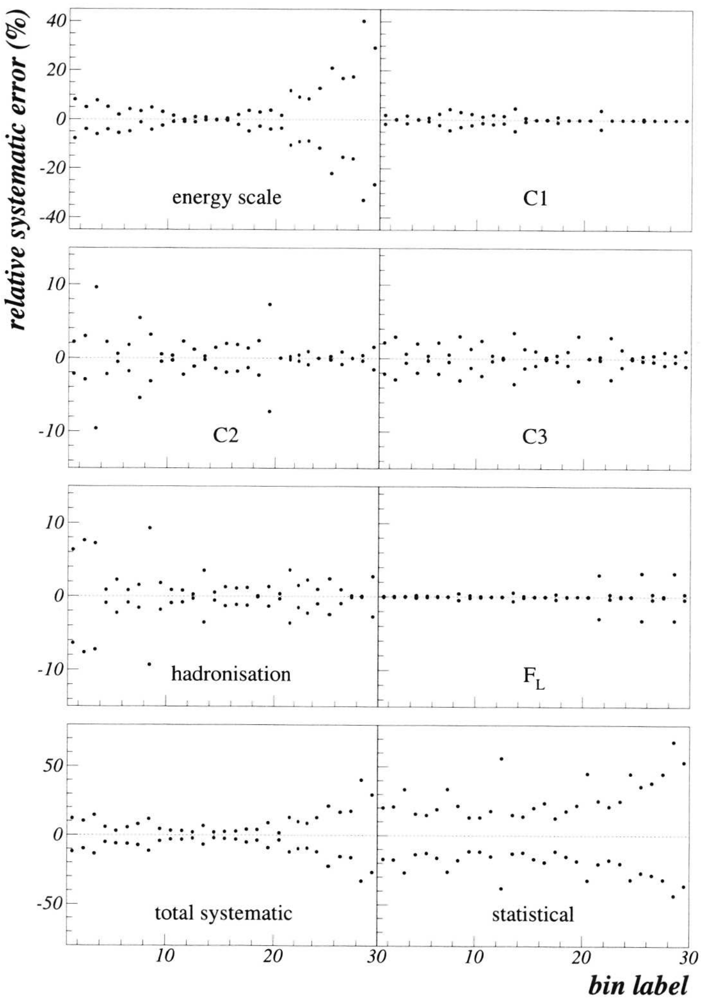

Figure 7.5: *relative systematic errors on the double differential cross section $d\sigma/dxdQ^2$ for various checks as a function of the bin label as defined in figure 7.1. The total systematic and statistical error in each bin are given in the lower two plots.*

		acceptances				number of events							systematic errors in %							
Q^2_{min} (GeV^2)	Q^2_{max} (GeV^2)	$\mathcal{P}$	ϵ_{sel}	ϵ_{mig}	$\mathcal{A}$	N_{obs}	PHP direct	PHP resolved	W	$\mu\mu$	$\tau\tau$	total	E scale	MEPS	$C1$	$C2$	$C3$	PHP	δF_L	total
200	400	0.65	0.42	1.11	0.47	133	4.32	9.63	0.53	6.84	2.82	24.15	$^{+7.4}_{-6.1}$	±7.9	±3.8	±1.9	±1.5	±5.1	-1.35	$^{+12.8}_{-12.2}$
400	711	0.62	0.60	1.03	0.62	185	0.39	2.14	0.74	2.20	1.39	6.86	$^{+3.8}_{-4.8}$	±2.0	±2.0	±1.3	±1.1	±0.6	-0.96	$^{+5.1}_{-5.9}$
711	1265	0.65	0.69	1.01	0.70	228	0.	0.	0.92	0.51	0.36	1.79	$^{+2.3}_{-1.8}$	±2.7	±1.0	±0.9	±0.9	0.	-0.68	$^{+3.9}_{-3.7}$
1265	2249	0.67	0.76	1.00	0.76	193	0.	0.	1.12	0.34	0.17	1.63	$^{+0.4}_{-0.2}$	±1.7	±2.3	±0.8	±1.9	0.	-0.60	$^{+3.5}_{-3.6}$
2249	4000	0.69	0.81	0.99	0.81	170	0.39	0.	0.75	0.32	0.11	1.57	$^{+3.4}_{-4.2}$	0.	±1.0	±1.1	±0.3	0.1	-0.58	$^{+3.8}_{-4.5}$
4000	7113	0.69	0.83	0.99	0.83	88	0.	0.	0.32	0.	0.	0.32	$^{+10.1}_{-9.7}$	±0.9	±0.9	±1.2	±0.9	0.	-0.54	$^{+10.3}_{-9.9}$
7113	12649	0.66	0.82	1.01	0.83	36	0.	0.	0.095	0.	0.	0.095	$^{+18.8}_{-18.4}$	±1.6	±2.3	±1.3	±2.1	0.	-0.58	$^{+19.2}_{-18.7}$
12649	22494	0.59	0.80	1.04	0.83	13	0.	0.	0.035	0.	0.	0.035	$^{+37.2}_{-30.5}$	±0.6	0.	±1.1	±0.7	0.	-0.79	$^{+37.3}_{-30.6}$
22494	60000	0.42	0.75	1.37	1.03	1	0.	0.	0.0035	0.	0.	0.0035	$^{+71.6}_{-46.8}$	±2.0	—	±0.5	±0.8	0.	-1.31	$^{+71.6}_{-46.9}$
> 200		0.98	0.67	1.02	0.68	1047	5.11	11.8	4.51	10.2	4.85	36.45	$^{+0.6}_{-0.4}$	±2.0	±1.2	±0.6	±1.1	0.7	-0.77	$^{+2.6}_{-2.7}$

x_{min}	x_{max}																			
0.01	0.0215	0.69	0.55	1.05	0.57	130	1.57	3.21	0.43	0.66	1.13	7.00	$^{+6.1}_{-5.2}$	±5.3	±0.5	±2.3	±3.0	±1.6	-0.99	$^{+9.1}_{-8.5}$
0.0215	0.0464	0.75	0.73	1.04	0.76	237	0.79	1.07	0.87	0.98	0.90	4.62	$^{+1.8}_{-2.1}$	±3.4	±1.6	±0.4	±1.5	±0.3	-0.53	$^{+4.5}_{-4.6}$
0.0464	0.1	0.82	0.84	1.00	0.84	304	0.39	0.	1.56	4.02	1.20	7.18	$^{+0.4}_{-0.5}$	±0.2	±1.9	±1.2	±0.9	±0.1	-0.21	$^{+2.4}_{-2.4}$
0.1	0.178	0.82	0.80	0.98	0.79	190	0.	0.	1.02	3.54	0.40	4.95	$^{+3.9}_{-3.7}$	±0.1	±0.6	±1.0	±0.7	0.	-0.05	$^{+4.2}_{-4.0}$
0.178	0.316	0.86	0.66	0.95	0.62	106	0.39	0.	0.45	0.42	0.057	1.31	$^{+7.8}_{-7.5}$	±0.7	±0.2	±1.8	±1.2	±0.2	0.04	$^{+8.1}_{-7.9}$
0.316	0.562	0.89	0.53	0.92	0.49	36	0.	0.	0.058	0.11	0.054	0.22	$^{+13.3}_{-12.0}$	±0.4	0.	—	±0.4	0.	0.04	$^{+13.3}_{-12.1}$
0.562	1.	0.81	0.46	0.86	0.39	3	0.	0.	0.	0.	0.	0.	$^{+37.0}_{-28.2}$	±0.5	—	—	±0.2	0.	0.04	$^{+37.0}_{-28.2}$

y_{min}	y_{max}																			
0.	0.1	0.91	0.57	0.94	0.54	156	1.18	0.	0.83	8.09	1.91	12.01	$^{+2.6}_{-2.3}$	±1.4	±1.5	±1.8	±1.2	±0.3	0.01	$^{+4.1}_{-3.8}$
0.1	0.2	0.84	0.87	0.98	0.85	247	0.79	1.07	1.14	0.89	0.48	4.37	$^{+0.8}_{-0.9}$	±1.8	±1.3	±0.9	±1.0	±0.3	0.01	$^{+2.8}_{-2.8}$
0.2	0.34	0.81	0.83	1.00	0.84	242	1.97	4.28	1.00	0.41	0.95	8.61	$^{+0.2}_{-0.1}$	±2.1	±1.8	±1.0	±1.1	±1.1	-0.02	$^{+3.3}_{-3.3}$
0.34	0.48	0.74	0.78	1.02	0.80	183	0.39	2.14	0.79	0.32	0.32	3.97	$^{+0.7}_{-0.9}$	±2.1	±2.0	±1.6	±1.5	±0.6	-0.11	$^{+3.7}_{-3.8}$
0.48	0.62	0.67	0.69	1.04	0.72	113	0.39	2.14	0.38	0.24	0.68	3.84	$^{+2.2}_{-1.9}$	±1.8	±4.8	±0.3	±1.7	±0.9	-0.37	$^{+5.9}_{-5.8}$
0.62	0.76	0.62	0.58	1.01	0.59	61	0.39	2.14	0.26	0.16	0.34	3.30	$^{+5.0}_{-3.9}$	±3.8	±5.2	±0.2	±3.2	±1.7	-0.94	$^{+9.0}_{-8.4}$
0.76	0.9	0.57	0.33	1.29	0.42	45	0.	0.	0.10	0.080	0.17	0.35	$^{+9.2}_{-10.6}$	±4.3	±1.3	±0.1	±0.2	0.	-1.99	$^{+10.2}_{-11.7}$

Table 7.1: *acceptance, expected background and systematic errors in intervals of Q^2, x and y for the range $Q^2 > 200$ GeV^2. The symbols in the heading are explained in the text.*

		acceptances				number of events							systematic errors in %							
Q_c^2 (GeV^2)	x_c	$\mathcal{P}$	ϵ_{sel}	ϵ_{mig}	$\mathcal{A}$	N_{obs}	PHP direct	PHP resolved	W	$\mu\mu$	$\tau\tau$	total	E scale	MEPS	$C1$	$C2$	$C3$	PHP	δF_L	total
280	0.015	0.52	0.57	1.13	0.64	43	1.57	3.21	0.14	0.42	0.61	5.96	$^{+8.1}_{-7.7}$	±6.4	±1.8	±2.2	±2.1	±5.2	0.	$^{+12.1}_{-11.8}$
280	0.032	0.55	0.68	1.17	0.80	38	0.79	1.07	0.15	0.83	0.51	3.35	$^{+5.0}_{-4.0}$	±7.6	±0.1	±2.9	±2.9	±2.1	0.03	$^{+10.2}_{-9.8}$
280	0.068	0.59	0.61	1.06	0.65	21	0.	0.	0.10	3.20	0.77	4.08	$^{+7.6}_{-6.1}$	±7.2	±1.9	±9.6	±0.6	0.	0.02	$^{+14.4}_{-13.6}$
530	0.015	0.45	0.62	1.08	0.66	52	0.	0.	0.18	0.16	0.35	0.69	$^{+5.0}_{-4.1}$	±0.9	±0.1	±2.2	±2.0	0.	−0.17	$^{+5.9}_{-5.2}$
530	0.032	0.54	0.80	1.05	0.84	60	0.	0.	0.21	0.16	0.17	0.53	$^{+2.0}_{-5.5}$	±2.3	±0.7	±0.6	±0.3	0.	0.01	$^{+3.1}_{-6.1}$
530	0.068	0.61	0.87	0.98	0.85	40	0.	0.	0.20	0.57	0.23	1.01	$^{+4.1}_{-4.9}$	±0.9	±3.0	±1.8	±2.1	0.	0.01	$^{+5.6}_{-6.2}$
530	0.13	0.58	0.62	0.96	0.59	17	0.	0.	0.10	1.15	0.18	1.43	$^{+3.4}_{-1.2}$	±1.6	±5.0	±5.5	±0.5	0.	0.	$^{+7.9}_{-7.3}$
950	0.015	0.39	0.46	1.09	0.50	30	0.	0.	0.10	0.080	0.17	0.35	$^{+4.8}_{-4.2}$	±9.3	±3.1	±3.2	±3.0	0.	−1.42	$^{+11.7}_{-11.5}$
950	0.032	0.54	0.80	1.03	0.83	73	0.	0.	0.25	0.	0.054	0.31	$^{+3.1}_{-2.5}$	±1.8	±2.3	±0.5	±1.3	0.	−0.02	$^{+4.5}_{-4.1}$
950	0.068	0.63	0.90	0.98	0.88	74	0.	0.	0.30	0.16	0.14	0.60	$^{+1.6}_{-0.9}$	±0.9	±1.3	±0.3	±2.4	0.	0.01	$^{+3.3}_{-3.0}$
950	0.13	0.65	0.84	0.97	0.82	44	0.	0.	0.20	0.079	0.	0.28	$^{+0.0}_{-0.9}$	±0.8	±1.8	±2.3	±0.4	0.	0.	$^{+3.1}_{-3.2}$
950	0.24	0.61	0.38	0.84	0.32	7	0.	0.	0.065	0.18	0.	0.25	$^{+1.0}_{-1.1}$	±0.3	±1.9	±1.2	±0.1	0.	0.	$^{+2.2}_{-2.2}$
1700	0.032	0.49	0.70	1.04	0.73	57	0.	0.	0.22	0.	0.11	0.34	$^{+1.0}_{-0.3}$	±3.5	±4.7	±0.2	±3.5	0.	−0.68	$^{+6.9}_{-6.8}$
1700	0.068	0.61	0.92	1.01	0.93	67	0.	0.	0.45	0.	0.058	0.51	$^{+0.0}_{-0.3}$	±0.5	±0.8	±1.4	±1.3	0.	0.	$^{+2.2}_{-2.2}$
1700	0.13	0.67	0.91	0.98	0.89	35	0.	0.	0.30	0.	0.	0.30	$^{+0.5}_{-0.4}$	±1.3	0.	±1.9	±1.0	0.	0.	$^{+2.6}_{-2.6}$
1700	0.24	0.69	0.71	0.90	0.64	27	0.	0.	0.13	0.23	0.	0.36	$^{+1.9}_{-2.1}$	±1.1	±0.1	±1.8	±0.2	0.	0.	$^{+2.9}_{-3.0}$
3000	0.068	0.58	0.88	1.02	0.90	78	0.39	0.	0.38	0.079	0.	0.85	$^{+3.6}_{-4.7}$	±1.2	±1.1	±1.3	±0.4	±0.2	−0.20	$^{+4.2}_{-5.2}$
3000	0.13	0.67	0.93	0.98	0.91	44	0.	0.	0.22	0.24	0.	0.46	$^{+3.0}_{-2.8}$	±0.1	0.	±2.3	±0.9	0.	0.	$^{+3.9}_{-3.8}$
3000	0.24	0.72	0.90	0.94	0.84	30	0.	0.	0.10	0.	0.	0.10	$^{+3.8}_{-4.0}$	±1.3	—	±7.3	±3.0	0.	0.	$^{+8.9}_{-8.9}$
3000	0.42	0.76	0.77	0.88	0.68	9	0.	0.	0.016	0.	0.054	0.070	$^{+1.7}_{-3.6}$	±0.3	—	—	0.	0.	0.	$^{+1.8}_{-3.6}$
5300	0.068	0.43	0.66	1.01	0.67	23	0.	0.	0.12	0.	0.	0.12	$^{+11.7}_{-10.5}$	±3.6	±3.9	±0.2	±0.2	0.	−1.03	$^{+12.9}_{-12.1}$
5300	0.13	0.61	0.92	1.00	0.93	32	0.	0.	0.12	0.	0.	0.12	$^{+9.2}_{-9.1}$	±1.5	0.	±0.4	±2.9	0.	−0.07	$^{+9.8}_{-9.7}$
5300	0.24	0.70	0.92	0.98	0.90	24	0.	0.	0.064	0.	0.	0.064	$^{+8.3}_{-8.8}$	±2.2	—	±0.9	±1.2	0.	−0.01	$^{+8.7}_{-9.2}$
5300	0.42	0.73	0.92	0.93	0.86	9	0.	0.	0.013	0.	0.	0.013	$^{+12.7}_{-11.7}$	±1.0	—	—	±0.1	0.	0.	$^{+12.8}_{-11.8}$
9500	0.13	0.45	0.77	1.02	0.79	13	0.	0.	0.043	0.	0.	0.043	$^{+21.0}_{-22.1}$	±2.4	±0.3	±0.3	±0.3	0.	−0.67	$^{+21.2}_{-22.5}$
9500	0.24	0.64	0.92	1.02	0.94	12	0.	0.	0.046	0.	0.	0.046	$^{+16.7}_{-15.4}$	±0.9	—	±0.8	±0.4	0.	−0.05	$^{+16.8}_{-15.4}$
9500	0.42	0.72	0.92	0.97	0.89	9	0.	0.	0.003	0.	0.	0.003	$^{+17.4}_{-16.1}$	±0.1	—	—	±0.9	0.	0.	$^{+17.5}_{-16.1}$
17000	0.24	0.45	0.80	1.05	0.84	5	0.	0.	0.022	0.	0.	0.022	$^{+40.1}_{-32.7}$	±0.1	0.	±0.4	±0.5	0.	−0.71	$^{+40.1}_{-33.1}$
17000	0.42	0.63	0.92	1.07	0.99	7	0.	0.	0.013	0.	0.	0.013	$^{+29.3}_{-26.5}$	±2.7	—	±1.5	±1.0	0.	−0.04	$^{+29.5}_{-26.7}$

Table 7.2: *acceptance, expected background and systematic errors in (x, Q^2) bins. The symbols in the heading are explained in the text.*

7.5 Integrated cross section

The integrated e^+p charged current DIS cross section is measured in the Q^2 region above 200 GeV^2. In the last row of table 7.3 the results of this measurement are summarised. The cross section is found to be

$$\sigma_{CC}(Q^2 > 200 \text{ GeV}^2) = 32.06 \pm 1.0(\text{stat})^{+0.91}_{-0.90}(\text{syst}) \text{ pb} \tag{7.9}$$

where the first error is statistical and the second error is the total systematic error excluding the overall normalisation uncertainty of 1.6%. This result is in good agreement with the Standard Model prediction of 31.64 pb evaluated with the CTEQ4D parton density distributions. Note that with the current amount of data the statistical and systematic error have approximately the same size. Thus, after the luminosity upgrade the latter error is likely to become the dominant one. Currently the largest contribution to the systematic error is due to the uncertainty in the parton shower development as discussed in section 7.4.2.

7.6 Measurement of $d\sigma/dQ^2$

In table 7.3 the results of the measurement of the single differential cross section $d\sigma/dQ^2$ are summarised. The cross section is plotted in figure 7.6a together with the prediction of the CTEQ4D parametrisation, drawn as a solid line. Statistical errors on the points are indicated

Q^2 range (GeV^2)	Q^2_c (GeV^2)	N_{obs}	N_{bg}	$\mathcal{A}$	$\mathcal{C}_{rad}$	$d\sigma/dQ^2$ (pb/GeV^2) measured	$d\sigma/dQ^2$ (pb/GeV^2) SM
200 – 400	280	133	24.15	0.47	1.01	$2.53 \pm 0.29\ ^{+0.32}_{-0.31} \cdot 10^{-2}$	$2.79 \cdot 10^{-2}$
400 – 711	530	185	6.86	0.62	1.01	$2.00 \pm 0.16\ ^{+0.10}_{-0.12} \cdot 10^{-2}$	$1.87 \cdot 10^{-2}$
711 – 1265	950	228	1.79	0.70	1.01	$1.27 \pm 0.09\ ^{+0.05}_{-0.05} \cdot 10^{-2}$	$1.15 \cdot 10^{-2}$
1265 – 2249	1700	193	1.63	0.76	1.02	$5.60 \pm 0.41\ ^{+0.20}_{-0.20} \cdot 10^{-3}$	$6.11 \cdot 10^{-3}$
2249 – 4000	3000	170	1.57	0.81	1.04	$2.66 \pm 0.21\ ^{+0.10}_{-0.12} \cdot 10^{-3}$	$2.64 \cdot 10^{-3}$
4000 – 7113	5300	88	0.32	0.83	1.05	$7.67\ ^{+0.91}_{-0.82}\ ^{+0.79}_{-0.76} \cdot 10^{-4}$	$8.43 \cdot 10^{-4}$
7113 – 12649	9500	36	0.095	0.83	1.06	$1.69\ ^{+0.33}_{-0.28}\ ^{+0.33}_{-0.32} \cdot 10^{-4}$	$1.71 \cdot 10^{-4}$
12649 – 22494	17000	13	0.035	0.83	1.07	$3.08\ ^{+1.11}_{-0.84}\ ^{+1.15}_{-0.94} \cdot 10^{-5}$	$1.80 \cdot 10^{-5}$
22494 – 60000	30000	1	0.0035	1.03	1.08	$8.64\ ^{+19.9}_{-7.18}\ ^{+6.19}_{-4.05} \cdot 10^{-7}$	$6.77 \cdot 10^{-7}$
> 200		1047	36.45	0.68	1.04	$32.06 \pm 1.0\ ^{+0.91}_{-0.90}$ pb	31.64 pb

Table 7.3: *the differential cross section $d\sigma/dQ^2$ measured in bins of Q^2. The symbols in the heading are explained in the text.*

by the inner errors bars (delimited by horizontal lines) while the full error bars show the total error obtained by adding the statistical and systematic contributions in quadrature. In figure 7.6b the ratio of the measured cross section to the Standard Model cross section evaluated with the CTEQ4D PDFs is shown. The shaded band indicates the uncertainty on the Standard Model prediction. Also shown by a full line is the result of the QCD fit. Note that this fit does not include the measurements of the charged current cross sections presented in this thesis.

Over five orders of magnitude the Standard Model prediction is able to describe the measured cross section. The NLO QCD fit shows a rise in the cross section at high Q^2 compared to the CTEQ4D prediction. However, the error on this prediction is rather large, mainly due to the uncertainty in the d quark density. A considerable reduction in this uncertainty is only reachable if the statistics of the data at high Q^2 are increased considerably. However, also the energy scale of the calorimeter has to be understood better as the uncertainty in this scale yields a systematic error of $\sim 70\%$ in the largest Q^2 bin.

7.7 Measurement of $d\sigma/dx$

The measurement of the cross section $d\sigma/dx$ in the region $Q^2 > 200$ GeV^2 is summarised in table 7.4. In figure 7.7a the cross section is plotted as a function of x, while figure 7.7b displays the ratio of the measured cross section to the Standard Model prediction evaluated using the CTEQ4D parton density functions. At the lower end of the x range the cross section is largest and has a gradual decrease from $x = 0.01$ to 0.2 followed by a sharp drop towards $x = 0.7$. At high x the cross section shows a tendency to be above the CTEQ4D prediction. However, no stronger conclusions can be drawn from this observation since the uncertainty on the predicted cross section is rapidly growing beyond $x = 0.4$.

The NLO QCD fit also describes the data and even follows the trends observed in the data: at intermediate x it undershoots the CTEQ4D prediction, just like the data and it shows a strong rise towards higher x. The latter is because the fit yields a larger d/u quark distribution at high x than CTEQ4D. An artificial modification of the d density according to equation 1.33, as suggested in [28], yields a $d\sigma/dx$ very close to the NLO QCD fit at high x. The MRST set of parton momentum distributions, which includes the E866 measurement of $x(\bar{d} - \bar{u})$ that (partially) drives the d/u ratio at high x, also predicts a larger cross section in this region.

7.8 Measurement of $d\sigma/dy$

The measurement of the single differential cross section $d\sigma/dy$ in the Q^2 region above 200 GeV^2 is compiled in table 7.5. The cross section is plotted in figure 7.8a together with the Standard Model prediction computed using the CTEQ4D set of parton densities. At low y the cross section is largest and decreases slowly as a function of y for $y > 0.1$. The data do not allow a measurement of the steeply falling cross section towards lower y. Figure 7.8b shows the ratio of the measured cross section to the Standard Model prediction. The shaded band is the error on this prediction originating from the uncertainty on the PDFs. Also drawn is the prediction of the NLO QCD fit that shows a sharp rise towards low y. Note that at high y the cross section is dominated by the sea quark distribution $x(\bar{u} + \bar{c})$ as expected from helicity conservation.

x range	x_c	N_{obs}	N_{bg}	$\mathcal{A}$	$\mathcal{C}_{rad}$	$d\sigma/dx$ (pb)	
						measured	SM
0.01 – 0.0215	0.015	130	7.00	0.57	1.03	$416 \pm 40\ ^{+38}_{-56}$	398
0.0215 – 0.0464	0.032	237	4.62	0.76	1.02	$271 \pm 18\ ^{+12}_{-13}$	277
0.0464 – 0.1	0.068	304	7.18	0.84	1.01	$146 \pm 8.7\ ^{+3.5}_{-3.6}$	152
0.1 – 0.178	0.13	190	4.95	0.79	1.01	$67.6 \pm 5.1\ ^{+2.8}_{-2.7}$	71.2
0.178 – 0.316	0.24	106	1.31	0.62	1.01	$25.7 \pm 2.5\ ^{+2.1}_{-2.0}$	24.2
0.316 – 0.562	0.42	36	0.22	0.49	1.01	$6.12\ ^{+1.21}_{-1.02}\ ^{+0.81}_{-0.74}$	4.60
0.562 – 1	0.65	3	0.	0.39	1.01	$0.74\ ^{+0.72}_{-0.40}\ ^{+0.27}_{-0.21}$	0.37

Table 7.4: *the differential cross section $d\sigma/dx$ measured in bins of x for $Q^2 > 200$ GeV^2. The symbols in the heading are explained in the text.*

y range	y_c	N_{obs}	N_{bg}	$\mathcal{A}$	$\mathcal{C}_{rad}$	$d\sigma/dy$ (pb)	
						measured	SM
0. – 0.1	0.05	156	12.01	0.54	0.98	$65.0 \pm 5.8\ ^{+2.6}_{-2.5}$	69.4
0.1 – 0.2	0.15	247	4.37	0.85	0.99	$59.8 \pm 3.9\ ^{+1.6}_{-1.7}$	58.3
0.2 – 0.34	0.27	242	8.61	0.84	1.01	$42.1 \pm 2.9\ ^{+1.4}_{-1.4}$	43.2
0.34 – 0.48	0.41	183	3.97	0.80	1.03	$34.5 \pm 2.6\ ^{+1.3}_{-1.3}$	31.2
0.48 – 0.62	0.55	113	3.84	0.72	1.05	$23.9 \pm 2.4\ ^{+1.4}_{-1.4}$	23.5
0.62 – 0.76	0.69	61	3.30	0.59	1.07	$15.7\ ^{+2.4}_{-2.1}\ ^{+1.4}_{-1.3}$	18.5
0.76 – 0.9	0.83	45	0.35	0.42	1.10	$17.5\ ^{+3.0}_{-2.6}\ ^{+1.8}_{-2.0}$	15.4

Table 7.5: *the differential cross section $d\sigma/dy$ measured in bins of y for $Q^2 > 200$ GeV^2. The symbols in the heading are explained in the text.*

7.9 Measurement of $d\sigma/dxdQ^2$

With the current amount of data it is possible to perfom a first HERA measurement of the charged current double differential cross section $d\sigma/dxdQ^2$. Still the uncertainty in the measurement is largely dominated by the statistical error. The double differential cross sections, or rather, the reduced cross sections are tabulated in tables 7.6a and 7.6b. The reduced double differential cross section $\tilde{\sigma}$ is defined as

$$\tilde{\sigma} = \left[\frac{G_F^2}{2\pi x}\left(\frac{M_W^2}{Q^2+M_W^2}\right)^2\right]^{-1}\frac{d\sigma^{CC}}{dx\,dQ^2} \tag{7.10}$$

$$= \frac{1}{2}\left[Y_+\,W_2^+(x,Q^2) - Y_-\,W_3^+(x,Q^2) - y^2\,W_L^+(x,Q^2)\right] \tag{7.11}$$

The reduced cross sections are displayed as a function of x and Q^2 in figures 7.9 and 7.10, respectively. The Standard Model predictions evaluated using the CTEQ4D parton momentum distributions give a good description of the data, although at high x there is again a tendency for the measured cross section to lie above the CTEQ4D predictions. The predictions of the NLO QCD fit at high x are somewhat higher than those obtained with CTEQ4D.

In leading order QCD the reduced cross section depends on the quark momentum distributions as follows:

$$\tilde{\sigma} = x\left[\bar{u}+\bar{c}+(1-y)^2(d+s)\right] \tag{7.12}$$

As a result, for fixed Q^2, $\tilde{\sigma}$ at low x, i.e. high y, is mainly sensitive to the antiquark combination $\bar{u}+\bar{c}$ while at high x, i.e. low y, it is dominated by the quark combination $d+s$. In figure 7.10 the contributions of both $x(\bar{u}+\bar{c})$ and $(1-y)^2\,x(d+s)$ to the cross section are drawn as a function of x. These combinations of parton densities are evaluated with the leading order QCD CTEQ4L parametrisation. The data clearly demonstrate the presence of both components. Both the quark and the antiquark combinations are required to obtain a good description of the data.

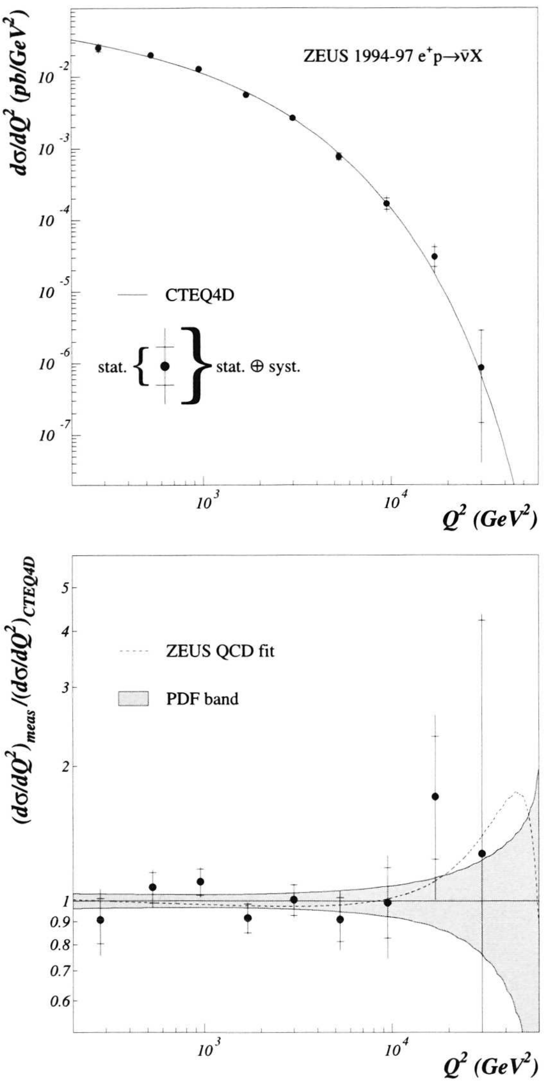

Figure 7.6: *(a) the measured e^+p CC DIS Born cross section $d\sigma/dQ^2$ (dots) compared to the Standard Model prediction evaluated using the CTEQ4D PDFs. (b) The ratio of the measured cross section and the prediction. The statistical errors are indicated by the inner error bars (delimited by horizontal lines) while the full error bars show the statistical and systematic error added in quadrature. The shaded band shows the uncertainty in the prediction originating from the PDFs. Also shown by a dashed line is the result of the QCD fit.*

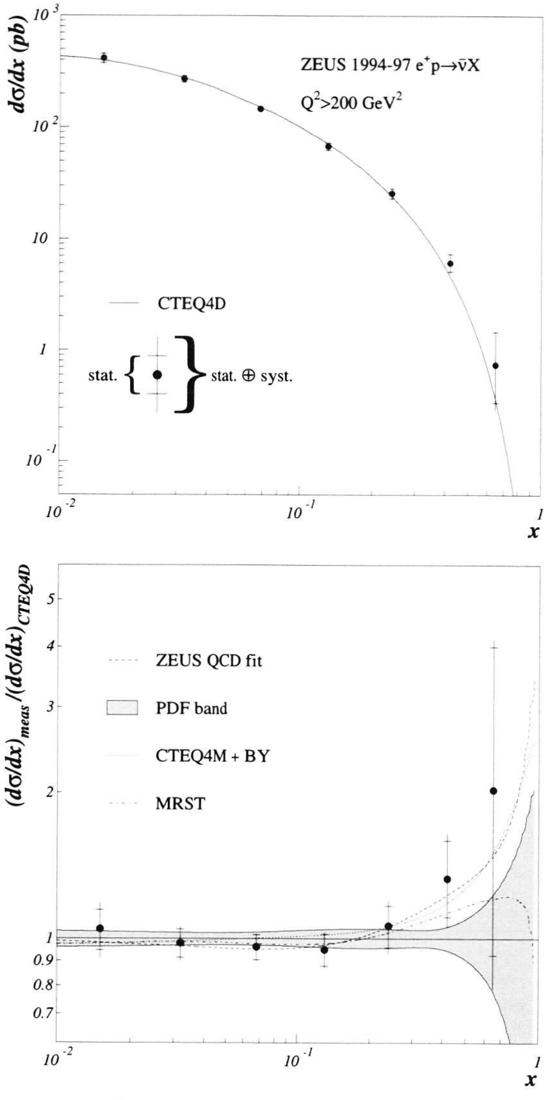

Figure 7.7: *(a) the measured e^+p CC DIS Born cross section $d\sigma/dx$ (dots) compared to the Standard Model prediction evaluated using the CTEQ4D PDFs. (b) The ratio of the measured cross section to the prediction. The statistical errors are indicated by the inner error bars (delimited by horizontal lines) while the full error bars show the statistical and systematic error added in quadrature. The shaded band shows the PDF uncertainty on the prediction. Also shown by a dashed line is the result of the QCD fit. The dotted line represents the result of modifying the d density by adding a term $0.1(x + 1)xu$. The dot-dashed line shows the prediction from the MRST set of PDFs.*

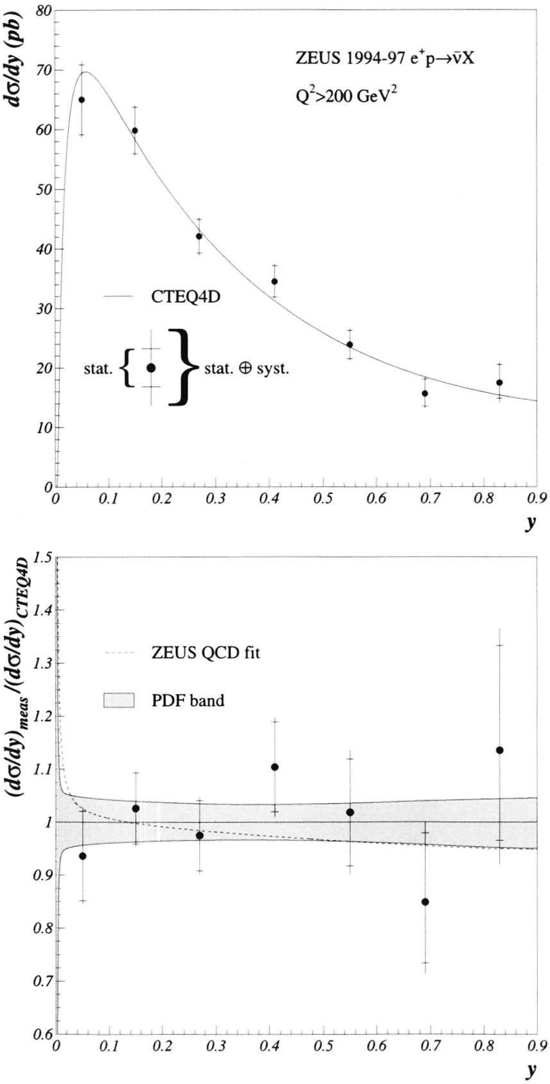

Figure 7.8: *(a) the measured e^+p CC DIS Born cross section $d\sigma/dy$ (dots) compared to the Standard Model prediction evaluated using the CTEQ4D PDFs. (b) The ratio of the measured cross section and the prediction. The statistical errors are indicated by the inner error bars (delimited by horizontal lines) while the full error bars show the statistical and systematic error added in quadrature. The shaded band shows the uncertainty in the prediction originating from the PDFs. Also shown by a dashed line is the result of the QCD fit.*

Q^2 range (GeV^2)	x range	Q^2_c (GeV^2)	x_c	N_{obs}	N_{bg}	$\mathcal{A}$	$\mathcal{C}_{rad}$	$\tilde{\sigma}$ measured	$\tilde{\sigma}$ SM
200 – 400	0.01 – 0.0215	280	0.015	43	5.96	0.64	1.00	$1.04\ ^{+0.21}_{-0.18}\ ^{+0.13}_{-0.12}$	1.03
200 – 400	0.0215 – 0.0464	280	0.032	38	3.35	0.80	0.99	$0.77\ ^{+0.16}_{-0.14}\ ^{+0.08}_{-0.08}$	0.86
200 – 400	0.0464 – 0.1	280	0.068	21	4.08	0.65	0.97	$0.45\ ^{+0.15}_{-0.12}\ ^{+0.07}_{-0.06}$	0.66
400 – 711	0.01 – 0.0215	530	0.015	52	0.69	0.66	1.02	$1.00\ ^{+0.16}_{-0.14}\ ^{+0.06}_{-0.05}$	0.86
400 – 711	0.0215 – 0.0464	530	0.032	60	0.53	0.84	0.99	$0.87\ ^{+0.13}_{-0.11}\ ^{+0.03}_{-0.05}$	0.79
400 – 711	0.0464 – 0.1	530	0.068	40	1.01	0.85	0.98	$0.55\ ^{+0.11}_{-0.09}\ ^{+0.03}_{-0.04}$	0.63
400 – 711	0.1 – 0.178	530	0.13	17	1.43	0.59	0.98	$0.44\ ^{+0.15}_{-0.11}\ ^{+0.04}_{-0.03}$	0.44
711 – 1265	0.01 – 0.0215	950	0.015	30	0.35	0.50	1.06	$0.56\ ^{+0.12}_{-0.10}\ ^{+0.07}_{-0.07}$	0.64
711 – 1265	0.0215 – 0.0464	950	0.032	73	0.31	0.83	1.01	$0.71\ ^{+0.09}_{-0.08}\ ^{+0.03}_{-0.03}$	0.66
711 – 1265	0.0464 – 0.1	950	0.068	74	0.60	0.88	0.99	$0.65\ ^{+0.09}_{-0.08}\ ^{+0.02}_{-0.02}$	0.57
711 – 1265	0.1 – 0.178	950	0.13	44	0.28	0.82	0.98	$0.56\ ^{+0.10}_{-0.08}\ ^{+0.02}_{-0.02}$	0.41
711 – 1265	0.178 – 0.316	950	0.24	7	0.25	0.32	0.99	$0.22\ ^{+0.12}_{-0.08}\ ^{+0.01}_{-0.01}$	0.22
1265 – 2249	0.0215 – 0.0464	1700	0.032	57	0.34	0.73	1.05	$0.44\ ^{+0.07}_{-0.06}\ ^{+0.03}_{-0.03}$	0.48
1265 – 2249	0.0464 – 0.1	1700	0.068	67	0.51	0.93	1.02	$0.40\ ^{+0.05}_{-0.05}\ ^{+0.01}_{-0.01}$	0.47
1265 – 2249	0.1 – 0.178	1700	0.13	35	0.30	0.89	1.00	$0.28\ ^{+0.06}_{-0.05}\ ^{+0.01}_{-0.01}$	0.36

Table 7.6a: *the reduced cross section $\tilde{\sigma}$ as defined in equation 7.10 measured in (x, Q^2) bins. The symbols in the heading are explained in the text.*

Q^2 range (GeV^2)	x range	Q^2_c (GeV^2)	x_c	N_{obs}	N_{bg}	$\mathcal{A}$	$\mathcal{C}_{rad}$	$\tilde{\sigma}$ measured	$\tilde{\sigma}$ SM
1265 – 2249	0.178 – 0.316	1700	0.24	27	0.36	0.64	0.99	$0.29\ ^{+0.07}_{-0.06}\ ^{+0.01}_{-0.01}$	0.20
2249 – 4000	0.0464 – 0.1	3000	0.068	78	0.85	0.90	1.06	$0.38\ ^{+0.05}_{-0.04}\ ^{+0.02}_{-0.02}$	0.34
2249 – 4000	0.1 – 0.178	3000	0.13	44	0.46	0.91	1.03	$0.27\ ^{+0.05}_{-0.04}\ ^{+0.01}_{-0.01}$	0.29
2249 – 4000	0.178 – 0.316	3000	0.24	30	0.10	0.84	1.01	$0.19\ ^{+0.04}_{-0.04}\ ^{+0.02}_{-0.02}$	0.17
2249 – 4000	0.316 – 0.562	3000	0.42	9	0.070	0.68	1.00	$0.068\ ^{+0.031}_{-0.022}\ ^{+0.001}_{-0.002}$	0.054
4000 – 7113	0.0464 – 0.1	5300	0.068	23	0.12	0.67	1.07	$0.18\ ^{+0.05}_{-0.04}\ ^{+0.02}_{-0.02}$	0.21
4000 – 7113	0.1 – 0.178	5300	0.13	32	0.12	0.93	1.04	$0.17\ ^{+0.04}_{-0.03}\ ^{+0.02}_{-0.02}$	0.20
4000 – 7113	0.178 – 0.316	5300	0.24	24	0.064	0.90	1.03	$0.13\ ^{+0.03}_{-0.03}\ ^{+0.01}_{-0.01}$	0.14
4000 – 7113	0.316 – 0.562	5300	0.42	9	0.013	0.86	1.04	$0.049\ ^{+0.022}_{-0.016}\ ^{+0.006}_{-0.006}$	0.045
7113 – 12649	0.1 – 0.178	9500	0.13	13	0.043	0.79	1.08	$0.097\ ^{+0.035}_{-0.026}\ ^{+0.021}_{-0.022}$	0.106
7113 – 12649	0.178 – 0.316	9500	0.24	12	0.046	0.94	1.05	$0.066\ ^{+0.025}_{-0.019}\ ^{+0.011}_{-0.010}$	0.084
7113 – 12649	0.316 – 0.562	9500	0.42	9	0.003	0.89	1.05	$0.051\ ^{+0.023}_{-0.016}\ ^{+0.009}_{-0.008}$	0.033
12649 – 22494	0.178 – 0.316	17000	0.24	5	0.022	0.84	1.07	$0.038\ ^{+0.026}_{-0.016}\ ^{+0.015}_{-0.016}$	0.032
12649 – 22494	0.316 – 0.562	17000	0.42	7	0.013	0.99	1.06	$0.043\ ^{+0.023}_{-0.016}\ ^{+0.013}_{-0.012}$	0.018

Table 7.6b: *the reduced cross section $\tilde{\sigma}$ as defined in equation 7.10 measured in (x, Q^2) bins. The symbols in the heading are explained in the text.*

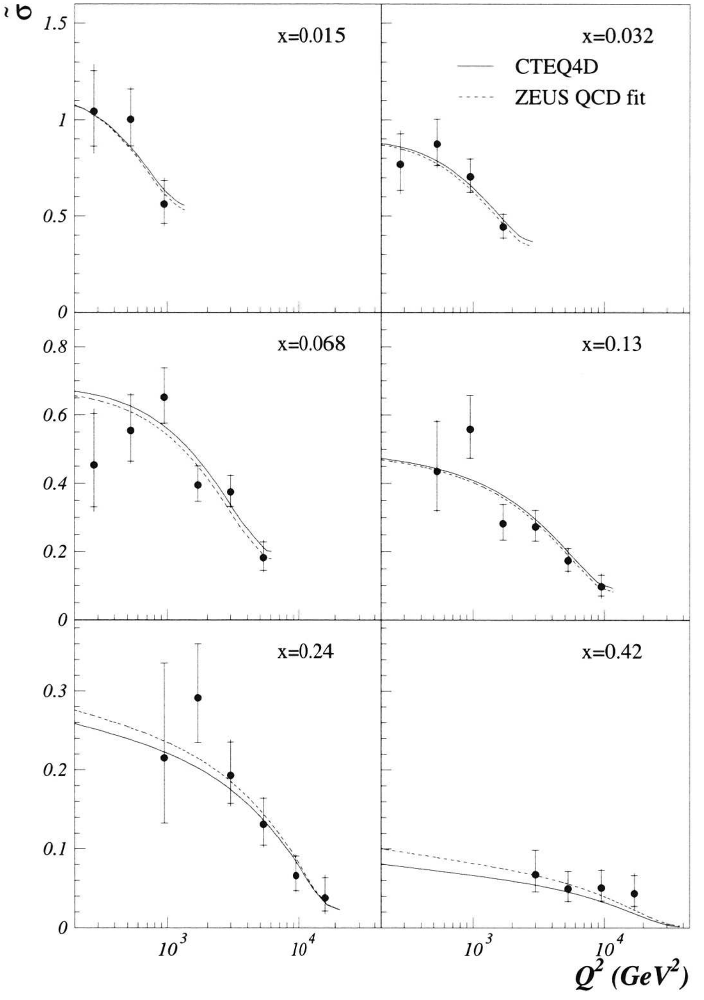

Figure 7.9: *the reduced charged current cross section $\tilde{\sigma}$ as a function of Q^2 for various values of x. The dots represent the measured cross section while the Standard Model expectations evaluated using the CTEQ4D PDFs are shown by solid lines. Also shown as dashed lines are the results of the NLO QCD fit.*

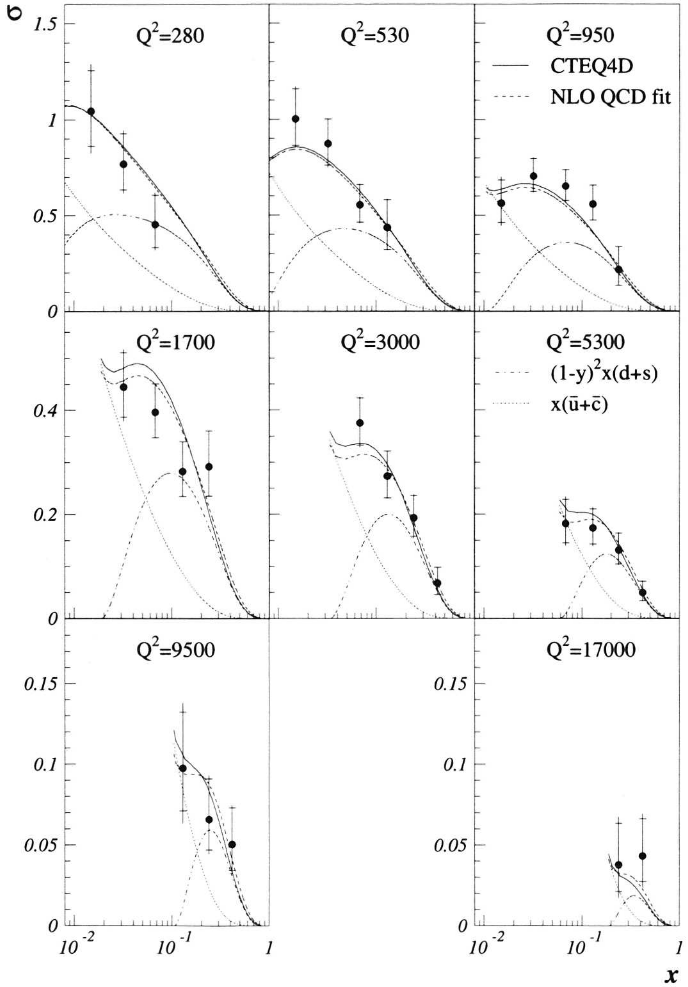

Figure 7.10: *the reduced charged current cross section $\tilde{\sigma}$ as a function of x for various values of Q^2. The dots represent the measured cross section while the expectations of the Standard Model evaluated using the CTEQ4D PDFs are shown as solid lines. For illustration the leading order parton density combinations $x(\bar{u}+\bar{c})$ and $(1-y)^2x(d+s)$, taken from the CTEQ4L parametrisation, are plotted as dotted and dash-dotted lines, respectively. Also shown as dashed lines are the results of the NLO QCD fit.*

Chapter 8

Other topics

8.1 Measurement of M_W

The single differential cross section $d\sigma/dQ^2$ as a function of Q^2 is determined by the Fermi constant G_F, a term $\mathcal{F}(Q^2)$ that contains the dependence on the parton density functions and a propagator term $M_W^2/(Q^2 + M_W^2)$:

$$\frac{d\sigma}{dQ^2} = G_F^2 \left(\frac{M_W^2}{Q^2 + M_W^2}\right)^2 \times \mathcal{F}(Q^2) \tag{8.1}$$

The propagator term is responsible for the rapid fall-off of the cross section towards high Q^2. This yields a reasonable sensitivity to the mass of the W boson as is illustrated in figure 8.1. This plot, basically the same as figure 7.6b, shows the ratio of the measured cross section $d\sigma/dQ^2$ to the Standard Model expectation evaluated with the CTEQ4D parton density functions. The lines show the results of the Standard Model predictions with different W masses varying between 60 GeV and 100 GeV. At the highest Q^2 values the predicted cross section is quite sensitive to M_W. Unfortunately, the measured cross section has a large uncertainty due to the lack of statistics.

The value of M_W is obtained via a binned log-likelihood fit to the cross section $d\sigma/dQ^2$ where M_W acts as the free parameter. The fit is performed with MINUIT [64] and yields a mass

$$M_W = 80.4^{+2.6}_{-2.4}(\text{stat})^{+4.2}_{-3.9}(\text{syst})^{+2.6}_{-2.6}(\text{PDF})\ \text{GeV} \tag{8.2}$$

with a minimum $\chi^2/dof = 1.2$. The central value is obtained using the CTEQ4D PDFs. The systematic error is evaluated by shifting the measured cross section with the size of the error of each source as listed in section 7.4. Positive and negative deviations of the central value of the M_W fit are added separately in quadrature. The error originating from the uncertainties in the partonic content of the proton is estimated by repeating the fit using the CTEQ4M, the MRSA and the MRSH PDFs and the NLO QCD fit instead of the CTEQ4D PDFs. The deviations from the central value are added in quadrature.

Another fit is performed to determine M_W under more restrictive theoretical assumptions. In this fit G_F and M_W are related by the Standard Model constraint

$$G_F = \frac{\pi\alpha}{\sqrt{2}} \frac{M_Z^2}{(M_Z^2 - M_W^2)M_W^2} \frac{1}{1 - \Delta r} \tag{8.3}$$

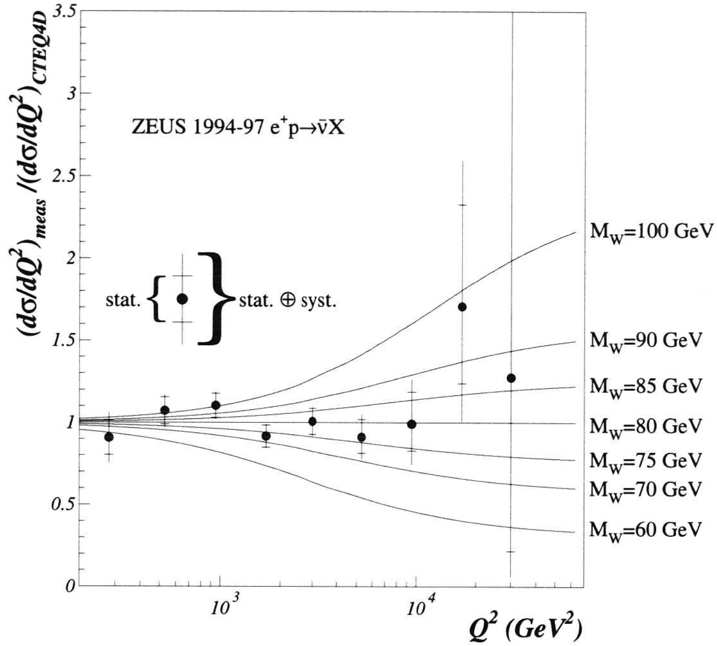

Figure 8.1: *ratio of the measured cross section $d\sigma/dQ^2$ to the Standard Model cross section prediction evaluated using the CTEQ4D PDFs. The lines show the Standard Model predictions with different W boson masses ranging from 60 GeV to 100 GeV.*

where M_Z is the mass of the Z boson and α is the fine structure constant. The term Δr contains the electroweak radiative corrections to the lowest order expression for G_F and it is a function of α and the masses of the fundamental bosons and fermions. All fermion masses, except for the mass m_t of the top quark, and α and M_Z are fixed at the PDG values [1]. The central result of the fit is obtained with $m_t = 175$ GeV and a Higgs boson mass M_H of 100 GeV and yields

$$M_W = 80.50^{+0.24}_{-0.25}(\text{stat})^{+0.13}_{-0.16}(\text{syst}) \pm 0.31(\text{PDF})^{+0.03}_{-0.06}(\Delta m_t, \Delta M_H, \Delta M_Z) \text{ GeV} \tag{8.4}$$

The last error is obtained by re-evaluating M_W with m_t in the range $170 < m_t < 180$ GeV, M_H in the range $100 < M_H < 220$ GeV and M_Z in the range $91.180 < M_Z < 91.194$ GeV. The dependence of M_W on these changes is small and the resulting error is negligible compared to the other errors.

Both values of M_W are in agreement with the current world average $M_W = 80.41 \pm 0.10$ GeV using timelike W production experiments at Tevatron and at LEP [1]. Note, however, that the second fit cannot be seen as an independent measurement of the W mass as it strongly depends on the underlying Standard Model. Since the mass of the W boson as measured from CC DIS is the mass of the spacelike W, the results of both fits are complementary to the measurements of

M_W from $p\bar{p}$ and e^+e^- annihilation and constitute an important check of the Standard Model consistency.

8.2 Large rapidity gap events

In deep inelastic scattering events the proton usually breaks up after the hard interaction. This leads to an energy deposit around the forward beampipe caused by the proton remnant. Also an energy flow is observed between the remnant and the current jet. However, in about 5% of the neutral current DIS events with Q^2 exceeding 5 GeV^2 the proton does not break up [66]. This type of events is referred to as diffractive DIS. Diffractive scattering is generally understood to proceed through the exchange of a colourless object with the quantum numbers of the vacuum, called the Pomeron, of which the true nature is still unclear. The Pomeron also has a partonic structure that is probed by the virtual photon. One of the experimental signatures of diffractive DIS events is that the hadronic energy deposit closest to the proton beam direction is found at a large polar angle or, equivalently, at a small pseudorapidity. Therefore, these events are generally referred to as "large rapidity gap" events.

It is interesting to see if these diffractive events also occur in charged current DIS. As the coupling of the exchanged W boson is sensitive to the flavour of the Pomeron constituents, this would provide additional information on the nature of the Pomeron. A search for diffractive charged current DIS events has been presented in [6]. Two variables are used to identify large rapidity gap events, η_{max} and $\cos\theta_H$. The variable η_{max} is defined as the pseudorapidity of the most forward island with energy greater than 400 MeV. The hadronic angle θ_H is given by the energy weighted mean polar angle of the energy deposits in the calorimeter, $\cos\theta_H = \sum_i P_{z,i} / \sum_i E_i$ where the sum runs over all calorimeter cells. Note that θ_H is not the same as the quantity γ_h as defined in chapter 6.

Figures 8.2a and 8.2b show the distributions of η_{max} and $\cos\theta_H$, respectively. The dots represent the charged current data and the filled histogram is the total expectation of the ARIADNE charged current Monte Carlo sample combined with the expected background. The dotted histogram is the prediction of the MEPS Monte Carlo sample. Figure 8.2c shows a scatter plot of $\cos\theta_H$ versus η_{max} for the final data sample. The rectangular box indicates the region $\eta_{max} < 2.5$ and $\cos\theta_H < 0.75$ which is taken as the definition of large rapidity gap events. Ten events are observed in this region, while 4.7 events are expected according to the ARIADNE Monte Carlo prediction and 3.5 events according to MEPS, both including a background contribution of 0.4 events. One of the observed events is shown in figure 8.3. In the CCfied neutral current data sample 6.1 events are observed. These numbers indicate that a fraction of the charged current events can be of a diffractive nature. More data are necessary, however, to make a definite statement about this.

8.3 Hadronic final state

The cross section measurements presented in the previous chapter are all inclusive, i.e. they ignore all structure in the hadronic final state. Nevertheless, it is interesting to see if the hadronic final state is properly described in the Monte Carlo predictions. In the previous

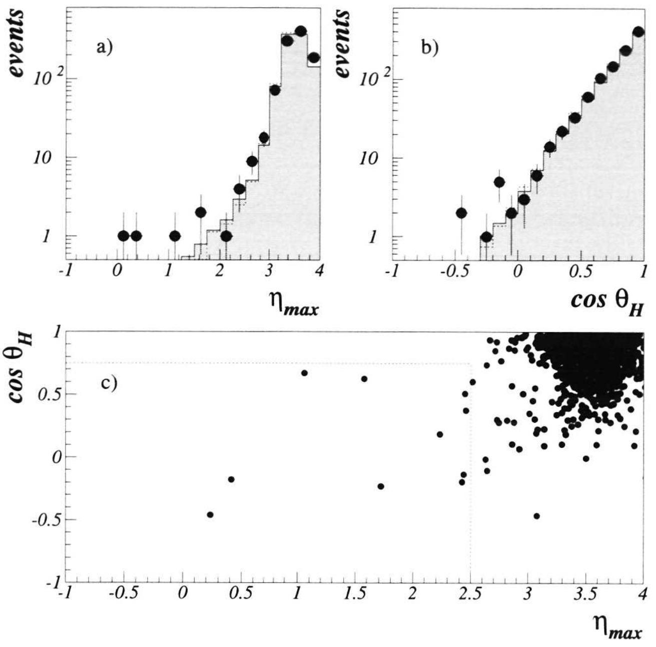

Figure 8.2: *distribution of charged current data (dots) and ARIADNE Monte Carlo data (full histograms) as a function of (a) the pseudorapidity η_{max} of the most forward island and (b) the cosine of the hadronic angle θ_H. The dotted histograms show the expectations of the MEPS Monte Carlo. Figure (c) shows the distribution of charged current data events in the ($\eta_{max}, \cos\theta_H$) plane. The box indicates the region that satisfies the definition of large rapidity gap events.*

section it was shown that the rapidity of the events can be described by Monte Carlo data. Here a number of properties of jets in the final state will be investigated.

Jets are defined according to the longitudinally invariant k_T algorithm [67] which is run in the inclusive mode [68]. The algorithm starts by considering a list of calorimeter objects with transverse energy E_T, azimuthal angle ϕ and pseudorapidity η. Initially these objects are taken as all calorimeter cells with an energy deposit. The algorithm then proceeds as follows

1. for each object i a distance parameter d_i is defined as $d_i = E_{T,i}^2$.

2. a distance parameter d_{ij} is defined as $d_{ij} = \min(E_i^2, E_j^2)\ [(\eta_i - \eta_j)^2 + (\phi_i - \phi_j)^2]$ for every pair of objects (i, j).

3. the smallest parameter d_{min} of all the d_i and d_{ij} is found.

4. if d_{min} is a pair distance parameter then the two objects i and j are merged into a new object according to formulae 8.5 to 8.7.

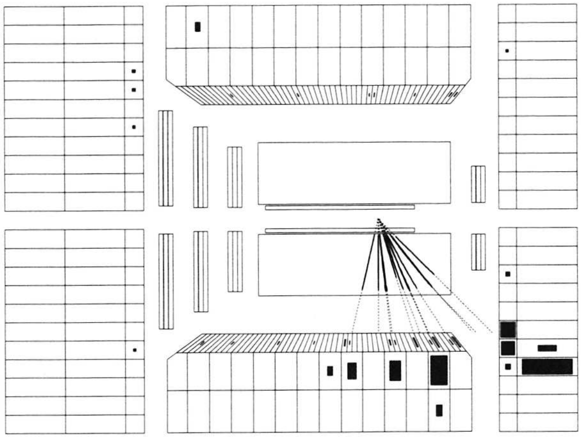

Figure 8.3: *example of a charged current event with a large rapidity gap. This specific event has* $\eta_{max} = 0.2$, $\cos\theta_H = -0.46$, $Q^2 = 286$ *GeV*^{2} *and* $x = 0.007$.

5. if d_{min} is of the d_i type then object i is added to the list of jets and discarded in the remainder of the algorithm.

6. steps 1 to 5 are repeated until $d_i < \min(d_{ij})$ for every object i.

The transverse energy, the azimuthal angle and the pseudorapidity of each jet are then computed as

$$E_{T,jet} = \sum_i E_{T,i} \tag{8.5}$$

$$\eta_{jet} = \frac{1}{E_{T,jet}} \sum_i E_{T,i}\,\eta_i \tag{8.6}$$

$$\phi_{jet} = \frac{1}{E_{T,jet}} \sum_i E_{T,i}\,\phi_i \tag{8.7}$$

where the sum runs over all calorimeter cells. Jets are only accepted if the transverse energy exceeds 6 GeV and the pseudorapidity is smaller than 2.5. In this way very forward jets due to the proton remnant are excluded.

In figure 8.4 the number of jets, the transverse energy, the pseudorapidity and the Q^2 distribution of the jets in the final charged current sample are shown. The dots represent the data while the histograms show the predictions of the ARIADNE and MEPS Monte Carlo sets. In general the measured distributions are well reproduced although a tendency for more multi-jet events in data than predicted is observed. This is also reflected in a harder Q^2 distribution than expected from Monte Carlo for 2-jet events.

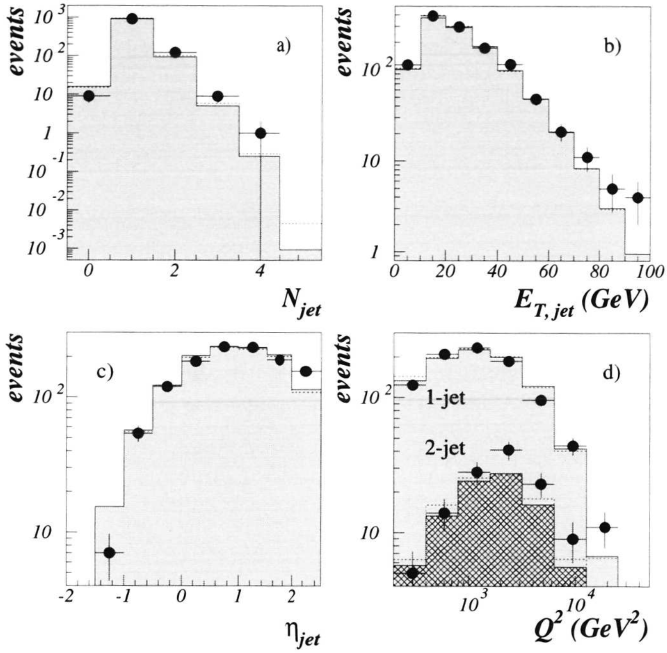

Figure 8.4: *jet properties of the selected charged current sample: (a) number of jets, (b) transverse jet energy $E_{T,jet}$, (c) pseudorapidity η_{jet}, (d) distribution in Q^2 for events with one or two jets. The dots denote charged current data while the filled and dashed histograms are the predictions of ARIADNE and MEPS, respectively.*

8.4 Comparison with NC DIS

Figure 8.5 compares the cross section $d\sigma/dQ^2$ for charged current DIS with the most recent ZEUS measurement of the neutral current cross section [55]. At $Q^2 \ll M_Z^2$ the photon propagator dominates the neutral current cross section. The charged current cross section is heavily suppressed in comparison, mainly due the factor $1/(Q^2 + M_W^2)^2$ as the magnitude of the coupling to the quarks and positron is about the same as for neutral current scattering (see equation 1.17). Going to higher Q^2 the neutral current cross section falls much more rapidly than the charged current cross section. For $Q^2 \gtrsim M_Z^2$ the two cross sections reach about the same magnitude, a demonstration of the electroweak $SU(2) \times U(1)$ unification.

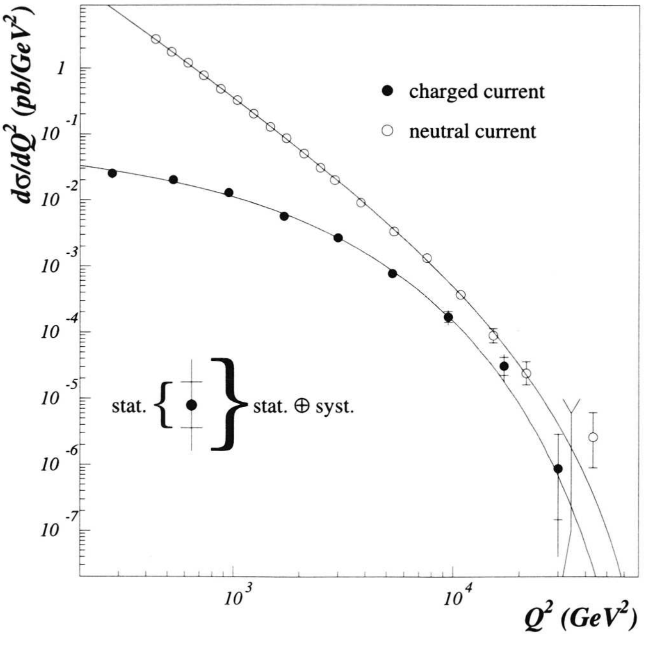

Figure 8.5: *comparison of the differential cross section $d\sigma/dQ^2$ for neutral current (circles) and charged current (dots) deep inelastic e^+p scattering from the ZEUS 1994-97 analysis. The lines represent the Standard Model predictions evaluated using the CTEQ4D parton density functions.*

References

[1] Particle Data Group, *Eur. Phys. J.* C **3** (1998) 1.

[2] some general reading:

F. Halzen and A.D. Martin, Quarks and leptons, Wiley 1984.

R.G. Roberts, The structure of the proton, Cambridge University Press 1990.

J. Engelen and P. Kooijman, *Prog. Part. Nucl. Phys.* **41** (1998) 1.

A.M. Cooper-Sarkar, R.C.E. Devenish and A. de Roeck, *Int. J. Mod. Phys.* A **13** (1998) 3385.

[3] H. Abramowicz et al., *Z. Phys.* C **25** (1984) 29.

P. Berge et al., *Z. Phys.* C **49** (1991) 187.

E. Oltman et al., *Z. Phys.* C **53** (1992) 51.

G.T. Jones et al., *Z. Phys.* C **62** (1994) 575.

[4] H1 collaboration, *Phys. Lett.* B **324** (1994) 241.

H1 collaboration, *Z. Phys.* C **67** (1995) 565.

H1 collaboration, *Phys. Lett.* B **379** (1996) 319.

[5] ZEUS collaboration, *Phys. Rev. Lett.* **75** (1995) 1006.

[6] ZEUS collaboration, *Z. Phys.* C **72** (1996) 47.

[7] D.Yu. Bardin, Č. Burdík, P.Ch. Christova and T. Riemann, *Z. Phys.* C **44** (1989) 149.

M. Böhm and H. Spiesberger, *Nucl. Phys.* B **304** (1988) 749.

H. Spiesberger, *Nucl. Phys.* B **349** (1991) 109.

[8] H. Spiesberger, in Future Physics at HERA, Vol. 1 (1996) 227.

[9] A. Arbuzov et al., *Comp. Phys. Comm.* **94** (1996) 128.

[10] H. Spiesberger et al., in Physics at HERA, Vol. 2 (1991) 798.

[11] A. Kwiatkowski, H. Spiesberger and H.-J. Möhring, *Z. Phys.* C **50** (1991) 165.
A. Kwiatkowski, H. Spiesberger and H.-J. Möhring, in Physics at HERA, Vol. 3 (1991) 1294.
A. Kwiatkowski, H. Spiesberger and H.-J. Möhring, *Comp. Phys. Comm.* **69** (1992) 155.

[12] A.M. Cooper-Sarkar et al., *J. Phys.* G **25** (1999) 1387.

[13] V.N. Gribov and L.N. Lipatov, *Sov. J. Nucl. Phys.* **15** (1972) 438, ibidem **15** (1972) 675.
L.N. Lipatov, *Sov. J. Nucl. Phys.* **20** (1975) 94.
G. Altarelli and G. Parisi, *Nucl. Phys.* B **126** (1977) 298.
Yu.L. Dokshitser, *Sov. Phys. JETP* **46** (1977) 641.

[14] W.L. van Neerven, in Future Physics at HERA, Vol. 1 (1996) 56 and references therein.

[15] H.L. Lai et al., *Phys. Rev.* D **55** (1997) 1280.

[16] A.D. Martin, W.J. Stirling and R.G. Roberts, *Phys. Rev.* D **50** (1994) 6734.

[17] A.D. Martin, R.G. Roberts, W.J. Stirling and R.S. Thorne, *Eur. Phys. J.* C **4** (1998) 463.
A.D. Martin, R.G. Roberts, W.J. Stirling and R.S. Thorne, hep-ph/9907231.

[18] M. Glück, E. Reya and A. Vogt, *Z. Phys.* C **67** (1995) 433.

[19] ZEUS collaboration, *Eur. Phys. J.* C **7** (1999) 609.
M. Botje, NIKHEF-99-011 (1999).

[20] ZEUS collaboration, *Z. Phys.* C **72** (1996) 399.

[21] H1 collaboration, *Nucl. Phys.* B **470** (1996) 3.

[22] E665 collaboration, *Phys. Rev.* D **54** (1996) 3006.
NMC collaboration, *Nucl. Phys.* B **483** (1997) 3.
BCDMS collaboration, *Phys. Lett.* B **223** (1989) 485.
BCDMS collaboration, *Phys. Lett.* B **237** (1990) 592.
L.W. Whitlow et al., *Phys. Lett.* B **282** (1992) 475.

[23] NMC collaboration, *Nucl. Phys.* B **487** (1997) 3.

[24] W.G. Seligman et al., *Phys. Rev. Lett.* **79** (1997) 1213.

[25] E866 collaboration, *Phys. Rev. Lett.* **80** (1998) 3715.

[26] M. Botje, ZEUS-Note 97–66 (1997).

[27] W. Melnitchouk and A.W. Thomas, *Phys. Lett.* B **377** (1996) 11.
W. Melnitchouk and J.C. Peng, *Phys. Lett.* B **400** (1997) 220.

[28] U.K. Yang and A. Bodek, *Phys. Rev. Lett.* **82** (1999) 2467.

[29] J. Gomez et al., *Phys. Rev.* D **49** (1994) 4348.

[30] ZEUS collaboration, The ZEUS detector, Status Report 1993, DESY 1993.

[31] M. Derrick et al., *Nucl. Instrum. Methods* A **309** (1991) 77.
A. Andresen et al., *Nucl. Instrum. Methods* A **309** (1991) 101.
A. Caldwell et al., *Nucl. Instrum. Methods* A **321** (1992) 356.
A. Bernstein et al., *Nucl. Instrum. Methods* A **336** (1993) 23.

[32] J. Straver, Thesis, University of Amsterdam (1991).

[33] A. Bamberger et al., *Nucl. Instrum. Methods* A **382** (1996) 419.

[34] N. Harnew et al., *Nucl. Instrum. Methods* A **279** (1989) 290.
B. Foster et al., *Nucl. Instrum. Methods* A **338** (1994) 254.

[35] C. Alvisi et al., *Nucl. Instrum. Methods* A **305** (1991) 30.

[36] A. Bamberger et al., *Nucl. Instrum. Methods* A **401** (1997) 63.

[37] G. Abbiendi et al., *Nucl. Instrum. Methods* A **333** (1993) 342.

[38] H. Abramowicz et al., *Nucl. Instrum. Methods* A **313** (1992) 126.

[39] B. Surrow, Thesis, University of Hamburg (1998).

[40] ZEUS collaboration, *Z. Phys.* C **63** (1994) 391.

[41] H. Bethe and W. Heitler, *Proc. Roy. Soc.* A **146** (1934) 83.
K.J.F. Gaemers and M. van der Horst, *Nucl. Phys.* B **316** (1989) 269; Erratum: *Nucl. Phys.* B **336** (1990) 184.
M. van der Horst, *Nucl. Phys.* B **347** (1990) 149.

[42] W. Verkerke, Thesis, University of Amsterdam (1998).

[43] A. Kruse, Thesis, University of Amsterdam (1999).

[44] A. Kruse and A.I. van Sighem, ZEUS-Note 98-25 (1998).

[45] Application Software Group, CERN Program Library Long Writeup W5013.

[46] G.A. Schuler and H. Spiesberger, in Physics at HERA, Vol. 3 (1991) 1419.

[47] G. Ingelman, in Physics at HERA, Vol. 3 (1991) 1366.
G. Ingelman, A. Edin and J. Rathsman, DESY 96-057 (1996).

[48] M. Bengtsson and T. Sjöstrand, *Z. Phys.* C **37** (465) 1988.
M. Bengtsson et al., in Proceedings of the HERA workshop, Vol. 1 (1987) 149.

[49] L. Lönnblad, *Comp. Phys. Comm.* **71** (1992) 71.

[50] T. Sjöstrand, *Comp. Phys. Comm.* **82** (1994) 74.

[51] A. Quadt and O. Ruske, ZEUS-Note 98–36 (1998).

[52] G. Marchesini et al., *Comp. Phys. Comm.* **67** (1992) 465.

[53] J.A.M. Vermaseren, *Nucl. Phys.* B **229** (1983) 347.
S.P. Baranov et al., in Physics at HERA, Vol. 3 (1991) 1478.

[54] U. Baur, J.A.M. Vermaseren and D. Zeppenfeld, *Nucl. Phys.* B **375** (1992) 3.

[55] ZEUS collaboration, *Eur. Phys. J.* C **11** (1999) 427.

[56] R. Pawlak, ZEUS-Note 98–40 (1998).

[57] H. Abramowicz, A. Caldwell and R. Sinkus, *Nucl. Instrum. Methods* A **365** (1995) 508.

[58] S. Bentvelsen, J. Engelen and P. Kooijman, in Physics at HERA, Vol. 1 (1991) 23.

[59] F. Jacquet and A. Blondel, in Proceedings of the study of an *ep* facility for Europe, DESY 79–48 (1979), 377.

[60] G.M. Briskin, Thesis, University of Tel Aviv (1998).

[61] U. Behrens et al., *Nucl. Instrum. Methods* A **289** (1990) 115.

[62] T.C. Awes et al., *Nucl. Instrum. Methods* A **311** (1992) 130.

[63] J. Grosse-Knetter, ZEUS-Note 97–39 (1997).
J. Grosse-Knetter, ZEUS-Note 98–31 (1998).

[64] F. James, CERN Program Library Long Writeup D506.

[65] A. Andresen et al., *Nucl. Instrum. Methods* A **290** (1990) 95.

[66] ZEUS collaboration, *Z. Phys.* C **68** (1995) 569.
ZEUS collaboration, *Phys. Lett.* B **315** (1993) 481.
H1 collaboration, *Phys. Lett.* B **348** (1995) 681.

[67] S. Catani, Yu.L. Dokshitzer, M.H. Seymour and B.R. Webber, *Nucl. Phys.* B **406** (1993) 187.

[68] S.D. Ellis and D.E. Soper, *Phys. Rev.* D **48** (1993) 3160.

Summary

Deep inelastic scattering (DIS) of leptons from protons is the main source of information on the structure of the proton. Two types of DIS can be distinguished: neutral current scattering in which a photon or a Z particle is exchanged, and charged current scattering where the exchanged particle is a $W^{\pm}$ boson. In contrast to neutral current interactions, where all quark and antiquark flavours contribute, only specific combinations of quarks and antiquarks participate in charged current DIS. Both processes have been studied extensively at fixed target experiments. Since 1992 the HERA collider in Hamburg has been operational, a unique machine as it is the first positron-proton collider in the world. It offers the possibility of extending the kinematic range in which DIS is studied by two orders of magnitude in both Q^2 and $1/x$ compared to fixed target experiments.

In this thesis an analysis is presented of charged current interactions as measured by the ZEUS detector in the years 1994 to 1997. In this period ZEUS collected an integrated luminosity of 47.53 pb^{-1} at a centre-of-mass energy of 300 GeV. Since the cross section for the charged current DIS interaction is very small compared to the cross section for other ep processes the selection of charged current events is one of the biggest challenges in this analysis. Special attention is paid to improving the event selection at high x. In this region the events are found in the very forward direction where the acceptance of the tracking detectors is almost zero. A total number of 1047 charged current events is selected from the data whereas about 1.3 million events are selected online as possible charged current candidates.

A characteristic property of charged current events that is used in the online event selection is a large missing transverse momentum in the detector due to the evanescent antineutrino. Additional cuts are necessary to reduce the considerable amount of background that is still present in the sample. First of all halo muons and cosmic rays form a substantial background. These events are removed with a special muon finder package that has been developed for this analysis. It is based on identifying the characteristic pattern of energy deposits and tracks that is caused by the muon when it traverses the detector. Also genuine ep processes such as neutral current DIS and photoproduction form a background and special cuts have been designed to remove these types of events. After all the event selection cuts have been applied the estimated amount of background still present in the signal sample is typically below 1%. Only at low Q^2 the photoproduction background becomes sizeable, around 20%.

The reconstruction of the kinematics of charged current DIS events is based on the measurement of the hadronic final state. However, due to energy loss in inactive material and through uninstrumented regions of the detector large biases from the true values are observed in the reconstruction. A new reconstruction method is presented that corrects the energy of individual clusters of calorimeter cells, so-called islands, and that calculates the kinematic variables using

these islands. As a result the bias is reduced to negligible values in almost the entire kinematic plane and also the resolution improves.

Measurements are presented of the single differential cross sections $d\sigma/dQ^2$, $d\sigma/dx$ and $d\sigma/dy$ above a minimum Q^2 value of 200 GeV^2. Also the double differential cross section $d\sigma/dxdQ^2$ is measured, for the first time at HERA. The precision of the cross sections is dominated by the statistical error although in some of the bins the systematic error is comparable in size. The uncertainties in the calorimeter energy scale and in the modelling of the hadronic showers are the largest sources of systematic errors.

In the whole kinematic range under study the measured cross sections can be described adequately by the CTEQ4D set of parton density functions. Also the predictions of a NLO QCD fit agree very well with the data and even seem to follow the tendencies that are observed at high x. In that region the measured cross section is somewhat above the CTEQ4D prediction. This is also observed for the NLO QCD fit. It turns out that the QCD fit has a larger d quark density than CTEQ4D. However, it is not necessary to add an extra contribution to the d density by hand as has been suggested in the most recent literature since the same rise is observed by including in the fit the recent fixed target data on $x(\bar{d}-\bar{u})$ at high x. The error on the predicted d/u ratio is rather large at very high x, however, and no definite statements about the d density can be made.

From the differential cross section $d\sigma/dQ^2$ the mass M_W of the W boson can be extracted. A fit to the shape of the cross section yields $M_W = 80.4^{+2.6}_{-2.4}(\text{stat})^{+4.2}_{-3.9}(\text{syst})^{+2.6}_{-2.6}(\text{PDF})$ GeV which is to be compared with the world average of 80.41 ± 0.10 GeV. This measurement shows that the mass of the spacelike W boson is the same as that of the timelike W as measured at e^+e^- and $p\bar{p}$ experiments, which constitutes an important consistency check of the Standard Model.

A search is performed for large rapidity gap events that might signal the presence of a diffractive component in the charged current data. Although a handful of promising events are found the present amount of data does not allow a measurement of the diffractive charged current cross section.

Finally, the measured charged and neutral current cross sections $d\sigma/dQ^2$ are compared. Over several orders of magnitude both cross sections are described by the Standard Model predictions. Future running with increased luminosities and alternating e^+ and e^- running will drastically reduce the statistical and possibly the systematic errors on the cross section measurements at high Q^2 and high x for both channels. This will allow a measurement of the structure function xF_3 for neutral current scattering. Moreover, it might become possible to extract quark densities directly from the measured double differential cross sections.

Samenvatting

Diep inelastische verstrooiing (DIS) van leptonen aan protonen is een van de meest directe methoden om meer te weten te komen over de structuur van het proton. Er bestaan twee verschillende soorten DIS: neutrale stroom verstrooiing, waar een foton of een Z-deeltje uitgewisseld wordt, en geladen stroom verstrooiing, waar het uitgewisselde deeltje een W-boson is. In tegenstelling tot neutrale stroom interacties waaraan alle quark- en antiquarksmaken bijdragen, doen alleen bepaalde combinaties van quarks en antiquarks mee in geladen stroom DIS. Beide processen zijn uitvoerig bestudeerd in "fixed target" experimenten. Sinds 1992 is in Hamburg de HERA versneller operationeel, een unieke machine omdat het de eerste positron-proton botser ter wereld is. HERA maakt het mogelijk om het kinematische gebied waarin DIS bestudeerd wordt, uit te breiden met twee ordes van grootte in Q^2 en $1/x$ in vergelijking met "fixed target" experimenten.

In dit proefschrift wordt een analyse gepresenteerd van geladen stroom interacties zoals die met de ZEUS detector zijn gemeten in de jaren 1994 tot en met 1997. In deze periode verzamelde ZEUS een geïntegreerde luminositeit van 47.53 pb^{-1} bij een zwaartepuntsenergie van 300 GeV. Omdat de werkzame doorsnede voor geladen stroom DIS interacties erg klein is vergeleken met de werkzame doorsnede voor andere ep processen, is de selectie van geladen stroom events een van de grootste uitdagingen in deze analyse. Veel aandacht wordt besteed aan het verbeteren van de selectie van events bij hoge x. In dat gebied gaan de geproduceerde hadronen sterk in de voorwaartse richting waar de acceptantie van de dradenkamers bijna nihil is. In totaal worden er uit de data 1047 geladen stroom events geselecteerd, terwijl er 1,3 miljoen events "online" geselecteerd zijn als mogelijke kandidaten voor geladen stroom events.

Een karakteristieke eigenschap van geladen stroom events, die ook gebruikt wordt in de online eventselectie, is een aanzienlijke missende transversale impuls in de detector die veroorzaakt wordt door het ontsnappende antineutrino. Er zijn echter nog andere sneden nodig om de grote hoeveelheid achtergrond te reduceren die nog steeds in het sample aanwezig is. In de eerste plaats vormen halomuonen en kosmische stralen een substantiële achtergrond. Deze events worden verwijderd met behulp van een "muonzoeker" die speciaal voor deze analyse ontwikkeld is. De werking ervan is gebaseerd op het opsporen van het karakteristieke patroon van energiedeposities en sporen dat door een muon veroorzaakt wordt, als het de detector doorkruist. Ook ep processen zoals neutrale stroom DIS en fotoproductie vormen een achtergrond. Om dit soort events te verwijderen zijn speciale sneden ontwikkeld. Na alle selectiesneden is de geschatte hoeveelheid achtergrond die nog in het sample aanwezig is, typisch kleiner dan 1%. De achtergrond is alleen aanzienlijk, ongeveer 20%, in het lage Q^2 gebied en wordt daar voornamelijk door fotoproductie gevormd.

De reconstructie van de kinematische variabelen die geladen stroom events beschrijven, maakt gebruik van metingen aan de hadronische eindtoestand van die events. Door verlies van energie in inactief materiaal en ongeïnstrumenteerde delen van de detector zijn er echter grote verschillen tussen de gemeten en de echte waarden. Een nieuwe reconstructiemethode wordt besproken die de energie van individuele clusters van calorimetercellen, eilanden geheten, corrigeert. Met deze eilanden worden dan de kinematische grootheden berekend. Het resultaat van deze correctie is dat de gemiddelde afwijking van de echte waarde verwaarloosbaar klein wordt in het grootste deel van het kinematische bereik. Dit gaat bovendien gepaard met een verbetering in de resolutie.

Vervolgens worden de metingen van de differentiële werkzame doorsneden $d\sigma/dQ^2$, $d\sigma/dx$ en $d\sigma/dy$ gepresenteerd boven een minimum Q^2 van 200 GeV^2. Ook de dubbel-differentiële werkzame doorsnede $d\sigma/dxdQ^2$ is gemeten en wel voor de eerste keer bij HERA. De fout op de gemeten werkzame doorsneden wordt gedomineerd door de statistische fout, hoewel de systematische fout in sommige bins van dezelfde orde van grootte is. De onzekerheid in de energieschaal van de calorimeter en die in de simulatie van hadronische cascades leveren de grootste bijdragen aan de systematische fout.

De gemeten werkzame doorsnede kan in het hele kinematische gebied dat door de metingen bestreken wordt, beschreven worden door de CTEQ4D parton-dichtheidsfuncties. Ook de voorspellingen van een NLO QCD fit komen goed overeen met de data en het lijkt erop dat ook de trends in de data bij hoge x beschreven worden. In dat gebied is de werkzame doorsnede namelijk wat hoger dan de voorspelling van CTEQ4D en dat is ook het geval voor de NLO QCD fit. Het blijkt dat de QCD fit een grotere d-quarkdichtheid wil dan CTEQ4D. Het is echter niet nodig om expliciet een extra bijdrage aan de d-dichtheid toe te voegen zoals recentelijk gesuggereerd is in de literatuur. Dezelfde stijging kan namelijk ook verkregen worden door in de fit de nieuwste "fixed target" metingen van $x(\bar{d}-\bar{u})$ bij hoge x mee te nemen. De fout op de voorspelling van d/u is echter vrij groot bij hoge x en bindende conclusies over de d-dichtheid kunnen nu nog niet getrokken worden.

Uit de differentiële werkzame doorsnede $d\sigma/dQ^2$ kan de massa M_W van het W-deeltje bepaald worden. Een fit aan de vorm van de werkzame doorsnede levert een waarde op van $80.4^{+2.6}_{-2.4}(\mathrm{stat})^{+4.2}_{-3.9}(\mathrm{syst})^{+2.6}_{-2.6}(\mathrm{PDF})$ GeV, tegenover een wereldgemiddelde van 80.41 ± 0.10 GeV. Deze meting laat zien dat de massa van het ruimteachtige W-boson hetzelfde is als die van de tijdachtige W, die gemeten wordt bij e^+e^-- en $p\bar{p}$-experimenten. Dit is een belangrijke verificatie van de consistentie van het Standaardmodel.

Verder is er gezocht naar events met een groot rapiditeitsgat. Zulke events kunnen op de aanwezigheid van een diffractieve component in de geladen stroom data duiden. Alhoewel er een handvol veelbelovende events gevonden is, is het gezien de huidige hoeveelheid data nog niet mogelijk een meting te verrichten van de diffractieve geladen stroom werkzame doorsnede.

Tenslotte zijn de geladen en neutrale stroom werkzame doorsneden $d\sigma/dQ^2$ met elkaar vergeleken. Over een aantal ordes van grootte kunnen beide werkzame doorsneden beschreven worden door het Standaardmodel. Toekomstige experimenten met een grotere luminositeit en met afwisselend positron- en electronbundels zullen de statistische fout en mogelijkerwijs ook de systematische fout op de werkzame doorsneden bij hoge x en hoge Q^2 voor beide processen aanzienlijk kleiner maken. Dit opent de weg naar een meting van de structuurfunctie xF_3 voor neutrale stroom verstrooiing. Bovendien wordt het dan mogelijk om de quarkdichtheden direct uit de gemeten dubbeldifferentiële werkzame doorsneden te bepalen.

Acknowledgements

The results presented in this thesis would not have obtained without the collaboration with many people from NIKHEF and DESY. In the first place I want to express my gratitude towards Andrés Kruse from whom I inherited a tremendous amount of expertise, neatly summarised in myriads of lines of Fortran code, when I started at NIKHEF in 1995. With his help I mastered all this knowledge and together we worked on the further development of the muon finder MUFFIN. His pioneering analysis of charged current interactions at ZEUS forms one of the corner stones on which this thesis is founded.

Also I would like to thank my other colleagues at NIKHEF for their contributions, suggestions and for the many discussions we had, occasionally accompanied by some spirituous refreshments. With pleasure I will remember the four years I spent in the ZEUS group. In particular I am thankful to my promotor Jos Engelen and my co-promotor Paul Kooijman for their support and advice during these years.

This thesis would hardly have been possible without the invaluable input from various people at DESY. In particular I would like to thank Kunihiro Nagano for our pleasant and fruitful cooperation. Also I owe a great deal of gratitude to Masahiro Kuze, Ken Long and Stefan Schlenstedt from who I received strong support and guidance.

Finally, working at NIKHEF would not have been possible without the members of the supporting staff. Of these I would like to mention the people of the computergroup whose assistance is gratefully acknowledged. The help of the secretaries was indispensable when I was wading through the swamps of bureaucracy necessary for some of my trips abroad. And last but not least, I would like to thank the tea lady for the nearly infinite supply of coffee and tea she provided every day.